Leveraging Carbon Based Nanoparticle Dispersions for Fracture Toughness Enhancement and Electro-mechanical Sensing in Multifunctional Composites

Nishant Prashant Shirodkar

Dissertation submitted to the Faculty of the
Virginia Polytechnic Institute and State University
in partial fulfillment of the requirements for the degree of

Doctor of Philosophy
in
Aerospace Engineering

Gary D. Seidel, Chair
Shengfeng Cheng
Michael Philen
Scott W. Case
Mayuresh Patil

April 27, 2022
Blacksburg, Virginia

Keywords: Carbon nanotubes, Graphene nanoplatelets, Fracture toughness, Enhancement mechanisms, Polymer bonded energetics, Structural Health Monitoring, Damage assessment

Leveraging Carbon Based Nanoparticle Dispersions for Fracture Toughness Enhancement and Electro-mechanical Sensing in Multifunctional Composites

Nishant Prashant Shirodkar

ABSTRACT

The discovery of carbon nanotubes (CNTs) in 1990s popularized a new area of research in materials science called Nanoscience. In the following decades, several carbon based nanoparticles were discovered or engineered, and with the discovery of Graphene nanoplatelets (GNPs) in 2010, carbon based nanoparticles were propelled as the most promising class of nanoparticles. High mechanical strength and stiffness, excellent electrical and thermal conductivity, and high strength to weight ratios are some of the unique abilities of CNTs and GNPs which allow for their use in a wide array of applications from aerospace materials to electronic devices. In the current work presented herein, CNTs and GNPs are added to polymeric materials to create a nanocomposite material. The effects of this nanoparticle addition (a.k.a reinforcement) on the mechanical properties of the nanocomposite polymer materials are studied. Specifically, efforts are focused on studying fracture toughness, a material property that describes the material's ability to resist crack growth. Relative to the conventional metals used in structures, epoxy-based composites have poor fracture toughness. This has long been a weak link when using epoxy composites for structural applications and therefore several efforts are being made to improve their fracture toughness. In the first, second and third chapters, the enhancement of fracture toughness brought about by the addition of CNTs and GNPs was investigated. CNT-Epoxy and GNP-Epoxy Compact Tension (CT) samples were fabricated with 0.1% and 0.5% nanofiller weight concentrations. The potential synergistic effects of dual nanofiller reinforcements were also explored using CNT/GNP-Epoxy CT samples at a 1:3, 3:1 and 1:1 ratio of CNT:GNP. Displacement controlled CT tests were conducted according to ASTM D5045 test procedure and the critical stress intensity factor, K_{IC}, and the critical fracture energy, G_{IC}, were calculated for all of the material systems. Significant enhancements relative to neat epoxy were observed in reinforced epoxies. Fracture surfaces were analyzed via scanning electron microscopy. Instances of CNT pullouts on the fracture surface were observed, indicating the occurrence of crack bridging. Furthermore, increased surface roughness, an indicator of crack deflection, was observed along with some crack bifurcations in the GNP-Epoxy samples. In the fourth chapter of Part I of the dissertation, the influence of pre-crack characteristics on the Mode-I fracture toughness of epoxy is investigated. Pre-crack characteristics such as pre-crack length, crack front shape, crack thickness and crack plane profile are evaluated and their influence on the peak load, fracture displacement, and the critical stress intensity factor, K_{IC} is studied. In order to improve consistency in generating a pre-crack, a guillotine-style razor tapping device was developed to initiate the pre-crack. An approach of quantitatively characterizing the crack front shape using a two-parameter function is introduced. Surface features present on the pre-crack surface are classified and their effects on the post crack initiation behavior of the sample are analyzed. This study aims to identify and increase the understanding of the various factors that cause variation in the fracture toughness data of polymeric materials, thus leading to more informed engineering design decisions and evaluations. Chapters six and seven of Part II of the dissertation investigate the SHM capabilities of dispersed MWCNTs in mock, inert, and active energetics. In these experimental investigations, the strain and damage sensing abilities of multi-walled carbon nanotube (MWCNT) networks embedded in the binder phase of polymer bonded energetics (PBEs) are evaluated. PBEs are a special class of particulate composite materials that consist of energetic crystals bound by a polymer matrix, wherein the polymer matrix serves to diminish the sensitivity

of the energetic phase to accidental mechanical stimuli as well as to maintain shape. The structural health monitoring (SHM) approach presented in this work exploits the piezoresistive properties of the distributed CNT networks. Major challenges faced during such implementation include the low binder concentrations of PBEs, presence of conductive/non-conductive particulate phases, high degree of heterogeneity in the PBE microstructure, and achieving the optimal MWCNT dispersion. In chapter seven, Ammonium Perchlorate (AP) crystals as the oxidizer, Aluminum grains as the metallic fuel, and Polydimethylsiloxane (PDMS) as the binder are used as the constituents for fabricating PBEs. To study the effect of each constituent on the MWCNT network's SHM abilities, various material systems are comprehensively studied: MWCNT/PDMS (nBinder) materials are first evaluated to study the binder's electromechanical response, followed by AP/MWCNT/PDMS (nPBE) to assess the impact of AP addition, and finally, AP/AL/MWCNT/PDMS (nPBE-AL) to evaluate the impact of adding conductive aluminum grains. Compression samples (ASTM D695) were fabricated and subjected to monotonic compression. Electrical resistance is recorded in conjunction with the mechanical test via an LCR meter. Gauge factors relating the change in normalized resistance to applied strain are calculated to quantify the electromechanical response. MWCNT dispersions, and mechanical failure modes are analyzed via scanning electron microscopy (SEM) imaging of the fracture surfaces. Correlations between the electrical behavior in response to the mechanical behavior are presented, and possible mechanisms that influence the electromechanical behavior are discussed. The results presented herein demonstrate the successful ability of MWCNT networks as structural health monitoring sensors capable of real-time strain and damage assessment of polymer bonded energetics.

Leveraging Carbon Based Nanoparticle Dispersions for Fracture Toughness Enhancement and Electro-mechanical Sensing in Multifunctional Composites

Nishant Prashant Shirodkar

GENERAL AUDIENCE ABSTRACT

The discovery of carbon nanotubes in 1990s popularized a new area of research in materials science called Nanoscience. Carbon nanotubes (CNTs) are one of several forms of Carbon, meaning a differently structured carbon molecule, similar to diamonds, graphite, and coal. In the following decades, several carbon based nanoparticles were discovered or engineered, and with the discovery of Graphene (GNP) in 2010, carbon based nanoparticles were propelled as the most promising class of nanoparticles. High mechanical strength and stiffness, excellent electrical and thermal conductivity, and high strength to weight ratios are some of the unique abilities of CNTs and GNPs which allow their use in a wide array of applications from aerospace materials to electronic devices. In the current work presented herein, CNTs and GNPs are added to polymeric materials to create a nanocomposite material, where the term "composite" refers to a material prepared with two or more constituent materials. The effects of this nanoparticle addition (a.k.a reinforcement) on the mechanical properties of the nanocomposite polymer materials are studied. Specifically, efforts are focused on studying fracture toughness, a material property that describes the material's ability to resist crack growth. Fracture toughness is a critical material property often associated with material and structural failures, and as such it is very important for safe and reliable engineering design of structures, components, and materials. Moving from a single function (i.e. mechanical enhancement) to a more multi-functional role, taking advantage of the excellent electrical and mechanical abilities of CNTs, their structural

health monitoring potential is assessed for use in polymer bonded energetics (eg. solid rocket propellants). When a material undergoes mechanical deformation or damage, the measured electrical properties of the material undergo some change as well. Using sensor networks built with multiple CNTs dispersed within a polymeric material, a whole structure can be made into an effective sensor where by simply monitoring the electrical properties, the extent of material deformation and damage can be known. Such a system is geared towards providing early warning of impending catastrophic material failures thus directly improving the safety during material handling and operations.

Dedication

I dedicate this dissertation to my family. My beloved wife, Ilina, who has been, and continues to be my source of strength, support, love, and inspiration in my life. My loving parents, Prashant and Jyoti Shirodkar, and my brother, Siddhant Shirodkar, whose love, support, and encouragement have always motivated me in my pursuit of knowledge.

Acknowledgments

I would like to express my deepest gratitude to my advisor, Gary D. Seidel. My PhD experience was one of the most amazing learning experiences thanks to my advisor. I was blessed to have his guidance throughout my academic journey at Virginia Tech. He was truly invested in shaping me into a good researcher, and showed me by example the qualities I must imbibe during my doctoral experience. Professionally and personally, I cannot emphasize enough, his enormous role in the success of my doctorate degree.

This endeavor would not have been possible without the help and guidance of my esteemed committee members: Scott W. Case, Michael Philen, Mayuresh Patil, and Shengfeng Cheng. From being my teachers, to advising me continually throughout my doctoral studies, their knowledge, honest feedback, and constructive support was always magnanimously offered, and I would like to express my sincere gratitude for that. Special thanks to Dr. David Dillard at Virginia Tech for providing me, on several occasions, his insight and feedback on my fracture toughness work.

I would also like to thank my colleagues, lab mates, and friends—Fortunately for me, these classifications were not mutually exclusive: Dr. Engin Sengezer, Dr. Krishna Talamadupula, Dr. Stefan Povolny, Neslihan Genckal, Carson Squibb, Kavan Shah, Pranay Anekal, Viswajit Talluru, Rashmi Chawla, Joseph Cunningham, Tony Spinetta, Brenton Morris, Sammi Rocker, Ryan Xi Hao, and Junwen Wang.

I would also like to acknowledge our program sponsors, Air Force Office of Scientific Research (AFOSR: Grant: FA9550-18-1-0433 and Grant no. FA9550-16-1-0198) for their financial support. I would also like to extend my sincere thanks to Mr. Stephen McCartney at the Nanoscale Characterization and Fabrication Lab (NCFL) at Virginia Tech for his immense help. A special thanks to many individuals, who through their own small contributions, have played a large role in my collective doctoral experience at Virginia Tech.

Contents

List of Figures

List of Tables

Part I

Fracture Toughness of Reinforced Epoxies

Chapter 1

Introduction

1.1 Overview of Linear Elastic Fracture Mechanics (LEFM)

In the mid 1900s, a series of structural failures occurring below the material yield stress prompted investigations in to a different type of failure mode: fracture [1]. These failures were characterized by rapid crack growth, often leading to catastrophic consequences. One well known example of such a failure is that of the Liberty ships produced during WWII, particularly the case of the *S.S. Schenectady*, which practically split in half right through the center even before it left the docks [2]. Upon further investigation, this rapid brittle-like failure of the Liberty ships was attributed to: the urgency of production during war-time which resulted in manufacturers using pre-welded steel sheets for ship building, and the overall poor design of the ship interior which was full of square door hatches, both of which ultimately result in severe stress concentrations in the structure. This example highlights the concept of stress concentrations, one of several important factors that may result in a fracture based failure in materials at stresses which are much lower than the material's yield stress. It must be noted that within the scope of the commonly used stress intensity factor approach for fracture analysis, stress concentrations, geometric effects, loading conditions, and intrinsic material properties are all important factors that affect fracture based failure. A stress concentration is a location in a part of a structure where the local stress is much higher than the surrounding region. They can occur at sites with grooves, notches, holes, scratches, geometric irregularities, and sometimes, also due to material heterogeneity. In practice, all materials and structures suffer from imperfections and flaws. These can be artifacts of the manufacturing process, but can also be inherent material flaws. Commonly used materials like steels, ceramics and polymers often contain microscopic cracks, which act as stress raisers or concentrations. When the material is strained, these microscopic cracks can grow in size and ultimately lead to fracture based failure. Works by A. Griffith in the 1950s, supported by the mathematical works of Inglis, are widely considered to be the genesis of the development of fracture mechanics theory. The Griffith theory, after important contributions from Irwin and Orowan, developed into Linear Elastic Fracture Mechanics (LEFM) as we know it today.

LEFM, named as such due to its scope being limited to linear elastic materials, is widely used even today. LEFM helps analyse the stress present in a material in the presence of a crack [1, 3]. The following are the important assumptions that must be satisfied for LEFM to apply:

1. Material is isotropic and linear elastic.
2. Material should undergo very little or no plastic deformation. In other words, the size of plastic deformation zone must be much smaller compared to the geometry of material specimen.

In practice, LEFM can still be applied to materials exhibiting some amount of plastic deformation at the crack tip, however, the plastic deformation has to be very minimal compared to the elastic strain zone, or the K-zone [3]. For materials exhibiting significant plastic deformation at the crack tip, Elastic Plastic Fracture Mechanis (EPFM) is used, which is beyond the scope of this work. As a tool for material characterization LEFM describes formulas for plane stress and plane strain cases under three widely encountered loading scenarios referred to as mode I (opening mode), mode II (shearing mode) and mode III (tearing mode or out-of-plane shearing mode). Detailed explanations and derivations of the said formulas, and the LEFM theory as a whole is not provided for brevity; however, several textbooks and literature are readily available on the subject [1, 3].

1.2 Overview of Testing Methods used for Determination of Fracture Toughness Properties of Materials

The material property that describes a material's resistance to failure by fracture is called fracture toughness. The concepts of fracture mechanics, and the contributions of several researchers have been instrumental in developing a standard method for testing materials under fracture loading [4]. The American Society for Testing and Materials (ASTM) has established several testing standards for various materials according to the modes of loading and the type of material. Mode I or the ”opening mode” is the most widely conducted fracture toughness characterization of materials. Double cantilevered beam (DCB) tests, compact tension (CT) tests and Single edge notch bend (SENB) test are some common tests described in ASTM D5528 and ASTM D5045 [5, 6]. Mode II test standards (ASTM D7905) were not developed until recently in 2014, while mode III test standards (ASTM D6671) were developed in 2000s [7, 8]. The cost and complexity of material characterization under mode II and III loading are some reasons why mode I is more commonly investigated than the former two modes.

In this work (Part I), mode I fracture toughness characterization is primarily the focus of all investigations. The compact tension geometry is used as it can be easily scaled down to smaller sizes, thus making it cost efficient to conduct several experimental trials. The ASTM D5045 standard for plane strain fracture toughness testing of plastic materials is used. This test method characterizes the resistance of a material to fracture in a neutral environment in the presence of a sharp crack under mode I loading conditions, such that the stress state near the crack front approaches plane strain, and the crack-tip plastic region is small compared with the crack size and specimen dimensions in the constraint direction. With plane strain conditions ahead of the crack tip, the resulting fracture toughness value is believed to represent a lower limiting value of fracture toughness [5]. Given below are important assumptions which must be satisfied to apply the analysis and formulas given in the ASTM standard correctly [5].

1. Material must sufficiently behave in an linear elastic manner.

2. A state of plane strain must exist at the crack tip, and thus specimen thickness must be adequate.

3. A sharp crack must be present at the crack tip such that a minimum value of toughness is obtained

Several other minute details can be found in the ASTM document which elaborate on the process of specimen geometry design, and acceptable ranges of sample features like initial crack length, thickness and width.

1.3 Approaches for Fracture Toughness Enhancement in Epoxy Matrix Composites: A Literature Review

(The following section is an excerpt taken from "Nishant Shirodkar, Shengfeng Cheng, Gary D. Seidel - Enhancement of Mode I fracture toughness properties of epoxy reinforced with graphene nanoplatelets and carbon nanotubes, Composites Part B: Engineering, Volume 224, 2021, 109177, ISSN 1359-8368, `https://doi.org/10.1016/j.compositesb.2021.109177`*.* *(*`https://www.sciencedirect.com/science/article/pii/S1359836821005552`*)". This paper is a published manuscript authored by the Nishant Shirodkar, who is also the author of this dissertation document.)*

Carbon-based nanoparticles have spurred a lot of interest in the composites research area because of their excellent mechanical, thermal, and electrical properties, making them a very good choice as filler materials. Even at low weight concentrations, nanoparticles such as carbon nanotubes (CNTs) and graphene nanoplatelets (GNPs) enable significant enhancement of the matrix material's mechanical properties. Owing to their multifunctional capabilities, CNT and GNP reinforced nanocomposites have found applications in a variety of areas such as energy storage, structural composites, electrical packaging, and flexible electronics [9, 10]. Structural composites, especially fiber reinforced polymer composites (FRPs) which consist of high strength carbon or glass fibers embedded in a weaker polymer matrix, are a key focus area for the application of CNTs and GNPs as they can be readily introduced into the binder during processing. Traditional FRPs suffer from several drawbacks such as weak interlaminar strength, fiber-matrix debonding, and poor fracture toughness properties. Compared with common metals such as steels, the fracture toughness of polymers is typically an order of magnitude lower [11]. Given that

FRPs are typically less dense than metals, but have comparable stiffness and strength, establishing ways to systematically improve their fracture toughness will make them well rounded structural materials. In the past two decades, several efforts have been made towards enhancing the fracture toughness of FRPs, as well as polymer composites in general [12, 13, 14, 15, 16].

In efforts to improve the fracture properties of FRPs, key failure mechanisms such as interlaminar delamination, fiber-matrix debonding, and matrix cracking have been identified. Methods such as inter-layer stitching and ply-pinning are introduced to address the issue of delamination. Ravandi *et al.* investigated the effects of through-thickness stitching by applying flax and cotton stitches through flax fiber/epoxy composite laminates [17]. The stitches act as bridging elements through the laminates and bridge the crack once it is initiated, thus lending it an added ability to resist crack growth. A 21% increase in fracture toughness was obtained by this method. In addition to delamination mitigation, methods to reduce fiber-matrix debonding have also been investigated. One natural thought is to increase the ability of the fibers to bond with the matrix for them to carry as much load as possible, thus disallowing crack growth and forming very strong crack bridging networks. Yildiz *et al.* grew CNTs on glass fibers and used these fuzzy fibers to improve fiber-matrix bonding [18]. A 113% increase in fracture toughness was observed. Several other works have explored similar techniques such as fuzzy carbon fibers and have found promising fracture toughness enhancements [19, 20]. However, the processing involved in growing CNTs or other nanoscale features on fibers typically results in a strength penalty for the fibers, making them weaker than their unaltered counterparts [19, 21]. A different reinforcing strategy involves strengthening the matrix material by incorporating additional rubbery or soft phases in the form of block copolymers. These softer phases endure much higher deformations than the surrounding brittle matrix, thereby slowing the advancement of cracks. Kamar *et al.*

incorporated a triblock copolymer into carbon fiber reinforced epoxy polymer composites (CFRPs) to improve their mode-I fracture energy [22]. The copolymer, a triad of polystyrene-polybutadiene-polymethylmethacrylate, was used to modify the epoxy matrix. Samples with several phr (parts per hundred resin) concentrations were tested. It was observed that a copolymer concentration of 10 *phr* resulted in a 290% increase in fracture energy. Bakar *et al.* experimented with the addition of plasticizers to unsaturated polyester resins and studied its effect on the resulting materials' mechanical properties [23]. A 45% increase in fracture toughness was observed at a concentration of dioctyl phthalate of 5 phr. Despite the observed increase in fracture toughness brought about by the addition of copolymers, complexities and compatibility issues between the added copolymers and the matrix materials limit the applicable range of this approach [24, 25, 26, 27].

Another method of reinforcing a matrix material involves dispersing small amounts of nanoparticles (carbon-based, metallic, etc.) in the matrix. Gojny *et al.* evaluated single-walled, double-walled, and multi-walled CNTs doped epoxy nanocomposites [14]. A maximum 43% increase in fracture toughness was observed for a nanocomposite reinforced with double-walled CNTs at 0.1% weight concentration. Kumar *et. al* investigated the enhancements caused by adding GNPs to epoxy and observed a $\sim$200% increase in Mode I fracture toughness at 0.5% weight concentration [28]. Additional efforts have explored other nanoparticles based on silica, graphene, and copper, and zinc nanowires. Significant enhancements have been reported even with small amounts of nanofillers [13, 15, 16]. The approach of adding nanofillers has several advantages. First, a wide range of nanoparticles can be chosen to reinforce a certain polymer. Second, the low content of nanofillers that are needed for reinforcement only leads to a marginal change of the matrix weight, which is desirable in many applications. Finally, many nanofillers also possess other functionalities (e.g., electrical and thermal functions) in addition to mechanical reinforcement, thus lending the composite a multifunctional capability [29, 30, 31, 32, 33, 34, 35, 36, 37, 38, 39, 40, 41, 42, 43, 44, 45, 46, 47, 48, 49, 50, 51, 52, 53, 54, 55, 56].

1.4 Defining the Problem Statement: Experimental Investigation of Fracture Toughness Enhancement in Epoxy Nanocomposites

Figure 1.1 is a compilation of various fracture toughness data for CNT-Epoxy, GNP-Epoxy and CNT/GNP-Epoxy nanocomposites obtained from the literature[14, 24, 28, 57, 58, 59, 60, 61, 62, 63, 64, 65, 66, 67, 68, 69, 70, 71, 72]. This plot highlights that while nanoparticle-reinforced epoxy composites have been studied to some extent, there is still no clear correlation revealed between the degree of enhancement and the concentration of CNTs and GNPs. The possible synergy between the two fillers is not well established and poorly understood. Additionally, the factors that affect fracture toughness, such as pre-crack characteristics and nanofiller particle sizes have not been studied in detail. This work aims to systematically study the enhancement of fracture toughness in epoxy-based nanocomposites. The underlying toughening mechanisms such as crack bridging, crack deflection, and crack branching are investigated. The reinforcing capabilities of CNTs, GNPs, and CNT/GNP mixtures as the nanofillers are quantified with neat epoxy as the baseline. The synergistic effects between CNTs and GNPs are investigated to possible enhancement behavior. The effect of different nanofiller particle sizes are also investigated. Lastly, an extensive study characterizing the effects of pre-crack characteristics on the initiation fracture toughness will be conducted to explain fracture behavior and scatter in experimental data.

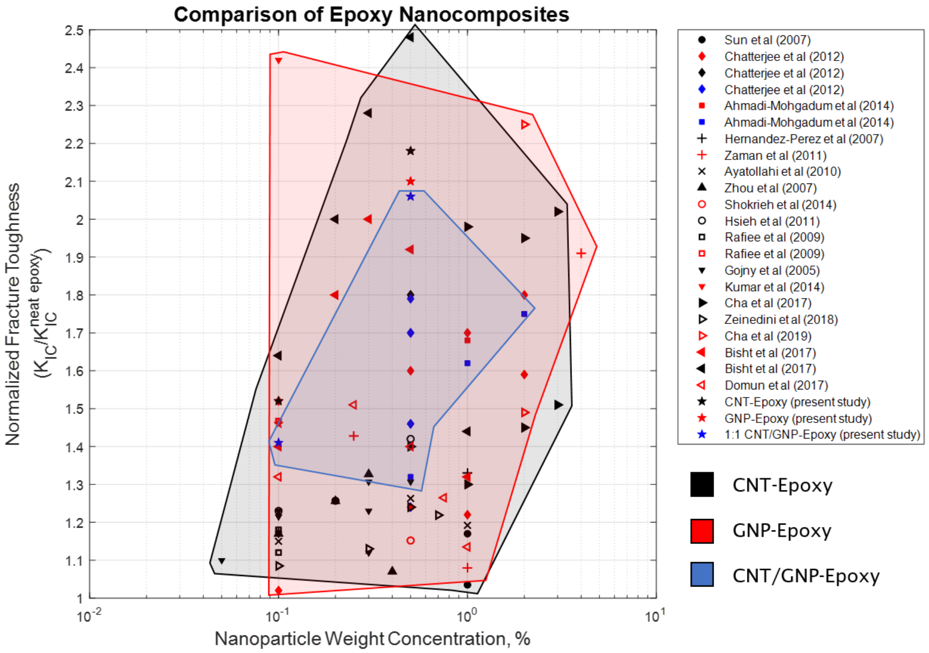

Figure 1.1: Fracture toughness data for various CNT, GNP, and CNT/GNP-Epoxy nanocomposites, normalized by the value for neat epoxy, were collected from the literature and plotted against the nanofiller weight concentrations.

Chapter 2

Initiation Fracture Toughness Enhancement in Carbon Nanotubes (CNTs) and Graphene (GNP) Reinforced Epoxies

(The following chapter contains sections taken from "Nishant Shirodkar, Shengfeng Cheng, Gary D. Seidel - Enhancement of Mode I fracture toughness properties of epoxy reinforced with graphene nanoplatelets and carbon nanotubes, Composites Part B: Engineering, Volume 224, 2021, 109177, ISSN 1359-8368, `https://doi.org/10.1016/j.compositesb.2021.109177`. (`https://www.sciencedirect.com/science/article/pii/S1359836821005552`)". This paper is a published manuscript authored by the Nishant Shirodkar, who is also the author of this dissertation document.)

2.1 Preparation and Testing of Epoxy Nanocomposite Samples

2.1.1 Materials

In this work, a two-part epoxy matrix material was used: EPON 862, a bisphenol-F resin, and EPIKURE Curing Agent W, an aromatic amine curing agent. Both resin and curing agent are supplied by Hexion. As reported by the manufacturer, the epoxy used has good performance characteristics, including low viscosity (2200 cP) at room temperature, low moisture absorption (2-2.5 wt%), and over 20 hours of working life at room temperature. Pristine multi-walled CNTs (MWCNTs) were supplied by Cheap Tubes Inc. The MWCNTs have a reported purity of >95% with some iron and sulfur residuals (residual particle sizes $\sim$ 80 nm), a reported outer diameter of 15±5 nm and an inner diameter of 7±2 nm, and an average length of 3±2 μm. xGNP Grade H GNPs were supplied by XGSciences and have a reported average thickness $\sim$ 15 nm and an average particle diameter of 5 μm. The GNP particles have a reported purity of over 95% with some residual acid contents. The CNTs and GNPs are not functionalized and are used in their pristine conditions for this study.

2.1.2 Fabrication

Positive counter molds were designed as per ASTM D5045 guidelines [5] and were 3D printed via a high-resolution Polyjet printer (Connex 3 Objet 500). Silicone molds were then prepared from the 3D printed template and used for the fabrication of CT samples. CNT and/or GNP doped epoxy nanocomposites with varying nanoparticle weight concentrations were fabricated to evaluate their effect on the fracture toughness properties of the reinforced epoxy. Table 2.1 lists the material compositions of the seven different material systems fabricated for this study. Neat epoxy samples (i.e. samples without any nanoparticle content) were fabricated by mixing the resin and curing agent at a ratio of 100:26.4 by weight, as prescribed by the manufacturer. After thorough mechanical mixing for approximately 10 minutes, the mixture was heated to 90°C and maintained at that temperature to reduce its viscosity; it was simultaneously degassed at 90 kPa vacuum for 45 minutes. It has been noted in the literature that reduced viscosity aids in proper degassing [28]. The silicone molds were sprayed with a mold release agent and then the degassed mixture was poured into the molds. The samples were cured in an oven (MTI DZF-6020-HT) at $121°C$ for 2 hours and post cured at 176°C for an additional 2 hours.

To prepare nanocomposite samples, appropriate quantities (see Table 2.1) of the nanoparticles were measured in a glass beaker. Measured quantities of EPON 862 resin epoxy were added to the nanoparticles and the two were mixed using a high shear mixer at 2000 rpm for 45 minutes. During the high shear mixing process, the resin and nanoparticle mixture was held at $90°C$ to reduce its viscosity and aid the nanoparticle diffusion. In order to further disperse the nanoparticles, the mixture was ultra-sonicated (QSonica Q500A) in an ice-chilled water bath at 20kHz and 30% amplitude for 10 minutes. After sonication, the required quantities of the curing agent were added and mixed with the resin-nanoparticle mixture using a high shear mixer at 2000 rpm for 10 minutes at room temperature. The resulting mixture was then degassed using the same parameters as for the neat epoxy samples. The subsequent processes for pouring the mixture in the molds and curing the samples were also consistent with the processes for the neat epoxy samples. The Nanocomposite samples were fabricated in batches of five samples each for the seven different material systems.

Table 2.1: Material Compositions

Material Systems	CNTs, %wt	GNPs, % wt	Epoxy Matrix, % wt
Neat Epoxy	0	0	100
0.1-CNT-Epoxy	0.1	0	99.9
0.1-GNP-Epoxy	0	0.1	99.9
0.1-CNT/GNP-Epoxy	0.05	0.05	99.9
0.5-CNT-Epoxy	0.5	0	99.5
0.5-GNP-Epoxy	0	0.5	99.5
0.5-CNT/GNP-Epoxy	0.25	0.25	99.5

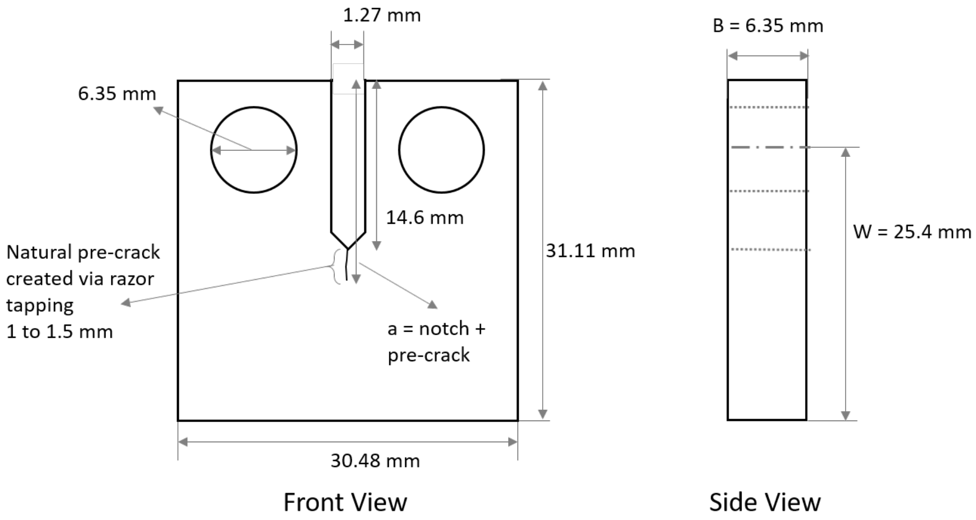

Figure 2.1: Graphical illustration of the fabricated CT samples shown with their geometrical dimensions in millimeters (mm).

2.1.3 Sample Preparation

CT specimens were prepared according to ASTM D5045 [5] to evaluate the fracture toughness properties of the nanocomposites. Figure 2.1 shows a graphical illustration of the CT samples with their geometric dimensions. The samples were cast using the silicone molds with a notch built into the mold. The thicknesses of the samples were within the prescribed ASTM guidelines such that a plane strain condition can be assumed at the crack tip. Additionally, raised features like the meniscus formation around the pin-holes and sample edges, an artifact of the casting process, were sanded to achieve a uniform thickness across the sample. Because of the limitations of the casting process, the notch tip of the cast samples was not as sharp as required by ASTM D5045. A sharp pre-crack is essential for a valid fracture toughness test because (a) a blunt crack tip results in a pseudo increase of the measured fracture toughness values [28] and (b) it violates the assumption of an ideal crack underlying linear elastic fracture mechanics (LEFM), the theory on which the calculations of the critical stress intensity factor, K_{IC}, and critical fracture energy, G_{IC}, are based [5, 73]. To create a sharp pre-crack, ASTM D5045 guidelines were followed [5]. The cast sample's blunt notch tip was sharpened with a knife-edged file. The filed notch tip was sharpened further by sawing with a thin serrated blade. Finally, a sharp, natural pre-crack was initiated by tapping the notch tip with a razor blade. Figure 2.2 shows images, acquired via digital microscopy, of a sample at every stage of the sharpening process of the notch tip and the creation of the pre-crack. In Figure 2.2(d), the thin line extending beyond the machined notch tip is the sharp, natural pre-crack created by the razor blade tapping method.

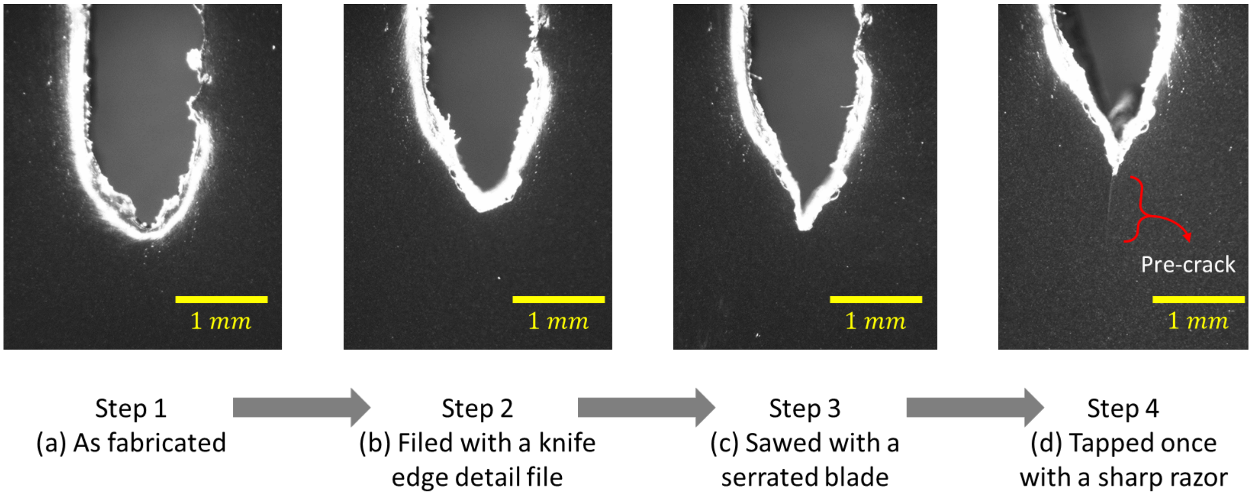

Step 1
(a) As fabricated

Step 2
(b) Filed with a knife edge detail file

Step 3
(c) Sawed with a serrated blade

Step 4
(d) Tapped once with a sharp razor

Figure 2.2: Digital microscope images of a CT sample undergoing the process of notch-tip sharpening and pre-crack creation. Left to Right: cast sample, sample after filing, sample after sawing, and sample after razor blade tapping.

2.1.4 Fracture Toughness Testing

Fracture toughness tests were conducted in an INSTRON universal double-columned test frame via a displacement controlled test at a displacement rate of 2 mm/min. The displacement and the corresponding force, measured using a load cell, exerted on the sample were recorded until the sample failed[1]. In this study, a sample was considered to be failed if the instantaneous load carrying capacity dropped by more than 80% from the peak load [2]. Through trial and error, it was observed that all samples cracked in half shortly upon meeting this criterion and hence, could be considered to be practically failed.[3] A batch of five samples for each material system was tested to account for the statistical variation in the load-displacement curves. The gathered data was analyzed and the peak load, fracture displacement, K_{IC}, and G_{IC} were calculated for every sample using the process outlined by ASTM standards.

2.2 Results and Discussion

2.2.1 Qualitative/Visual Assessments

Figure 2.3 shows photographs of the fabricated CT samples. The addition of CNTs and/or GNPs lent a distinctive black hue to the composite samples as opposed to the nominally

---

[1] For the load cell that was used (5 kN), the measurement accuracy is 0.10% of the measured value. For a 100 N load, the error would be +/- 0.1 N. With that in mind, the data presented has been truncated after the decimal point. For example, 89.56 N becomes 86 N. For the displacement measurements, the Instron manufacturers report an accuracy of 0.001 mm. Hence, only 2 digits after the decimal point are reported. This has been done in subsequent chapters as well.

[2] This study investigated the initiation fracture toughness of the materials and hence, the load and displacement data of the material past its peak load was not employed in the calculations of the fracture toughness values

[3] In some of the tested CNT-Epoxy samples, the crack did not propagate all the way through the sample despite registering a 80% load drop. However, the samples broke as they were being dismounted from the test fixture and hence, could be considered to be practically failed.

semi-transparent amber hue of the neat epoxy. Even at 0.1% weight concentration, there was a marked change in the color. At 0.5% weight concentration, increased opaqueness and a slightly darker black hue were observed. Some bubbles were observed around the outer edge of some samples (see Figure 2.3). However, any samples with bubbles along the crack path—identified by inspecting the fracture surface after testing—were discarded and the corresponding data were excluded from the analysis.

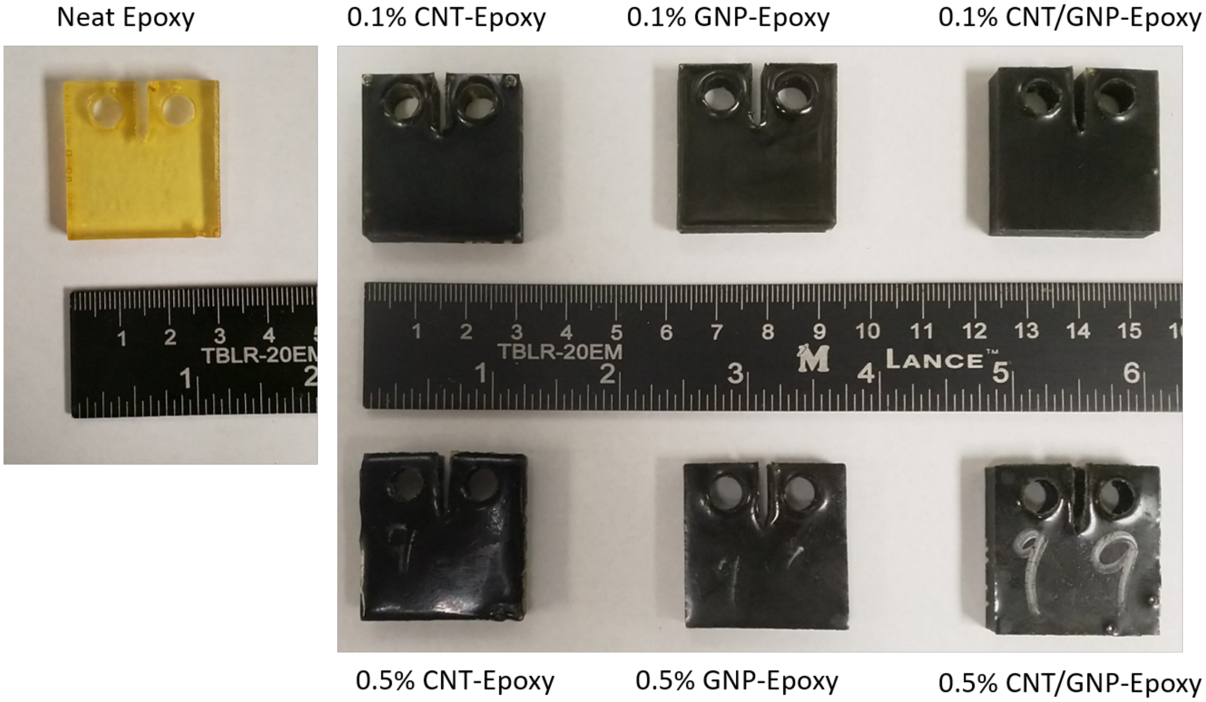

Figure 2.3: Photographs of representative CT samples of the seven material systems fabricated for this study.

2.2.2 Mechanical Properties

Figures 2.4(a-c) show the mean load-displacement curves for the CNT-Epoxy, GNP-Epoxy, and CNT/GNP-Epoxy nanocomposites, respectively, as well as the neat epoxy in each case as a reference. The plotted error bars represent data within two standard deviations of the mean (plus and minus one standard deviation). The load-displacement data has been post-processed and the value of displacement has been corrected according to ASTM D5045 procedures [5]. Specifically, the contribution from the initial non-linear loading regime, which can be attributed to sample compression, system compliance, and loading-pin penetration, has been subtracted from the measured raw value of displacement. The data in Figure 2.4 therefore represents the linearized load-displacement curves, which are plotted using the slope of the linear part of a load-displacement curve, the peak load and the corrected fracture displacement values.

The neat epoxy samples have an average peak load of 86 ± 5 N and an average fracture displacement of 0.19 ± 0.01 mm. These samples serve as a baseline for further comparisons. Adding 0.1% CNTs (by weight) to the epoxy resulted in ∼53% increase in load-carrying capacity and ∼36% increase in fracture displacement, with an average peak load of 132 N and average fracture displacement of 0.26 mm. Increasing the CNT weight concentration to 0.5% led to ∼120% increase in peak load (to 190 N) and ∼89% increase in displacement (to 0.36 mm). For the GNP-Epoxy nanocomposite samples at 0.1% weight concentration, the peak load was enhanced by ∼46% to 126 N and the fracture displacement was increased by ∼32% to 0.25 mm. Increasing the GNP weight concentration to 0.5% makes the enhancement factor of the peak load and fracture displacement to be ∼111% (to 182 N) and ∼78% (to 0.34 mm), respectively. Nanocomposites reinforced with a mixture of nanofillers are also of interest as synergistic effects may occur between nanofillers with different geometrical characteristics. CNTs and GNPs offer a good opportunity to explore such effects as CNTs are filament-like, while GNPs have a platelet shape. The different aggregation behavior among CNTs and GNPs may lead to new reinforcement mechanisms not involved in nanocomposites based on one type of nanofillers. For the CNT/GNP-Epoxy samples at 0.1% weight concentration and 1:1 ratio of CNT:GNP, the

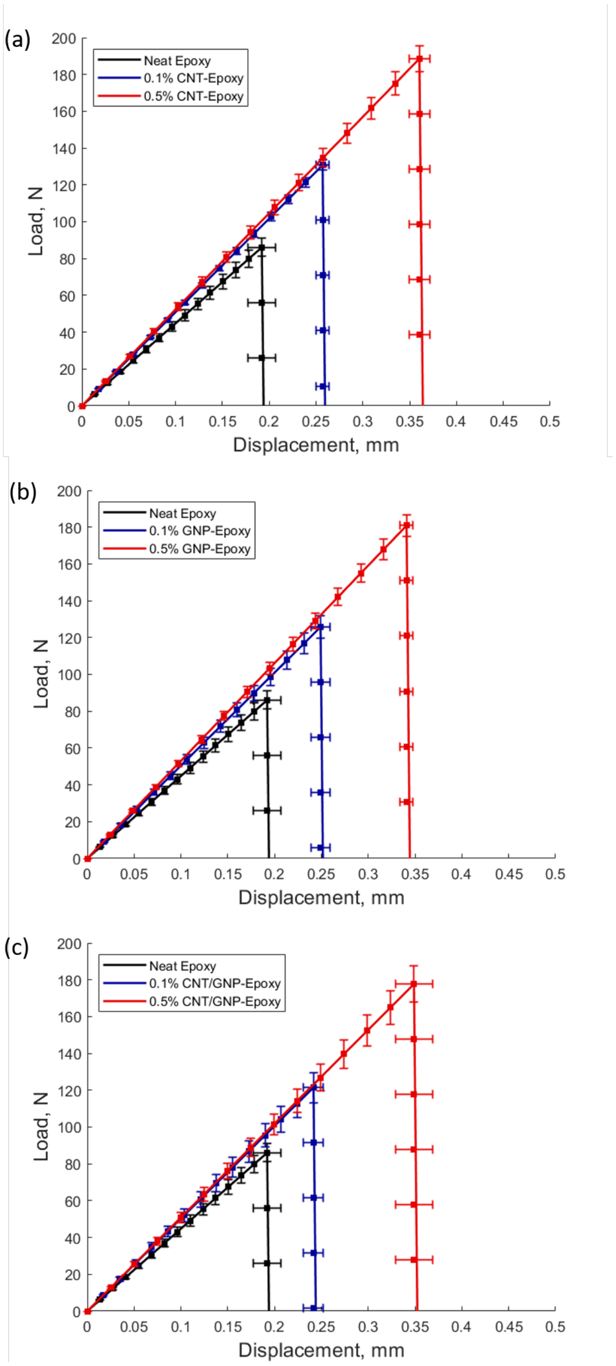

Figure 2.4: Linearized load-displacement curves for (a) 0.1% and 0.5% CNT-Epoxy, (b) 0.1% and 0.5% GNP-Epoxy, and (c) 0.1% and 0.5% CNT/GNP-Epoxy. The result for the neat epoxy is included in each plot as a baseline.

peak load was increased by ∼41% to 122 N and the fracture displacement was increased by ∼26% to 0.24 mm. When the weight concentration of the CNT/GNP mixture was increased to 0.5%, the peak load and fracture displacement were enhanced further, by ∼108% to 179 N for the former and ∼84% to 0.35 mm for the latter. Table 2.2 summarizes the average peak loads and fracture displacements of all the material systems tested, with the degree of enhancement quantified using the neat epoxy as a reference. The data are presented with the associated error bars (representing one standard deviations of the mean) to indicate the extent of variability or repeatability of the data from CT tests. It should be noted that the peak load value is not the indicator of a material's tensile strength, but rather its maximum load-carrying capacity in the presence of a crack. In other words, it represents the maximum amount of load a material can bear before a crack is able to grow in it and eventually lead to its failure.

Table 2.2: Peak loads and fracture displacements of all the material systems

Material System	**Peak Load (N)**	**% Increase**	**Fracture Displacement (mm)**	**% Increase**
Neat Epoxy	86 ± 5	-	0.19 ± 0.01	-
0.1-CNT-Epoxy	132 ± 2	∼53	0.26 ± 0.01	∼36
0.1-GNP-Epoxy	126 ± 6	∼46	0.25 ± 0.01	∼32
0.1-CNT/GNP-Epoxy	122 ± 8	∼41	0.24 ± 0.01	∼26
0.5-CNT-Epoxy	190 ± 6	∼120	0.36 ± 0.01	∼89
0.5-GNP-Epoxy	182 ± 5	∼111	0.34 ± 0.007	∼78
0.5-CNT/GNP-Epoxy	179 ± 4	∼108	0.35 ± 0.01	∼84

As a straight comparison, the average peak loads and fracture displacements are also shown as bar plots in Fig. 2.5. It shows that the addition of CNTs, GNPs, and CNT/GNP mixtures to an epoxy matrix enhances its mechanical properties to resist fracture. The enhancement is more significant at 0.5% weight concentration of the nanofillers than at

0.1% weight concentration. At a given weight concentration, CNTs slightly outperforms GNPs, while both lead to enhancements marginally stronger than the CNT/GNP mixtures. The only exception is the fracture displacement of the CNT/GNP-Epoxy sample at 0.5% weight concentration, which is slightly larger than that of the GNP-Epoxy sample at the same weight concentration.

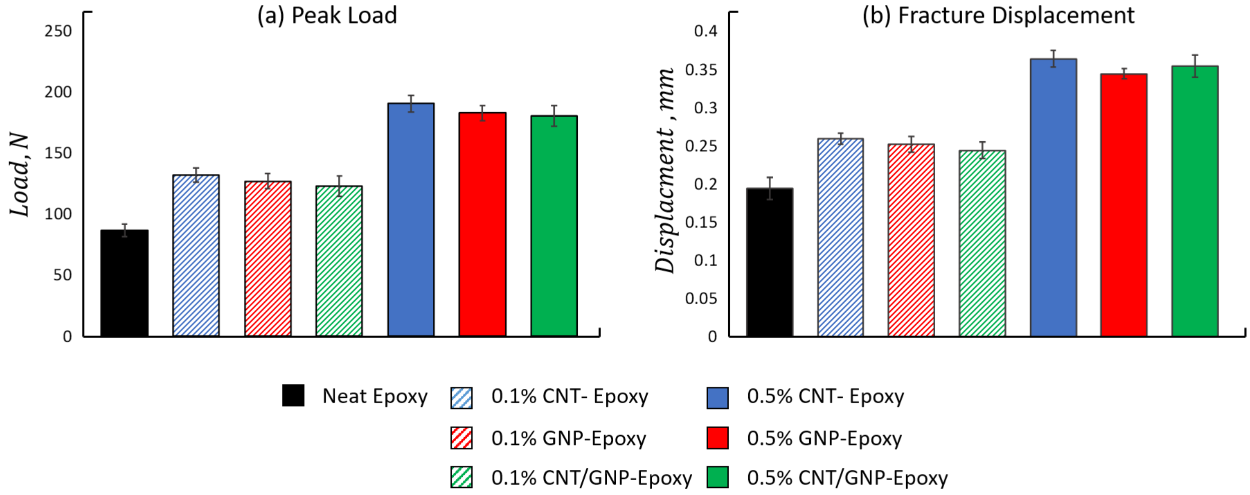

Figure 2.5: Bar plots comparing (a) average peak load and (b) fracture displacement for the seven material systems. Error bars shown over every bar represent two standard deviations of the mean.

2.2.3 Fracture Toughness and Fracture Energy

To further quantify the initiation fracture toughness of the nanocomposites studied here, Mode I critical stress intensity factor, K_{IC}, was calculated using Equation 2.1, where P is the peak load, B is the average sample thickness, W is the specimen width as defined by ASTM D5045, and $f(x)$ is an empirical calibration factor dependent on crack length, a, and specimen width, W of each sample. Equation 2.2 shows the formula for $f(x)$ where $x = a/W$.

$$K_{IC} = \frac{P}{BW^{1/2}} f(x) \tag{2.1}$$

$$f(x) = \frac{(2+x)(0.886 + 4.64x - 13.32x^2 + 14.72x^3 - 5.6x^4)}{(1-x)^{3/2}} \tag{2.2}$$

Using Equation 2.1 the value of K_{IC} was found to be 0.75 ± 0.04 MPa· $m^{1/2}$ and is consistent with the manufacturer's reported value of 0.8 MPa· $m^{1/2}$ [74]. The values of K_{IC} were 1.14 MPa· $m^{1/2}$, 1.10 MPa· $m^{1/2}$, and 1.06 MPa· $m^{1/2}$ for the CNT, GNP, CNT-GNP reinforced epoxy at 0.1% weight concentration, corresponding to an enhancement factor of 52%, 46%, and 41% with respect to the neat epoxy, respectively. At 0.5% weight concentration, CNT-Epoxy, GNP-Epoxy and CNT/GNP-Epoxy samples achieved a ~118% (to 1.64 MPa· $m^{1/2}$), ~110% (to 1.58 MPa· $m^{1/2}$) and ~106% (to 1.55 MPa· $m^{1/2}$) increase in fracture toughness. Table 2.3 summarizes the average K_{IC} values and the associated error bars, corresponding to one standard deviation, for all the material systems tested. Compared with the neat epoxy, the reinforced samples showed a marked increase in initiation fracture toughness, even at a weight concentration as low as 0.1%.

Table 2.3: Comparison of the critical stress intensity factor (K_{IC}) and fracture energy (G_{IC}) of all the material systems

Material Systems	**K_{IC} (MPa· $m^{1/2}$)**	**% Increase**	**G_{IC} (J/m^2)**	**% Increase**
Neat Epoxy	0.75 ± 0.04	-	247 ± 29	-
0.1-CNT-Epoxy	1.14 ± 0.02	~52	502 ± 16	~103
0.1-GNP-Epoxy	1.10 ± 0.05	~46	469 ± 39	~89
0.1-CNT/GNP-Epoxy	1.06 ± 0.07	~41	440 ± 49	~78
0.5-CNT-Epoxy	1.64 ± 0.05	~118	1017 ± 65	~311
0.5-GNP-Epoxy	1.58 ± 0.05	~110	923 ± 43	~273
0.5-CNT/GNP-Epoxy	1.55 ± 0.04	~106	927 ± 36	~275

Mode I critical fracture energy was calculated using Equation 2.3, where U is the corrected strain energy (i.e. the area under the linearized load-displacement curve), B is the average sample thickness, W is the specimen width, and $\phi(x)$ is an empirical energy calibration factor. The expression for $\phi(x)$ is given in Equation 2.4.

$$G_{IC} = \frac{U}{BW\phi(x)} \tag{2.3}$$

$$\phi = \frac{(1.91 + 19.11x - 2.51x^2 - 23.22x^3 + 20.54x^4)(1 - x)}{(19.11 + 5.02x - 69.67x^2 + 82.12x^3)(1 - x) + 2(1.91 + 19.11x - 2.51x^2 - 23.22x^3 + 20.54x^4)} \tag{2.4}$$

The value of G_{IC} was determined to be 247.4 J/m^2 for the baseline neat epoxy samples. For the reinforced samples at 0.1% weight concentration of the nanofillers, the fracture energy was increased by ~103% (to 502.92 J/m^2) for CNT-Epoxy, ~89% (to 469 J/m^2) for GNP-Epoxy. and ~78% (to 440.53 J/m^2) for the CNT/GNP-Epoxy samples. At the higher weight concentration of 0.5% , the CNT-Epoxy, GNP-Epoxy, and CNT/GNP-Epoxy samples exhibited an increase in fracture energy by ~311% (to 1017.6 J/m^2), ~273% (to 923 J/m^2) and ~275% (to 927.14 J/m^2), respectively. Table 2.3 summarizes all the average G_{IC} values and the associated error bars. The possible mechanisms underlying the observed enhancements of the fracture properties of the reinforced materials will be discussed later in the paper.

A direct comparison of fracture toughness (K_{IC}) and fracture energy (G_{IC}) is included in Figure 2.6 as bar plots. Similar trends as those in Figure 2.5 are observed. Enhancements of K_{IC} and G_{IC} are found for all the reinforced samples. For the reinforced composites containing the same fraction of nanofillers in terms of weight, CNTs perform the best, followed by GNPs, while the CNT/GNP mixtures exhibit an enhancement slightly weaker than both CNTs and GNPs. In other words, there appears to be no synergy among CNTs

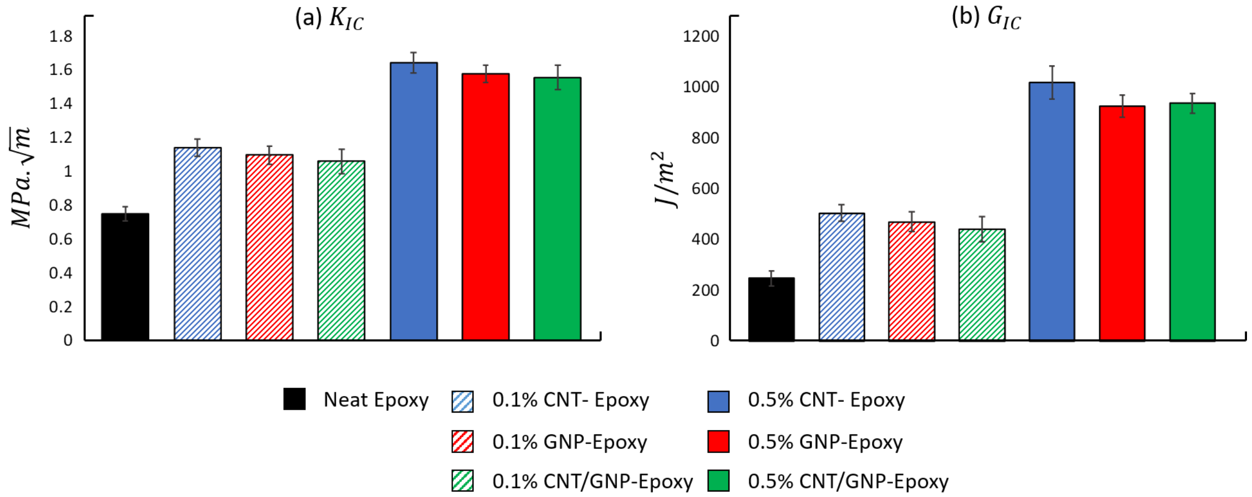

Figure 2.6: Bar plots comparing (a) fracture toughness (K_{IC}) and (b) fracture energy (G_{IC}) for the seven material systems. Error bars represent two standard deviations of the mean.

and GNPs as reinforement agents. However, this may be due to the 1:1 mass ratio between the two nanofillers used in the mixtures in this study. The connection between mass ratio and possible synergistic effects in CNT/GNP mixtures needs to be explored with more studies.

2.2.4 Fracture Surface Analysis

Scanning Electron Microscopy (SEM) was used to image the post-failure surfaces of the fractured samples and some results were included in Figure 2.7. These images were taken at a magnification of 500x. The neat epoxy samples exhibit smooth surfaces, with almost no features or roughness after fracture, which indicates unobstructed crack propagation after initiation (Figure 2.7(a)). In comparison, the CNT-Epoxy samples, at both 0.1% and 0.5% weight concentrations, have visible clusters of CNTs on the fracture surface (Figure 2.7(b)). Minor surface roughness near the clusters is also observed. In Figures 2.8(a-ii, a-iii) where the fracture surfaces were imaged at higher magnifications (5000x and 20,000x), CNTs are

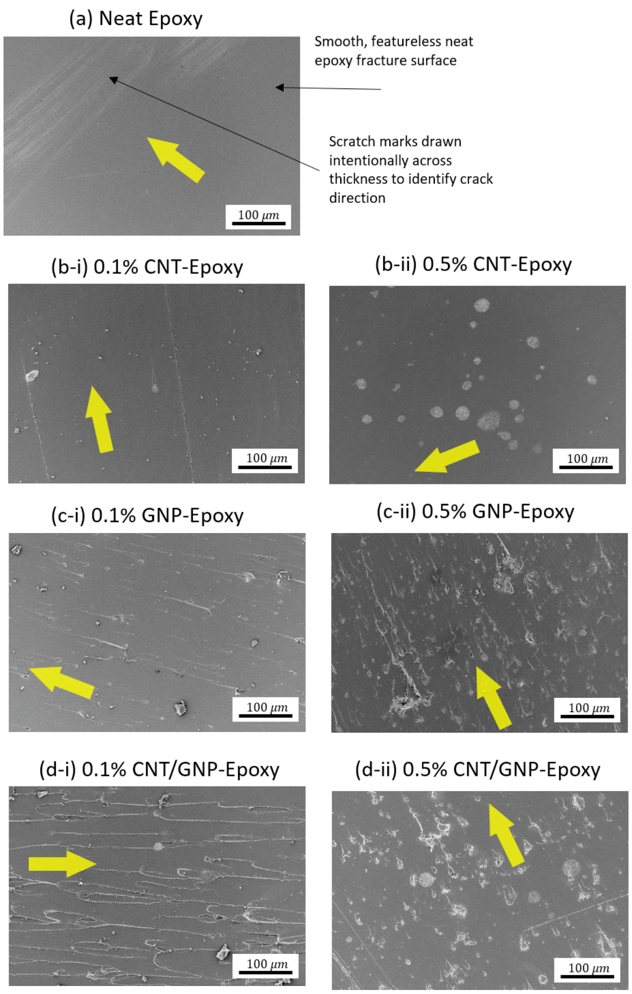

Figure 2.7: SEM images of the fracture surfaces of all the tested materials: (a) Neat Epoxy, (b-i,ii) 0.1% and 0.5% CNT-Epoxy, (c-i,ii) 0.1% and 0.5% GNP-Epoxy, (d-i,ii) 0.1% and 0.5% CNT/GNP-Epoxy. In each image, the direction of the yellow arrow indicates the direction of crack propagation.

clearly visible and the epoxy has impregnated the CNT clusters quite well. Instances of CNT pullouts are also observed, indicating crack bridging across the fracture surface. Further, it is believed that the wavy nature of the CNTs observed in Figures 2.8(a-iii, c-iii) can lead to mechanical interlocking behavior, thereby making CNT pullouts difficult and resulting in stronger crack bridging elements.

Compared with the CNT-Epoxy samples, the GNP-Epoxy samples have visibly more surface

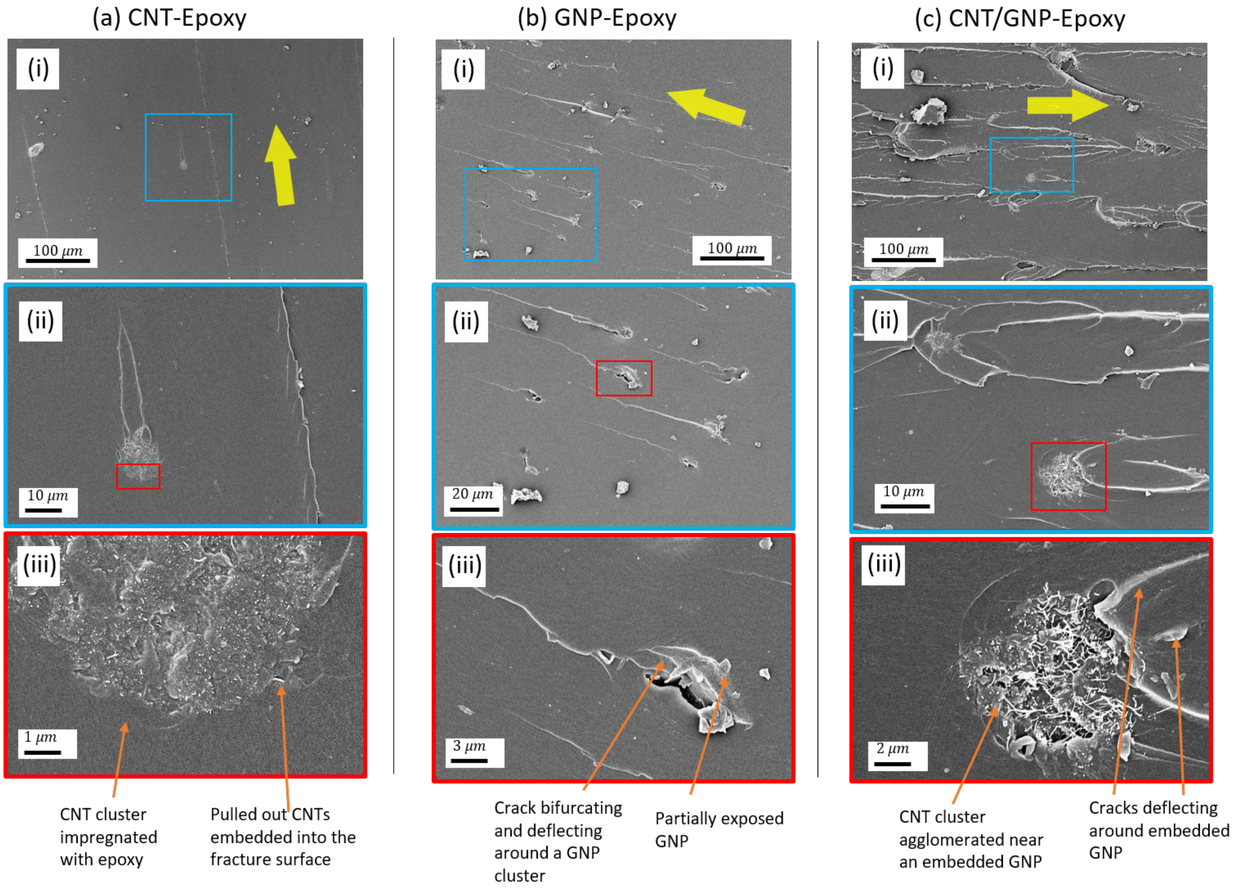

Figure 2.8: Sequential high magnification SEM images of the fracture surfaces of (a) 0.1% CNT-Epoxy, (b) 0.1% GNP-Epoxy, (c) 0.1% CNT/GNP-Epoxy. The images in the top, middle, and bottom rows are taken at 500x, 5000x, and 20,000x magnification, respectively. Colored boxes highlight the approximate regions magnified further. In each image, the direction of the yellow arrow indicates the direction of crack propagation.

roughness, as seen in Figures 2.7(c-i, c-ii). The two dimensional GNPs are much stronger and stiffer than the surrounding epoxy. Thus, it is energetically favorable for an advancing crack front to deviate around GNPs, rather than go through them. In this sense, the embedded GNPs act as barriers to obstruct the advancement of cracks. The resulting crack deviation or deflection creates rough surface features in its wake. Such roughness has been observed by others who have also attributed it to crack deflection [75, 76]. The fracture surface was found to be more rough as the nanofiller weight concentration was increased to 0.5%; this is indicative of more crack deflection occurring along the crack path. It must be noted that as a crack circumvents a GNP, it may conceal a GNP under the fracture surface, which makes spotting GNPs via SEM harder than detecting CNTs. A few instances of partially exposed GNPs are visible in Figures 2.8(b-ii,iii), wherein cracks can be seen bifurcating and deflecting around the GNPs.

SEM images of the fractured surfaces of the CNT/GNP-Epoxy samples shown in Figures 2.8(c-i, c-ii, c-iii) reveal markers indicating the occurrence of both crack mitigation processes: deflection and bridging. The former can be deduced from the increased surface roughness and the latter is confirmed by the presence of CNT clusters and pullouts on the fractured surfaces [75, 76]. Figure 2.8(c-iii) shows an instance of CNTs agglomerated around/near a GNP (most likely a group of GNPs situated close to each other). Exposed pulled-out CNTs are visible in front of the bifurcation point of the crack, suggesting that both crack bridging and deflection may have occurred in that region. Furthermore, SEM images shown in Figure 2.7(d-i, d-ii) also reveal that as the weight concentration of the nanofillers is increased, the fractured surface becomes rougher and more CNT clusters can be observed on the surface.

2.2.5 Discussion on Toughening Mechanisms

CNT, GNP, and CNT/GNP reinforced epoxies experience different dominant toughening mechanisms due to characteristics such as different geometry (fiber-like for CNTs as opposed to plate-like for GNPs), aspect ratio, and available surface area to form interfaces with the epoxy matrix. Furthermore, the active mechanisms involved in enhancing initiation fracture toughness are different from those mitigating crack propagation. CNTs and GNPs are much stiffer and stronger than the surrounding epoxy matrix and as a result, the localized stiffness of the region ahead of the crack front is higher. This permits higher amounts of stored strain energy ahead of the crack front allowing the material to carry more load, thus delaying crack initiation, and thereby effectively resulting in an increase in initiation fracture toughness. In addition, the orientation of the nanofillers present in the localized matrix region also affect the local stiffness. CNTs and GNPs that lie parallel with the direction of loading (Mode I opening loads) increase the stiffness in that direction, thus contributing the most to initiation toughness enhancement. Therefore, in a randomly oriented dispersion of nanofillers, a certain percentage of the total individual nanofillers take a favorable orientation and increase the local stiffness in the Mode I loading direction. The increase in local stiffness of the region ahead of the crack front caused by the addition of nanofillers is believed to be the primary mechanism for initiation toughness enhancement. The observed increase in the critical fracture energy of the nanocomposite samples is believed to be caused by the release of the increased strain energy stored in regions ahead of the crack front.

Due to differences in the size of GNPs and CNTs used in this study, it can be shown that at the same weight there are more CNTs than GNPs by about 1 order of magnitude[4]. With more individual CNTs than individual GNPs, there is a greater possibility for favorably aligned CNTs which enhance the stiffness in the Mode I direction. Similarly, GNPs that are favorably aligned with the loading direction can use their 2D plane stiffness to improve stiffness in the Mode 1 direction; however, there are fewer of them, and those that are lying parallel to the loading direction offer little improved stiffness from their through-thickness direction. The differences in the local stiffness resulting from the above mention phenomenon explain the higher initiation toughness values of the CNT-Epoxy samples compared with their counterparts. It must be noted that CNT agglomerations

---

[4] In the present study, the approximate diameter of a GNP is $\sim 5\mu$m, while the CNTs have an average an outer diameter (OD) of $\sim$ 15 nm. Considering that a CNT can be thought of as a GNP rolled in to a tubular structure, a single GNP —assumed to be a 5μm $\times 5\mu$m square plate for this hypothetical thought experiment —can yield about 10 multi-walled CNTs with $\sim 5\mu$m length and $\sim$ 15 nm OD. Therefore, for a CNT-Epoxy sample and a GNP-Epoxy sample at the same nanofiller weight concentration, there are more individual CNTs than individual GNPs dispersed in the epoxy

impregnated with epoxy (observed in SEM images, Figure 2.8(a-iii)) may impart some regions with stiffness enhancement larger than the individual CNTs which may aid initiation toughness enhancement.

Crack bridging and crack deflection are primary mechanisms that dominate the mitigation of crack propagation in CNT and GNP reinforced epoxies, respectively [14, 77]. Crack bridging occurs in the wake of a crack tip and is a result of bridging elements present on the crack path, more specifically, across the separated fracture surfaces that lie in the wake of a crack (see Figure 2.9(a)). The high aspect ratios of CNTs make them suitable for crack bridging. Load transfer occurs from the epoxy to the strong and stiff CNTs via interfaces held by van der Waals forces that exist between the CNTs and epoxy. During crack initiation under Mode I loading, the wake of the crack tends to open but is halted by the CNTs which act as bridging elements [78, 79, 80, 81]. This, in turn, slows crack propagation [81]. In addition to the van der Waals forces between the CNTs and epoxy at the interface, there exists interfacial friction and some degree of mechanical interlocking between the CNTs and epoxy, both of which must be overcome for the CNTs to pull out and the crack to advance. The CNTs used in this study have random chirality, which results in wavy, convoluted profiles along the length of the CNTs (Figure 2.8). Such complex waviness results in features resembling hooks and zigzag lines, which lead to strong mechanical interlocking. Such interlocking, coupled with interfacial friction, is believed to contribute towards increasing the ability of CNTs to bridge cracks [82, 83, 84]. Crack deflection typically occurs in the region ahead of the crack front; but, it still requires the crack to initiate and advance in order to deflect, and hence, is classified as a crack propagation mitigation mechanism. GNPs that lie ahead of a crack front effectively act as a wall because of their 2D planar structure. The localized stiffness of the GNP-Epoxy region ahead of the crack front is high, and thus, the crack path is forced to deviate around those regions (Figure 2.9(b)). This process slows down crack propagation. The presence of pulled-out GNPs has been observed in the SEM images (Figure 2.7(b-iii)) which indicate GNP pullout as an additional possible mechanism for crack propagation mitigation.

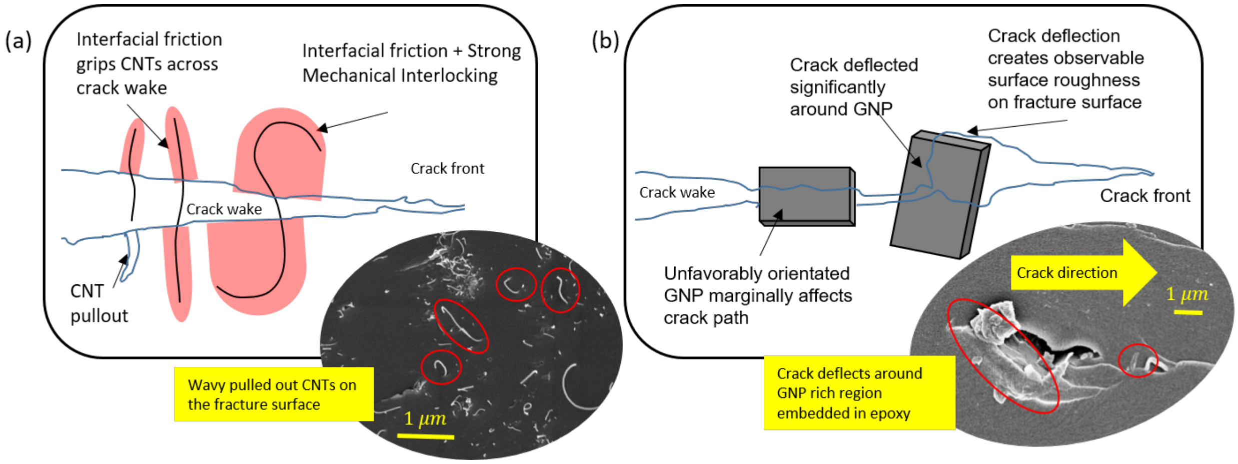

Figure 2.9: Graphical illustrations of (a) CNTs bridging the fractured surface in the wake of a crack and the influence of mechanical interlocking in enhancing the CNTs' bridging capabilities; (b) GNPs deflecting cracks and the effects of GNP orientation on the efficacy of crack deflection. SEM micrographs are included to demonstrate the proposed toughening mechanisms.

The CNT/GNP-Epoxy samples exhibit both toughening mechanisms, i.e., crack bridging and crack deflection. Chatterjee *et. al* explored the synergistic effects of CNTs and GNPs at different CNT/GNP ratios and experimented with different particle sizes [77]. They reported that only the samples reinforced with CNT/GNP mixtures at the 9:1 ratio of CNT:GNP and 0.5% weight concentration exhibited enhancements larger than those of the CNT-Epoxy samples containing 0.5% CNTs by weight; at all other ratios (1:3, 1:5, 1:9, 5:1, and 3:1), the values of K_{IC} are smaller for the CNT/GNP-Epoxy samples. A similar trend is observed in the present study, where the CNT/GNP-Epoxy samples with CNT:GNP at the 1:1 ratio have relatively lower K_{IC} values than the CNT-Epoxy samples. At the 1:1 ratio, the weights of CNTs and GNPs are equal, however, there are more individual CNTs than individual GNPs, as discussed earlier. When 50% of the CNTs in a CNT-reinforced sample are replaced with GNPs, the total number of nanofillers is reduced roughly by 50% as well, resulting in fewer reinforcing agents in the CNT/GNP-Epoxy sample. Since, CNTs and GNPs, as individual nanofillers, have comparable stiffness, a reduction in the total number of stiffening/reinforcing agents in the epoxy can affect the local stiffness of the CNT/GNP-Epoxy regions. Therefore, it is not surprising that a CNT/GNP-Epoxy sample under performs compared with the CNT-Epoxy counterpart. However, the same argument would suggest that a CNT/GNP-Epoxy sample should show a more significant enhancement compared with the GNP-Epoxy counterpart at the same nanofiller weight fraction. This is inconsistent with the experimental results presented here, which show that the CNT/GNP-Epoxy nanocomposites are only slightly outperformed by both CNT-Epoxy and GNP-Epoxy nanocomposites at a given nanofiller weight concentration. This observation suggests that other factors beyond the number of reinforcing elements are at work, such as the agglomeration behavior between CNTs and GNPs. This observation also suggests that 1:1 may not be the optimum ratio for CNT/GNP-Epoxy nanocomposites, although a significant enhancement in fracture toughness and fracture energy is still observed compared with neat epoxy. Further explorations are warranted to better understand the toughening mechanisms behind crack initiation and propagation in CNT and GNP reinforced epoxies and evaluate their effect on overall fracture toughness; and to elucidate the possible synergy between CNTs and GNPs as dual nanofillers.

Chapter 3

Investigating the Fracture Toughness Enhancement in Dual-nanofiller Reinforced Epoxies brought about by the Synergistic Interactions between Embedded CNTs and GNPs

3.1 Introduction

In the previous chapter, we explored the effects of nanofiller reinforcements on crack initiation under mode I loading. It was observed that adding nanofillers in quantities as small as 0.1% weight, a significant enhancement was observed. An interesting case of dual filler systems was also explored. The net enhancement achieved in these dual filler systems was comparable but lesser than that of the individual filler systems. This raised important questions about the interaction between the two nanoparticles. Importantly, we would like to explore different ratios of CNT/GNP to study if they exhibit any synergistic effect on the enhancement of fracture toughness properties of the material. To that end, this chapter explores five different material systems with 0.5% nanofiller weight loading, and three different ratios of

CNT/GNP: namely 1:3 CNT/GNP-Epoxy (CG13-Epoxy), 1:1 CNT/GNP-Epoxy (CG11-Epoxy), and 3:1 CNT/GNP-Epoxy (CG31-Epoxy). Single filler systems were prepared for completeness and neat epoxy samples were fabricated as a baseline for comparison. In this study, two displacement rates were considered at which the mode I fracture toughness tests were conducted: 0.5 mm/min and 2 mm/min. Digital image correlation techniques were utilized to visualize the strain field and identify these mechanisms. To verify the applicability of these mechanisms at faster displacement rates, additional tests were conducted. These tests were used to obtain K_{IC}, G_{IC} and total fracture energy of the samples for all the materials. Additonally, extensive fracture surface analysis was carried out to identify features which indicate crack arresting behavior, as well as markers indicating crack deflection and crack bridging.

3.2 Experimental Setup

Mode-I fracture toughness tests were conducted using crosshead displacement rates of 0.5 mm/min and 2 mm/min. In this study, a different method was utilized for nanoparticle dispersion, while the methods for fabricating (besides dispersion), testing and pre-crack generation were followed as mentioned in the previous chapter's methodology section 2.1. To disperse the nanoparticles, the ultra-sonication method was used. Specifically, an ice-water bath sonication technique was employed. First the required quantities of nanoparticles were measured in a glass beaker. Next, appropriate amounts of acetone was added which serves as a low viscosity solvent to aid dispersion. This mixture was sonicated for 1 hour at 30% amplitude and 20 kHz frequency. Next, measured quantities of epoxy part A (EPON 862) were mixed with the MWCNT-Acetone mixture. This mixture was again sonicated for 1 hour using the same parameters as before. Finally, the dispersed MWCNT-Acetone-Part

A mixture underwent solvent extraction in a rotary evaporator for 1:30 hours. The obtained MWCNT-Part A mixture was then mixed with required quantities of Part B (curing agent) using a magnetic stirrer for 5 minutes. The rest of the processes for degassing and curing remain the same. In conjunction with the Mode I fracture toughness tests, Digital image correlation (DIC) tests were performed to analyze the strain fields. Comprehensive fracture surface analysis was also conducted, for which relevant information will be discussed in the the results section.

3.3 Results and Discussion

Using the same procedure outlined in chapter 2.1, the critical stress intensity factor, K_{IC}; the critical fracture energy, G_{IC} and the total work done, WT were calculated. The raw data was processed according to ASTM D5045 to obtain the aforementioned values. The portion of the load-displacement curve leading up to the peak load was linearized as per ASTM recommendations, and the post crack initiation part of the curve was joined to the peak load point, thus creating a full load-displacement curve showing the crack initiation but also the crack growth.

3.3.1 Critical stress intensity factor, K_{IC}

Figure 3.1 shows the K_{IC} values for all the materials tested in this study. The solid column represent the samples tested at 0.5 mm/min while the hatch filled column represent the data for samples tested at 2 mm/min. Errors bars shown over every column represent one standard deviation from the mean obtained from a minimum of 10 number of samples per material type. Tables 3.1 and 3.2 show the values in a tabular for samples tested at 0.5

mm/min and 2 mm/min respectively.

Table 3.1: Comparison of the critical stress intensity factor (K_{IC}) and fracture energy (G_{IC}) of all the material systems tested at 0.5 mm/min displacement rate

Material Systems	**K_{IC} (MPa· $m^{1/2}$)**	**% Increase**	**G_{IC} (J/m^2)**	**% Increase**
Neat Epoxy	0.62 ± 0.05	-	182 ± 23	-
GNP-Epoxy	0.85 ± 0.13	~ 37	440 ± 106	$\sim$141
CG13-Epoxy	0.84 ± 0.11	~ 35	445 ± 80	$\sim$144
CG11-Epoxy	0.82 ± 0.1	~ 32	360 ± 73	$\sim$97
CG31-Epoxy	0.83 ± 0.12	~ 33	406 ± 90	$\sim$123
CNT-Epoxy	0.75 ± 0.1	~ 20	376 ± 100	$\sim$106

Table 3.2: Comparison of the critical stress intensity factor (K_{IC}) and fracture energy (G_{IC}) of all the material systems at 2 mm/min displacement rate

Material Systems	**K_{IC} (MPa· $m^{1/2}$)**	**% Increase**	**G_{IC} (J/m^2)**	**% Increase**
Neat Epoxy	0.58 ± 0.05	-	233 ± 58	-
GNP-Epoxy	0.79 ± 0.07	~ 36	401 ± 42	$\sim$72
CG13-Epoxy	0.85 ± 0.09	~ 46	384 ± 53	$\sim$64
CG11-Epoxy	0.83 ± 0.07	~ 43	410 ± 61	$\sim$75
CG31-Epoxy	0.79 ± 0.14	~ 36	352 ± 53	$\sim$51
CNT-Epoxy	0.79 ± 0.05	~ 36	400 ± 62	$\sim$71

Figure 3.1 shows that while there is a net effective enhancement in the K_{IC} values for the reinforced epoxies, there is no statistically dominant nanofiller combination that exhibits the highest enhancement. The error bars on the data indicate that all the reinforced epoxy samples lie within the same range of each other in terms of K_{IC} values. No particular synergy has been observed in the dual filler samples. In fact for the samples tested at 0.5 mm/min, the highest enhancement was observed in the GNP-Epoxy samples. In the samples tested at 2 mm/min, the highest enhancement was observed in the CG13-Epoxy samples. However, since the error bars are overlapping all the data, it cannot be stated with confidence, that one material system is better than the other. On an average the reinforced epoxies have K_{IC} values that are about 35% higher than the neat epoxy. This enhancement in initiation fracture toughness can be attributed to several factors. Addition of nanoparticles such as

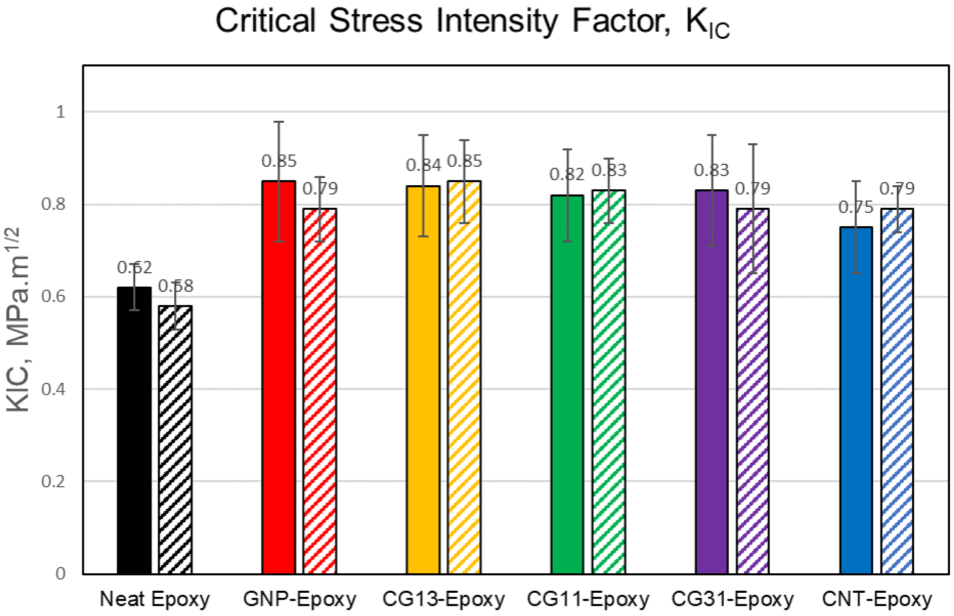

Figure 3.1: Critical stress intensity factor, K_{IC}, for all the materials. The hatched columns indicate a crosshead displacement rate of 2 mm/min while the solid columns indicate a displacement rate of 0.5 mm/min. Errors bars shown over every column represent one standard deviation from the mean obtained from a minimum of 10 number of samples per material type

CNTs and GNPs result in crack bridging and crack deflection in the region around the pre-crack tip, thus requiring a higher amount of energy needed for crack initiation. The changes in stiffness due to nanoparticle addition also affect the size of the fracture process zone, which influences the amount of crack tip blunting ahead of the pre-crack tip. More blunting would result in higher fracture toughness values. These mechanisms have been discussed in earlier chapters in much more detail [29]. Since the nanoparticles used have comparable stiffness values, and were added to the epoxy using the same weight loading and dispersion technique, it is unsurprising that the K_{IC} values of the reinforced nanocomposites are so close to each other.

3.3.2 Critical fracture energy, G_{IC}

The critical fracture energy is described as the minimum energy required for the material in order to initiate crack growth. In other words, it is the maximum energy a material can store as strain energy, before it is energetically favorable for the material to grow two new surfaces (meaning a crack) and releasing some of that strain energy. The fracture process zone, influenced by the local stiffness of the material ahead of the crack tip plays a crucial role in fracture energy enhancements. Addition of nanofillers have an influence on the intrinsic fracture energy, and the fracture process zone as seen by the K_{IC} enhancement, and thus similar enhancements can be expected for fracture energy as well. However, it must be noted that overlapping errors for the critical fracture energy data suggests that while a net effective enhancement was observed, there is statistically no one material that had the best enhancement. Figure 3.2 shows a column chart for the critical fracture energy values for all the materials. The solid column represent the samples tested at 0.5 mm/min while the hatch filled columns represent the data for samples tested at 2 mm/min. Errors bars shown over every column represent one standard deviation from the mean. Tables 3.1 and 3.2 show the G_{IC} values in a tabular for samples tested at 0.5 mm/min and 2 mm/min, respectively.

To study the behavior of the material during the crack growth phase (i.e. crack propagation), a metric: work of fracture, which corresponds to the total area under the force-displacement curve, is introduced. The area under the curve after the crack initiation was used to calculate the additional work done required to grow the crack until complete sample failure. Figure 3.3 shows a column chart for all the total fracture energy values calculated for all the materials. The solid column represents the samples tested at 0.5 mm/min while the hatch filled column represent the data for samples tested at 2 mm/min. The lighter shade stacked column above every column represents the additional work done to cause complete sample failure. Errors bars shown over every column and every stack represent one standard deviation from

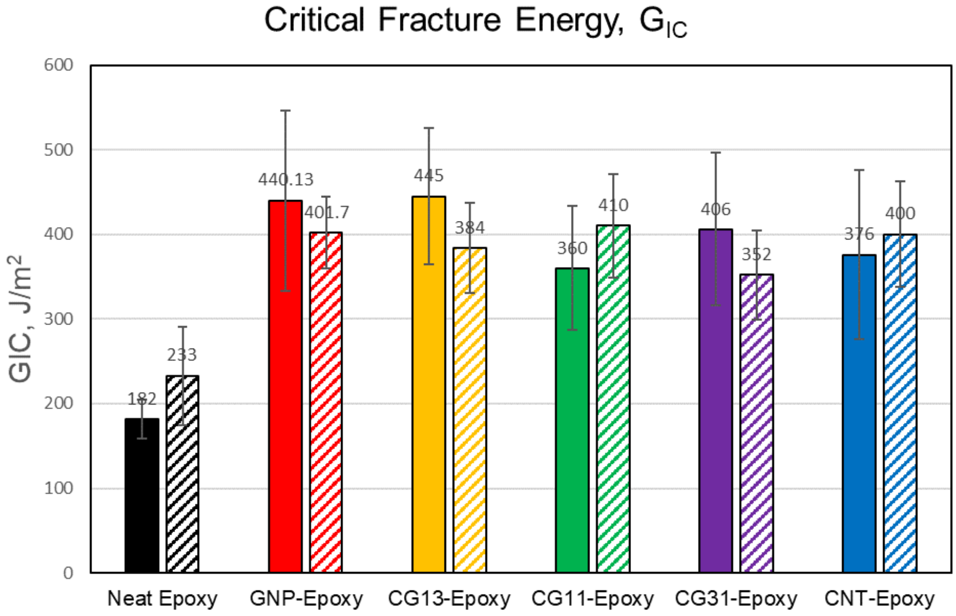

Figure 3.2: Critical fracture energy, G_{IC}, for all the materials. The hatched columns indicate a crosshead displacement rate of 2 mm/min while the solid columns indicate a displacement rate of 0.5 mm/min. Errors bars shown over every column represent one standard deviation from the mean obtained from a minimum of 10 number of samples per material type

the mean calculated for a minimum of 10 samples per material type with a maximum of 12 samples for some material types. Table 3.3 shows the total work of fracture in a table for samples tested at 0.5 mm/min and 2 mm/min respectively. It can be seen that on an average, the graphene reinforced epoxies (single filler and the graphene dominated mixed ratios) have a higher increase in the total energy compared to the CNT reinforced epoxies. This can be attributed to the crack deflection mechanisms that require more work for crack growth, and that are dominant in the sample due to the presence of the GNPs [28]. GNPs that lie ahead of a crack front effectively act as a wall because of their 2D planar structure. GNPs are much stiffer and stronger than the surrounding epoxy matrix and as a result, the localized stiffness of the region ahead of the crack front is high. In order to grow, the crack path is forced to deviate around the locally stiffer and stronger GNP-Epoxy regions (Figure 2.9(b) [28, 85]. This process effectively results in an increase in the total amount of work required for crack growth. The presence of pulled-out GNPs has been observed in the SEM images (Figure 2.7(b-iii)) which indicate GNP pullout as an additional possible mechanism for disrupting crack propagation.

Table 3.3: Comparison of the total work done (W_T) for all the material systems at 0.5 mm/min and 2 mm/min displacement rates. Variation in the data representing one standard deviation from the mean is calculated for a minimum of 10 samples per material type with a maximum of 12 samples for some material types. The work done is calculated as the area under the load-displacement curve.

Material Systems	**W$_T$ (J/m^2) at 0.5**	**% Increase**	**W$_T$ (J/m^2) at 2**	**% Increase**
Neat Epoxy	0.0080 ± 0.0006	-	0.0110 ± 0.0013	-
GNP-Epoxy	0.0209 ± 0.0027	~ 261	0.0254 ± 0.0046	~222
CG13-Epoxy	0.0202 ± 0.0040	~ 252	0.0208 ± 0.0043	~182
CG11-Epoxy	0.0183 ± 0.0027	~ 228	0.0193 ± 0.0083	~175
CG31-Epoxy	0.0157 ± 0.0025	~ 196	0.0201 ± 0.0040	~176
CNT-Epoxy	0.0202 ± 0.0055	~ 252	0.0182 ± 0.0024	~159

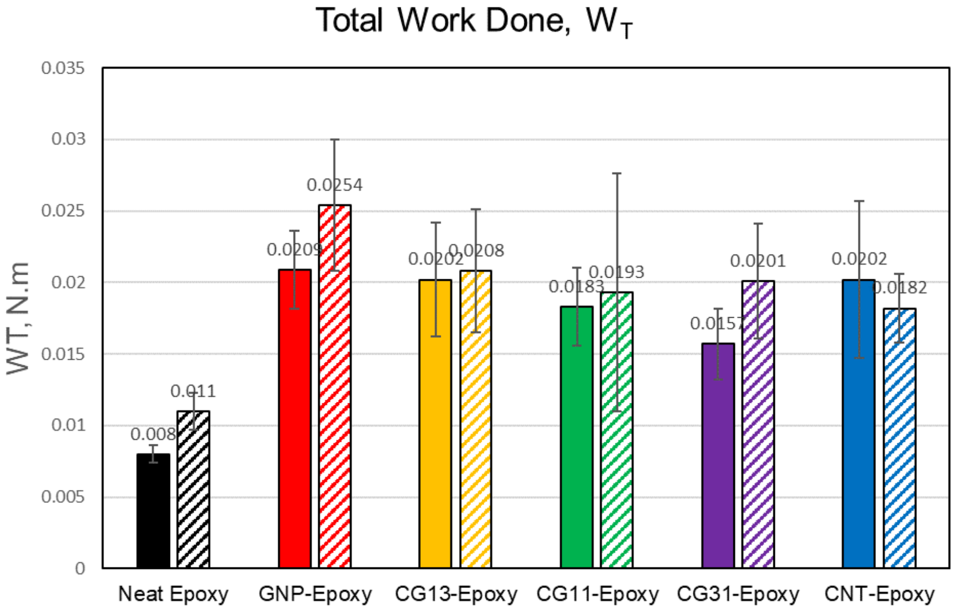

Figure 3.3: Total work done, i.e. the total amount of work required for crack initiation and subsequent crack growth, for all the materials. The solid columns indicate a displacement rate of 0.5 mm/min while the hatched columns indicate a crosshead displacement rate of 2 mm/min. Errors bars representing one standard deviation from the mean are shown over every stack of every column calculated for a minimum of 10 samples per material type with a maximum of 12 samples for some material types

3.3.3 Post-initiation crack growth behavior

In this section, we will look at the effects that the previously described mechanisms have on the post-initiation crack growth behavior. Figure 3.4 shows representative load-displacment curves for a GNP-Epoxy sample exhibiting reloading behavior after crack initiation. It is known that GNPs exhibit crack deflection as the dominant mechanism [28, 75, 76, 86]. A deflection event creates a tortuous crack path (leading to increased surface roughness which can be observed on the crack surface via SEM (Figure 2.7), a result of which is uneven, inclined surfaces relative to the direction of loading [75, 76]. This can lead to mixed-mode loading conditions locally, and may result in additional load carrying capacity in the sample, leading to a reloading behavior observed in the load-displacement curves. Another major source of mixed-mode loading conditions occur at the macroscale due to experimental uncertainty: misalignment of the test fixture resulting in a tilt (deviation of sample planar axis from the plane of loading) in the loaded sample due to system compliance while testing and geometric variations in the sample fabrication. This presence of macroscale tilt was verified using DIC measurements of out of plane displacements during testing (the absolute out of plane displacements measured via DIC were between 0-1 mm). Since crack deflection does not occur in CNT dominated samples, the contribution of mode mixity in those samples emanating from crack deflection is absent, however, the experimental uncertainty still contributes. Figure 3.4 also shows a fractograph of a sample clearly exhibiting rib marks, a physical artifact of crack arresting behavior [87]. These number of rib marks on the sample directly correlate with the number of reloading event observed in the samples.

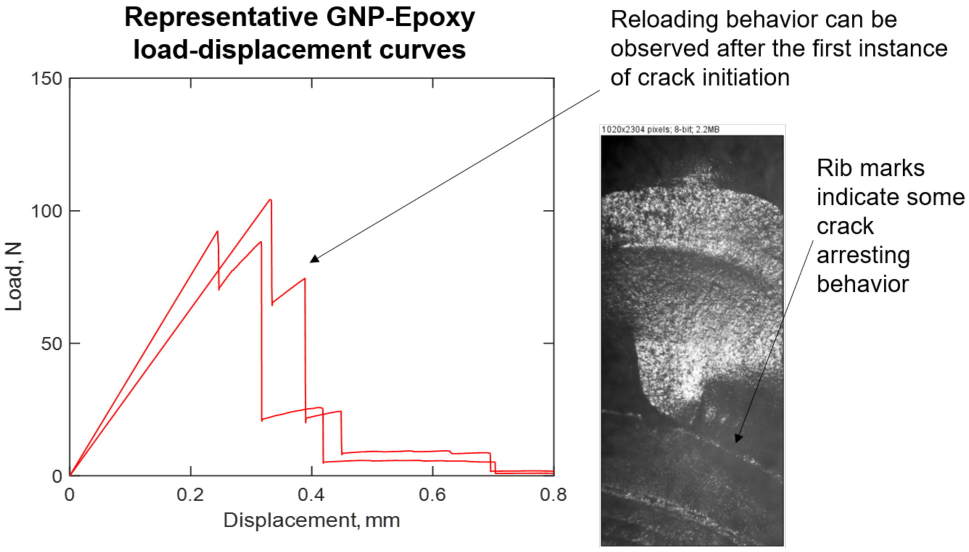

Reloading behavior can be observed after the first instance of crack initiation

Rib marks indicate some crack arresting behavior

Figure 3.4: Left: representative load-displacement curves (for 0.5 mm/min crosshead displacement) showing the initial linear portion followed by the reloading behavior observed in all the samples after crack initiation. Right: Image of a fracture surface showing indicators of crack arresting behavior as seen during the reloading event in the load-displacement curves. Four rib marks ahead of the pre-crack can be seen corresponding to the four instances of load drops.

Digital Image Correlation (DIC) results

Another method of verifying reloading behavior in samples is via DIC testing. DIC allows visualization of the displacement field on sample. Through this, the strain field can be plotted and the elastic zone ahead of a crack tip can be visualized. Figure 3.5 shows two images from a DIC test indicating the strain field present on the surface of a GNP-Epoxy sample before crack growth, and reloading behavior during crack growth, respectively. The strain concentration contours can be observed before crack growth occurs indicated by a red region (∼0.001 strain, ε_{yy}) near the crack tip. Just after crack initiates, the crack grows and arrests for 6 seconds during which strain builds up in the sample. This can be seen via the strain concentration contours (∼0.004 strain, ε_{yy}) ahead of the grown crack. The observations of the changing strain contours corresponding to the reloading events observed

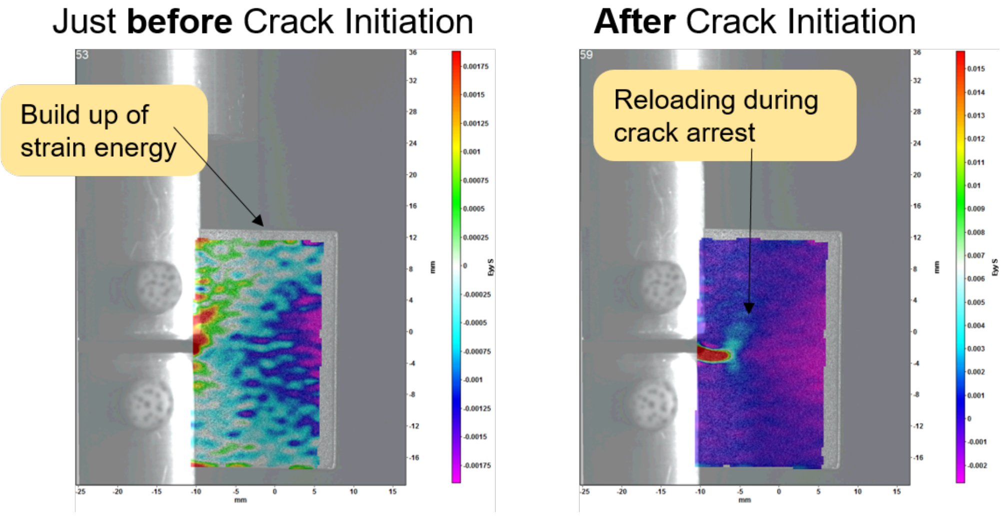

Figure 3.5: Left: The ε_{yy} strain field on the surface of a GNP-Epoxy sample just before crack initiation. Right: the ε_{yy} strain field on the sample sample just after crack initiation. The DIC image shown captures a small instant in time when reloading occurs. Changing strain contours can be seen on the fracture surface indicating build up of strain during reloading.

in the load-displacement curve definitively prove the occurrence of reloading in the sample during crack growth.

Chapter 4

Influence of pre-crack characteristics such as length, crack front shape, and crack plane profile on the mode I fracture toughness of structural epoxies

4.1 Introduction, Background, and Motivation

The fracture toughness of materials is a fundamental material property often used widely in engineering design [1, 3]. It indicates the critical value of strain energy a material can absorb in the presence of flaw such as a crack before the strain energy is released in the form of crack growth. The higher the fracture toughness, the better the material's ability to resist crack growth, or crack propagation [1, 3, 88]. For polymers, the compact tension (CT) sample geometry and the single edge notch bend (SENB) sample geometry are the two commonly used sample geometries for Mode-I fracture toughness testing, as they have been standardized through the ASTM D5045. This standard which is designed upon the concepts of LEFM theory, lays down the guidelines for valid fracture toughness testing, such that they do not violate the limitations and assumptions of the LEFM theory.

A key requirement of the ASTM D5045 standard and the LEFM theory for valid fracture toughness characterization states that a sharp, natural crack[1] must be present before the load is applied to the sample [5]. Typically, this is introduced through a process called razor blade tapping, wherein a sharp, fresh blade is tapped into a notch using a hammer [5]. This process results in an acceptable representation of a theoretical crack (where the tip radius is zero) [28]. However, the process of razor blade tapping is very susceptible to user error, and oftentimes unstable crack growth can occur during the pre-cracking process which results in the loss of a sample even before testing, a highly undesirable situation [89]. To that effect, several other methods of creating a sharp pre-crack in brittle polymer materials exist such as sawing, sliding a razor blade, razor blade pressing, fatigue cycle cracking [90, 91]. *De Souza et al* explored the effects of different pre-crack generation methods on the calculated Mode-I fracture toughness values for Poly-Methyl Methacrylate (PMMA) resin [90]. Four methods, namely razor blade tapping, razor blade pressing, rotary blade machining, and sawing were explored. Through topographical analysis of the fracture surfaces, it was found that the different pre-cracking methods resulted in different surface features such as hackles observed on the razor tapped samples, and concentric rib marks observed on the razor pressed samples [90]. Additionally, the different methods also resulted in different fracture toughness values for comparable samples, with the lowest K_{IC} values of $\sim 1.15 \pm 0.11$ MPa.m$^{1/2}$ obtained through razor blade tapping, and the highest K_{IC} values of $\sim 1.77 \pm 0.17$ MPa.m$^{1/2}$ obtained via razor blade pressing [90]. It is important to note the increased K_{IC} variation in the data between the two processes as well. The different pre-cracking methods have different effects on the stress state ahead of the crack tip which directly affects the fracture toughness of the PMMA samples (visualized using the photo-elasticity technique)

---

[1] Since this crack is introduced in the sample before testing, it is called a pre-crack.

[90]. In the case of razor blade pressing, the residual stresses (crack tip plastic deformation) induced during pressing seem to increase the K_{IC} values drastically [90]. Similar results have been found in several other studies, where razor blade pressing results in artificially high K_{IC} values, and hence this process is not recommended by the ASTM D5045 standard as well [5, 92, 93, 94]. Additionally, the most conservative fracture toughness values were always obtained via natural cracks produced by razor blade tapping [90].

Since it has been established that a sharp natural crack results in accurate fracture toughness characterization, several efforts have been made towards generating sharp, natural cracks in a sample in a reproducible manner that is free of operator error/bias. Methods such as fatigue cracking have been explored, however, they do not work very well with brittle polymer materials which exhibit unstable crack growth [91, 94]. Newer approaches, such as the one demonstrated by *Kuppusamy et al.* [95] rely on designing pre-cracking rigs which utilize a guillotine-type razor blade tapping setup. This eliminates the operator error component; however, the actual process of razor blade tapping is still difficult to reproduce. *Kuppusamy et al.* also demonstrates the use of tension loads to create a natural pre-crack, which is arrested using localized compression in the through-thickness direction [95]. Good reproducibility was observed for pre-crack generation in terms of pre-crack lengths and shape. A combination of guillotine-style razor tapping rig and slight through thickness compression applied via vice clamps was used in the present study to generate pre-cracks. This method was found to be easier to implement as it did not require the use of a universal testing machine, and a portable, compact test rig could be designed where the compression was applied using vice grips and the razor blade tapping was performed using a tapping hammer dropped from a fixed height through a guided rail.

Although several works have explored the effects of different pre-cracking methods on the K_{IC}

values of the materials, there is very little information on the effects of the influence of pre-crack characteristics such as length, crack front shape, and crack plane profile on the Mode-I fracture toughness. This chapter of the dissertation focuses on comprehensively exploring the influence of these pre-crack characteristics on the Mode-I fracture toughness of brittle polymers such as epoxies. Approaches to quantify crack front shapes have been introduced, and subsequently, their influence on the K_{IC} values have been studied. Additionally, a thorough topographical analysis of the fracture surface is presented, through which the influence of the crack plane profile over the post-initiation crack behavior can be understood. As seen in the literature, the process through which a pre-crack is generated can result in different kinds of pre-cracks with different topographies and geometries, and that can severely affect the obtained K_{IC} values [90, 92, 93, 94, 95]. This chapter of the dissertation aims to provide more insight into the factors that affect the obtained K_{IC} values during Mode-I fracture toughness testing, particularly focusing on the quantifiable characteristics of the pre-crack itself.

4.2 Experimental Methodology and Setup

4.2.1 Materials and Fabrication

In this study, EPON 862 (Diglycidyl Ether of Bisphenol F) epoxy was used as the resin while EPIKURE W (Aromatic Amine curing agent) was used as the curing agent. Both materials were supplied by Hexion Inc. The resin and the curing agent were mixed with a ratio of 100:26.4 by weight, as prescribed by the manufacturer. The resin and curing agent mixture was degassed at 90 kPa vacuum pressure for 30 minutes [85, 96, 97, 98, 99]. During degassing the mixture was heated to, and maintained at, 70°C in order to aid degassing by reducing the viscosity [85, 96]. The degassed mixture was then poured into hot silicone molds maintained at 70°C as well. The mixture, now cast in the molds, was degassed for a second time under 90 kPa vacuum pressure for 20 minutes to remove any additional entrapped air. The molds were maintained at 70°C during the second degassing stage as well. Finally, the epoxy mixture was cured using the following curing cycle, based on previous works [85, 96]: 80°C to 121°C in 30 minutes, hold at 121°C for 2 hours, 121°C to 176°C in 30 minutes, and hold at 176°C for 2 hours in an oven. The samples were allowed to cool down to room temperature before they were extracted from the molds.

4.2.2 Sample Preparation and Pre-crack Generation

The compact tension (CT) sample geometry, as defined in ASTM D5045, was used in this study for mode I fracture toughness tests. The samples had an approximate dimension of 32 × 30 × 6.25 mm (designed with a width of $W = 25$ mm)[2]. Figure 4.1a shows an example photo of a neat epoxy sample used in this study. Due to the casting method of sample fabrication, there were meniscus formations near the edges of the samples, which were sanded down until uniform thickness was achieved on the sample face (Figure 4.1a). To facilitate the generation of a pre-crack, first, a sharper notch was introduced on the existing notch tip by sawing. Then, a fresh razor blade was tapped once using a custom-built razor tapping setup[3] resulting in a sharp, natural pre-crack as required by ASTM 5045. Figure 4.1b shows an example of a neat epoxy sample that has been pre-cracked.

---

[2] The width W is defined in the ASTM D5045 standard as the distance between the center-line of the pin-holes and the sample edge opposite to the machined notch.

[3] This setup utilized a guillotine-styled razor which was tapped using a tapping hammer (~200 g) dropped from a fixed height (40 mm). Additionally, the samples were gripped in mini-vice faces at a specific distance from the notch tip, which applied through-thickness compression causing the crack to arrest, and thus allowing some control over the pre-crack length [95]

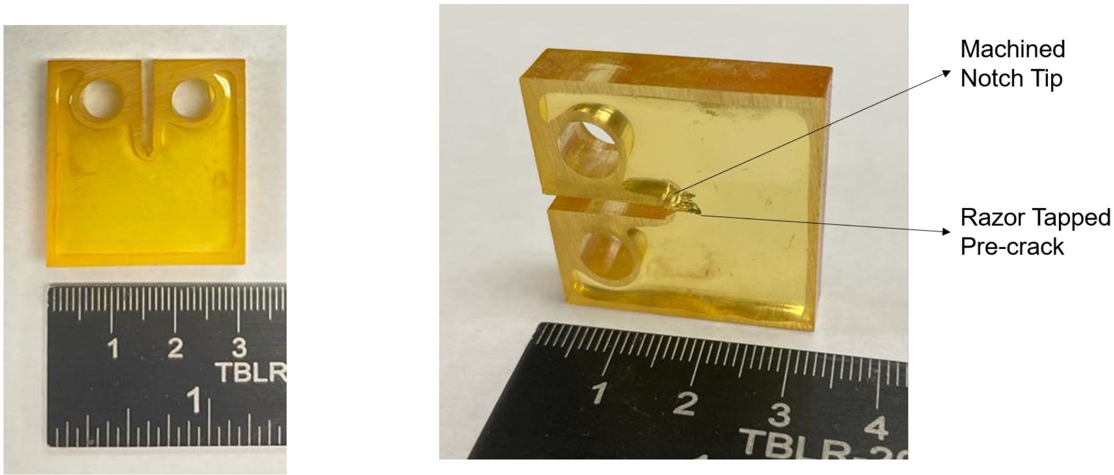

(a) A photograph of an actual neat epoxy sample used in this study.

(b) A photograph of an neat epoxy sample that has been pre-cracked. The pre-crack can be seen ahead of the notch tip.

Figure 4.1: Photographs of the fabricated samples used in this study.

4.2.3 Mode I Fracture Toughness Testing

Compact Tension tests were conducted in a Universal Testing Machine (Instron 5900 Series Double Column) with a crosshead displacement of 0.5 mm/min. Load and displacement values were recorded for each sample. The procedures outlined in ASTM D5045 for data processing, and calculation of mode I critical stress intensity factor (K_{IC}) were used. A total of 50 epoxy samples were tested until complete failure, and the effects of various pre-crack characteristics on the peak load carrying capacity, fracture displacement, and K_{IC} were studied.

4.2.4 Pre-crack Characterization and Measurement Techniques

The pre-crack characteristics were classified as follows: length, the shape of the crack front, crack plane profile. Figure 4.2 demonstrates a simplified 3D schematic of the pre-crack and highlights the pre-crack characteristics considered in this study. The pre-crack length was

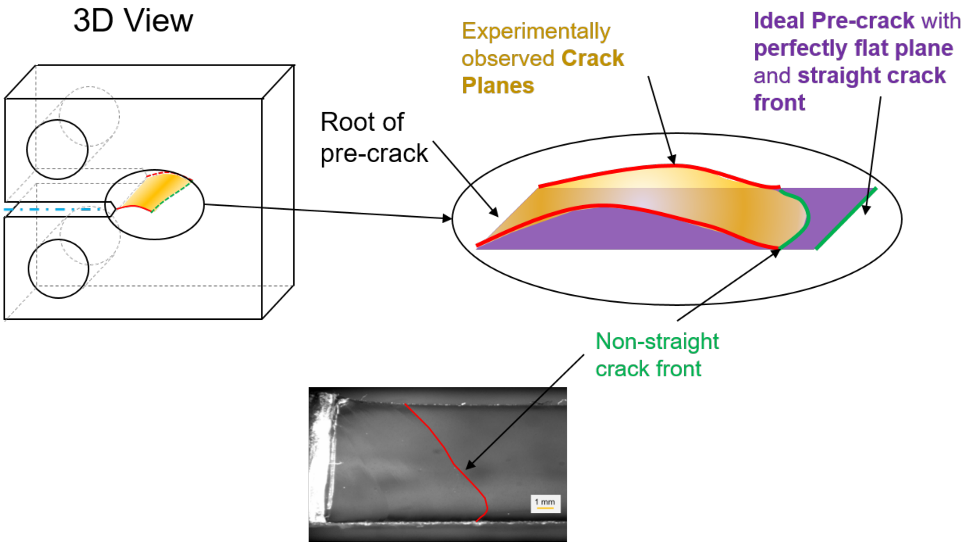

Figure 4.2: A 3D schematic of a compact tension sample highlighting the pre-crack region, and illustrating the pre-crack characteristics. The features shown in this graphic illustration are exaggerated for better visual explanation of the pre-crack characteristics

measured by analyzing the fracture surface of every sample after testing, as recommended by ASTM D5045. The fracture surface was imaged with a calibrated digital microscope (Hirox Digital Microscope) and the average pre-crack length across the sample thickness was measured on the image using a calibrated point-to-point measurement tool available in the imaging software (INFINITY ANALYZE). In this study, the crack front shape refers to the shape of the foremost edge of the pre-crack plane. Fracture surface images were used to trace the shape of the crack front for all the samples. The trace was obtained by marking several points on the crack front and then fitting a cubic curve through them. A two-parameter quantification was developed to characterize the crack front shape using inclination, ϕ, and arc-chord ratio tortuosity, τ. In this study, the inclination is defined as the inclination of the best-fit linear line passing through the traced crack front shape. The arc-chord ratio, a simple yet effective tool to quantify the tortuous path a line takes between its endpoints, was selected to quantify the tortuosity of the crack front shape. The ratio of the length of the traced arc, L to the chord length between the end-points, C is defined as the arc-chord ratio. For a perfectly straight line the arc-chord tortuosity ratio is 1, while for a non-straight curve, the arc-chord ratio is greater than 1. Figure 4.3 illustrates the process followed to calculate the inclination and tortuosity for every sample. In addition to these quantifiable characteristics, a comprehensive fractographical analysis was conducted to qualitatively identify surface features that may lead to a better understanding of post-initiation crack behavior in epoxy polymers. In this study, the crack plane profile refers to the x-y-z profile of the pre-crack plane. This analysis was carried out using fracture surface images obtained via digital microscopy.

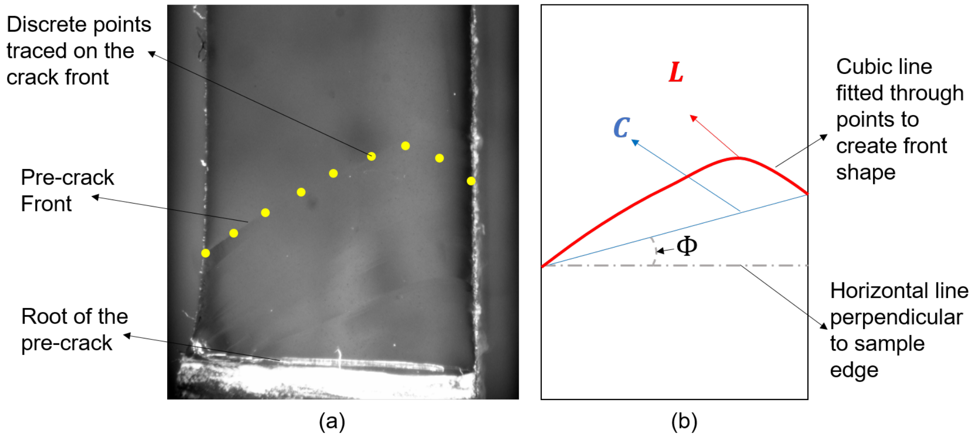

Figure 4.3: (a) A digital microscope image of the fracture surface of a neat epoxy CT sample. Yellow dots identify the crack front and mark the points used to curve-fit, and subsequently recreate the crack front shape. (b) An illustration of the obtained crack front shape is quantified using inclination, ϕ and arc-chord tortuosity, τ.

4.3 Results and Discussion

Load and displacement curves were obtained for each sample and the K_{IC} values were calculated according to the procedure outlined in ASTM D5045[4]. The obtained K_{IC} values

---

[4] The procedure mentioned in ASTM D5045 requires the linearization of the initial portion of the load-displacement curve to discount the effects of sample compression due to pins, and system compliance. The

have been plotted as a function of the selected characteristics to identify any present trends or correlations. The following formula for the critical stress intensity factor has been used for calculation of K_{IC} values:

$$K_{IC} = \frac{P}{B \cdot W^{1/2}} f(x) \tag{4.1}$$

where B is the thickness, W is the width as defined by ASTM and f(x) is the calibration factor which is a function of initial crack length, a and width.

4.3.1 Variation of K_{IC} as a function of Pre-crack Length and Crack Thickness

Figure 4.4a shows the influence of pre-crack length on the peak load carrying capacity of the samples. The plot shows a linearly decreasing peak load value with an increasing pre-crack length. The highest peak load of 102 N was obtained at a pre-crack length of 0.254 mm, while the lowest peak load value of 15.8 N was obtained at a pre-crack length of 5.94 mm. The cross-section area of the ligament that holds the two halves of the compact tension sample decreases with increasing pre-crack length. Additionally, the moment arm measured from the loading pins to the crack tip also increases as the crack propagates, and hence the sample's ability to carry more load is diminished.

Since the K_{IC} value is dependent on the peak load value (Equation 4.1), a strong correlation between the peak load and pre-crack length could influence the K_{IC} value significantly. To mitigate this influence, the calibration factor f(x) mentioned in ASTM standard (and in Equation 4.1), is factored in to the calculations for K_{IC}. The factor f(x) is a semi-empirical factor that takes into account the increase in sample compliance as a result of increasing

---

linearized curve is then used to identify peak load and fracture displacement, which are then subsequently used to calculate K_{IC}

pre-crack length [100]. The calibration factor is calculated for each sample using the initial crack length (which includes the notch and the pre-crack) and sample width using Equation 4.2 [5].

$$f(x) = \frac{(2+x)(0.886 + 4.64x - 13.32x^2 + 14.72x^3 - 5.6x^4)}{(1-x)^{3/2}} \tag{4.2}$$

where x = a/W. Figure 4.4b shows the variation of the critical stress intensity factor, K_{IC}, as a function of the pre-crack length. The highest K_{IC} value of 0.70 MPa.m$^{1/2}$ was obtained at a pre-crack length of 0.254 mm, while the lowest K_{IC} value of 0.22 MPa.m$^{1/2}$ was obtained at a pre-crack length of 5.94 mm.

While a clear decreasing linear trend can be seen in the peak load between 0 to 3.5 mm pre-crack lengths, that effect is mitigated by the use of the calibration factor, and the K_{IC} values in that range of pre-crack lengths are adjusted such that an initial plateau region is formed. It can be observed that the amount of variation in the data increases beyond the 3.5 mm threshold length, and the K_{IC} values tend to decrease significantly thereafter. This observed trend in the variation of K_{IC} with pre-crack length was best described using a fourth order polynomial fit with a fairly flat region until 3 mm followed by a downward dip indicating decreasing K_{IC} values. While the current ASTM standard prescribes a minimum pre-crack length, the current data suggests that a maximum permissible pre-crack length, proportionate to the sample geometry dimensions, should also be prescribed for reproducible determination of Mode-I fracture toughness, K_{IC}, of a material.

Figure 4.5 shows the influence of pre-crack lengths on the critical fracture displacement[5] at crack initiation. The average fracture displacement of the entire data set is 0.24±0.1 mm. Based on the graph shown in Figure 4.5, it can be observed that the pre-crack length

---

[5] In this paper, critical fracture displacement refers to the critical crosshead displacement at which crack growth initiates.

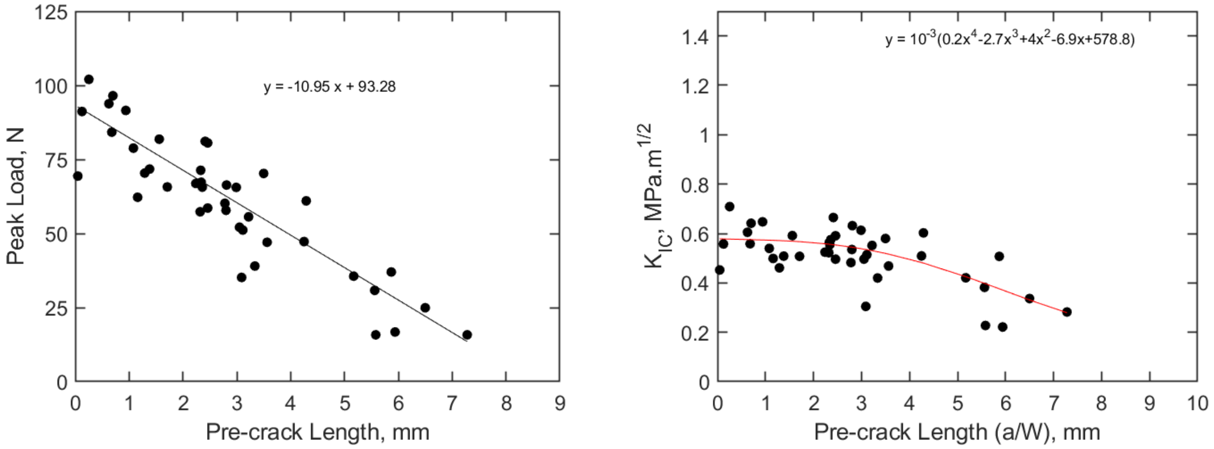

(a) Variation of the peak load exhibited by each sample as a function of pre-crack length.

(b) Variation of critical stress intensity factor, K_{IC} as a function of pre-crack length.

Figure 4.4: Effects of pre-crack length on peak load carrying capacity and fracture toughness.

does not strongly influence the fracture displacement. The data is more dispersed at higher pre-crack lengths, but almost all the values lie within one standard deviation. The absence of a strong correlation can be attributed to the fracture energy of the material, which is an intrinsic material property that remains unaffected by geometry.

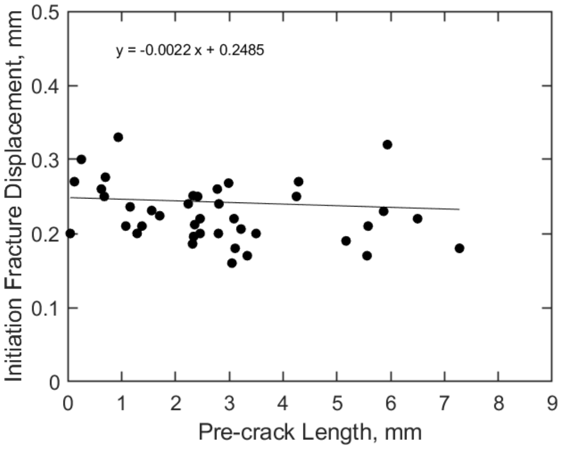

Figure 4.5: Variation of critical fracture displacement at crack initiation versus pre-crack length.

The effect of crack plane thickness[6] on the Mode-I fracture toughness property of materials has been widely studied in the literature [101, 102, 103]. Larger K_{IC} values are observed at smaller sample thicknesses. K_{IC} values tend to decrease with increasing thickness until they reach minimum K_{IC} value plateau[101, 102, 103]. This trend is attributed to the transition of plane stress state (at smaller thicknesses) to plane strain state (at larger thicknesses) ahead of the crack tip. In the case of a thinner sample, the plane stress (biaxial stress state) that exists on the external surface of the sample provides less constraint on the material through-thickness, thus allowing the formation of a significant plastic zone ahead of the crack tip [101, 102, 103]. For crack initiation, more energy is subsequently required to overcome the larger plastic zone which causes increased crack tip blunting, thereby leading to higher K_{IC} values [103, 104]. However, in the case of plane strain (triaxial stress state), the constraint on the material through-thickness is larger and that reduces the size of the crack-tip plastic zone. Subsequently, the amount of energy required for crack growth is lesser, leading to lower K_{IC} values [101, 103, 104]. The difference between plane stress fracture toughness and plane strain fracture toughness can be quite significant, with the former being several times larger than the latter [101, 102, 103]. For engineering design purposes, plane strain fracture toughness is most commonly used as it is more conservative [101, 102, 103]. Figure 4.6a shows the variation of K_{IC} with crack plane thickness. Since studying the effects of crack plane thickness on the fracture toughness was not an objective of this study, the samples were not fabricated with varying thicknesses, but were fabricated with a nominal thickness of 6.35 mm. A small degree of cure shrinkage has resulted in the average thickness shifting to 5.97 mm. No correlation can be observed between K_{IC} values and the crack plane thicknesses as the range of thicknesses explored in this study are very limited. Figure 4.6b shows the variation of K_{IC} as a function of pre-crack length and crack plane thickness. Similar to

---

[6] For a sample exhibiting a flat crack plane, the crack plane thickness is equivalent to the sample thickness. In this study, the crack plane thickness is approximated to be equal to the sample thickness.

Figure 4.6a, no significant correlation can be observed between the K_{IC} values and the crack plane thickness.

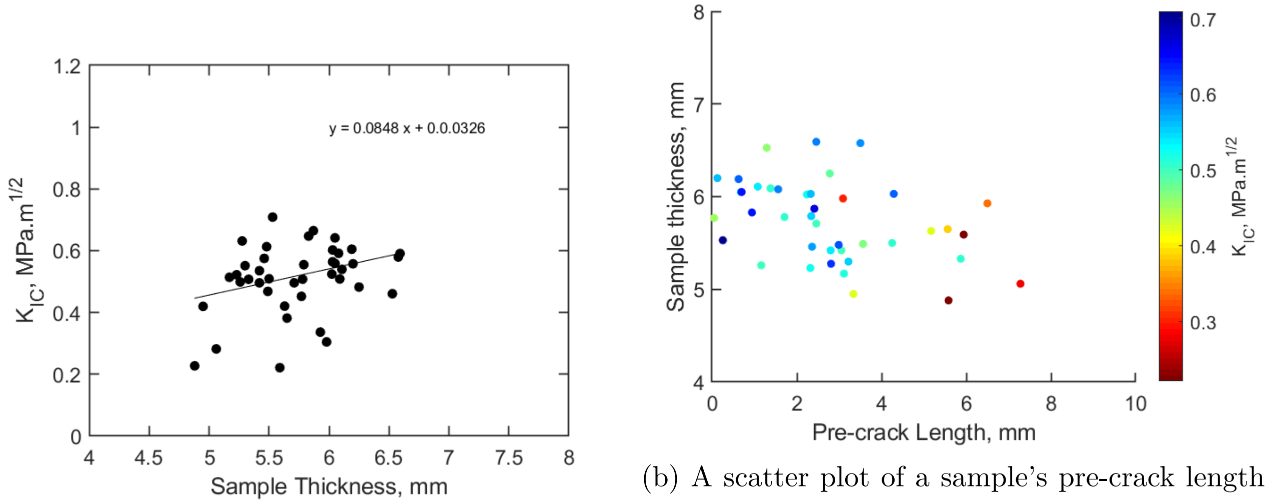

(a) Variation of critical stress intensity factor, K_{IC} as a function of crack plane thickness

(b) A scatter plot of a sample's pre-crack length plotted against it's corresponding thickness. The gray scale shade of the points indicates the K_{IC} values of the samples with the gray scale color-bar indicating the range of the K_{IC} values.

Figure 4.6: Effects of crack plane thickness on the critical stress intensity factor, K_{IC}

4.3.2 Effects of Crack Front Shapes on Mode-I Fracture Toughness

Crack front shapes were characterized by the two-parameter quantification using inclination, ϕ (in degrees), and arc-chord tortuosity, τ. Using the procedure described in previous sections, the crack fronts for all the samples were traced. Figure 4.7 shows some representative examples of the traced crack fronts (Additional images showing the traced pre-crack fronts obtained for all the samples are presented in the Appendix F). These curves have been shifted in the X and Y directions such that they are approximately centered around the origin. Several types of shapes were observed through these traced pre-cracks; commonly, wavy and sloping shapes were encountered the most, with a few samples having straight crack fronts as well. No particular control was exercised to create any specific crack front shapes, and thus the obtained crack fronts statistically represent the effect of the pre-cracking process used in this study on the crack front shape.

Figure 4.8a shows the variation of K_{IC} values as a function of the inclination of the crack front shape[7]. It can be observed that at lower inclinations the variation in the K_{IC} values is smaller compared to the variation at higher inclinations. While there are no specific guidelines for acceptable crack front inclinations mentioned in the ASTM D5045-99 standard [5], it does mention that the difference between the shortest and longest pre-crack length measurement (measured from the root of the pre-crack) must not exceed 10%. The green dots shown in Figure 4.8a show samples that satisfy this ASTM guideline. This method effectively allows for any type of crack front shapes, without considering the crack front shape's tortuosity, as long as the 10% variation between the smallest and largest pre-crack lengths is maintained. It can be observed from Figure 4.8a that several samples exhibited comparable K_{IC} values, despite having larger than 10% variations in the smallest and largest pre-crack length measurement. Additionally, the green dots also have similar variation compared to the other samples below 10 degrees of inclination that did not fit the ASTM criterion, indicating that there are other additional factors contributing to the variation in K_{IC} values.

Along with inclination, the degree of waviness of the crack front shape indicated by the arc-chord tortuosity is introduced as a separate characteristic of the crack front shape. Figure 4.8b shows the variation of K_{IC} values as a function of the arc-chord tortuosity, τ. At lower tortuosity, the obtained K_{IC} values are more consistent. As the tortuosity increases beyond 1.05, the variation in the K_{IC} values is significantly larger. The green dots seen in Figure 4.8b are the same samples highlighted in Figure 4.8a, i.e. the samples with lesser than 10% difference between the smallest and largest pre-crack length. Most of

---

[7] The inclination values indicate the inclination of the best-fit linear line—obtained via linear regression of the traced crack front—relative to the through-thickness direction.

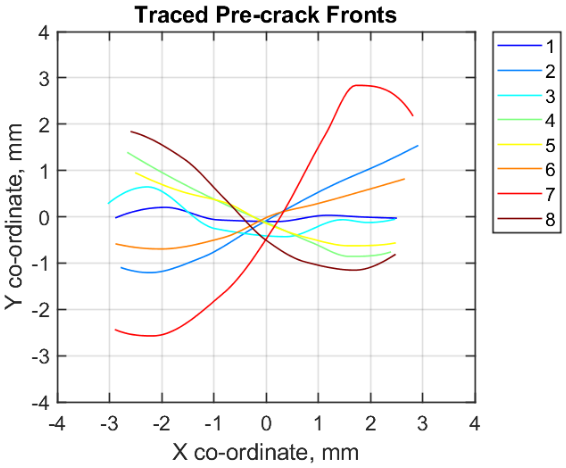

Figure 4.7: Traced pre-crack fronts for eight randomly selected samples plotted on an X-Y co-ordinate system. The curves have been shifted such that they are roughly centered around the origin, in order to allow visual comparison. The legend on the right indicates the sample number.

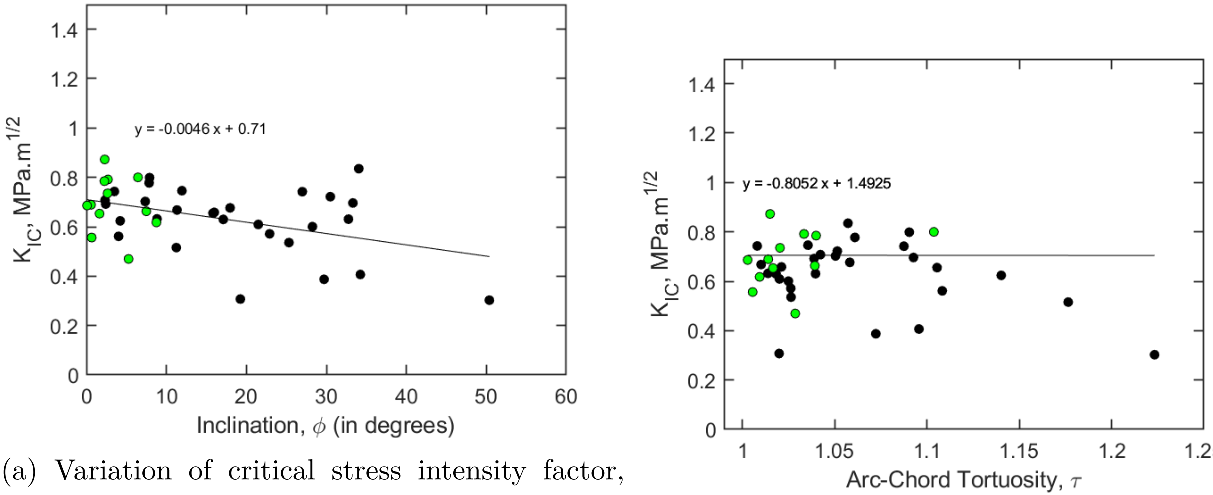

(a) Variation of critical stress intensity factor, K_{IC} as a function of crack front inclination, ϕ. Green dots represent K_{IC} values of samples which had inclination variations within the bounds prescribed by ASTM D5045.

(b) Variation of critical stress intensity factor, K_{IC} as a function of crack front tortuosity, τ.

Figure 4.8: Variation of K_{IC} as a function of the pre-crack front shape parameters

these samples lie under the 1.05 tortuosity level. To better visualize the combined effect of the inclination and tortuosity, Figure 4.9a and 4.9b present the K_{IC} values plotted against the two crack front shape parameters. Similar to Figure 4.8a, green dots highlight the samples fulfilling the ASTM guideline for crack shapes. Samples with high inclinations and high tortuosities have lower K_{IC} values. Samples having lesser than 10 degrees of inclination seem to have comparable K_{IC} values with respect to the manufacturer's reported values of ∼0.74 MPa.m$^{1/2}$, even at tortuosities as high as 1.10. From Figure 4.9a and 4.9b, it can be observed that for reproducible and repeatable determination of K_{IC}, samples with crack front shapes having less than 10 degrees of inclination and less than 1.05 arc-chord tortuosity should be considered. The green dots highlight the same limits, thus supporting the observations; however, there are more data points in the area with K_{IC} values comparable to the manufacturer's reported values. By quantifying the crack front shape using the mentioned two parameters, a more comprehensive criterion can be developed for the selection of valid sample data, thus allowing for larger data sets to be considered and therefore enabling uniform representation of the variation in fracture toughness tests.

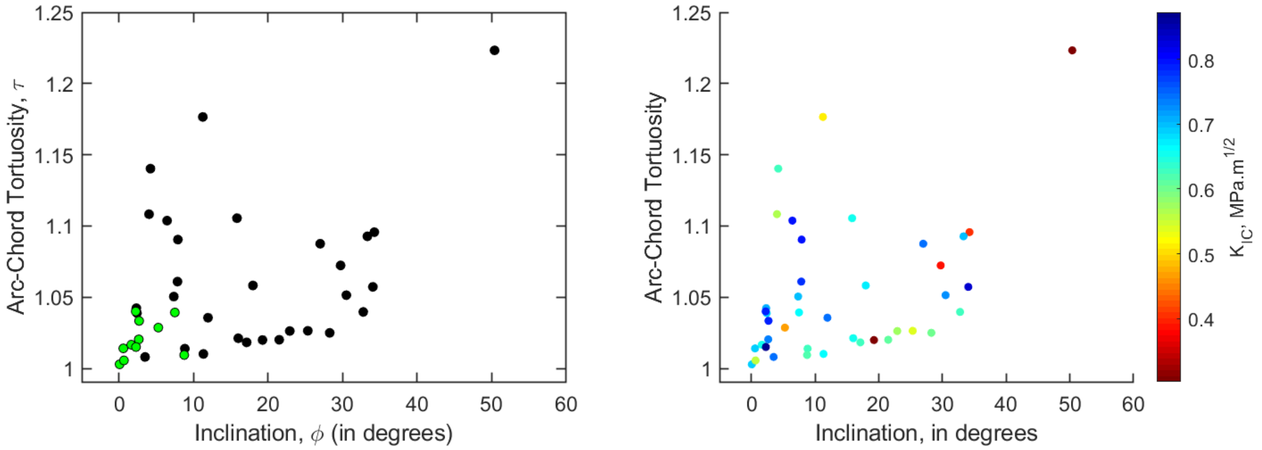

(a) Correlation between tortuosity and inclination values for each crack front. Green dots represent K_{IC} values of samples which had inclination variations within the bounds prescribed by ASTM D5045.

(b) A scatter plot of the measured crack front inclination plotted against it's corresponding tortuosity. The shaded points indicate the K_{IC} values of the samples with the scale color-bar indicating the range of the K_{IC} values.

Figure 4.9: Effects of crack front shape parameters on the critical stress intensity factor, K_{IC}

4.3.3 Influence of Crack Plane Profile on Crack Initiation and Crack Growth Behavior

Figure 4.10 shows the representative load-displacement curves obtained for all the samples considered in this study. The load-displacement curves show the initial non-linear portion of the curve which is attributed to system compliance, and sample compression at the pin-holes [5, 85]. This portion of the curve has to be linearized according to the process outlined in the ASTM D5045-99 standard [5]. Fairly linear behavior is then observed until the first instance of load drop, corresponding to the initial crack extension[8] in the sample. The subsequent crack growth behavior of the samples was also monitored in this study. Interestingly, two distinct crack growth behaviors were observed: First, where the samples exhibited a sharp drop in the load, followed by a smooth and gradual reduction to zero load i.e. brittle response; and second, where the samples exhibited a load drop followed by several instances of reloading and subsequent drops before finally reaching zero load. Topographical analysis of the fracture surface revealed that all the samples exhibiting the former behavior, i.e. sharp decline of load after crack initiation, had a smooth fracture surface, as shown in Figure 4.11(Left). On the contrary, samples exhibiting the latter behavior, i.e. reloading of load after crack initiation, had millimeter-sized rough features as shown in Figure 4.11(Right). Consequently, the two behaviors were termed as ”smooth-drop” and ”rough-reload”, respectively, for simplicity of referencing in this work.

In the case of the smooth-drop behavior, the seemingly featureless surface of the pre-crack and the subsequent crack propagation region is an indicator of fracture due to pure Mode-I loading condition [105]. After crack initiation, the crack extension occurs in a smooth fashion as the pre-crack front advances and such smooth crack propagation requires minimum fracture energy for the creation of two new surfaces [88, 105]. In the case of the rough-reload

---

[8] In this chapter, the ”initial crack extension” is referred as ”crack initiation” for brevity.

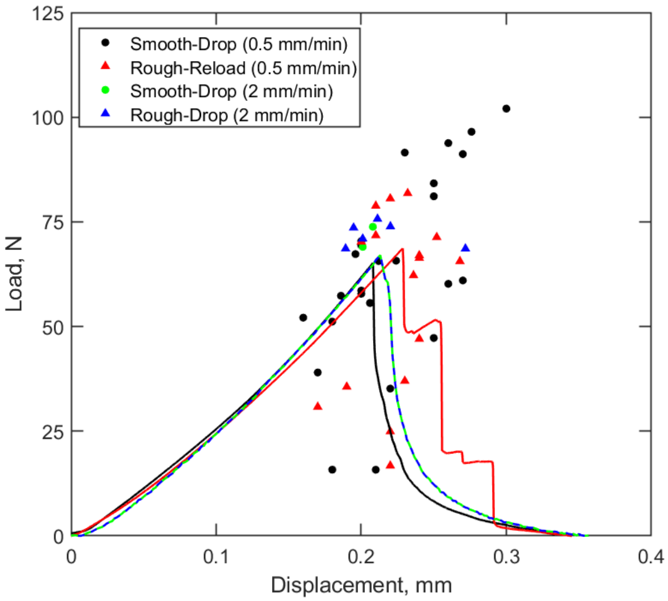

Figure 4.10: Load-Displacement curves for the 0.5 mm/min and 2 mm/min displacement rates. These curves show the representative curves for different post-initiation behaviors with respect to the fracture surface features.

behavior, the roughness features observed are called hackle marks; particularly, these are specific types of hackle marks called twist hackles [87]. Twist hackles can be identified by the shear lips (ridge-like) structure lying parallel with the macroscale direction of crack growth[9] [87, 106]. These twist hackles are an indicator of the presence of slight mode mixity, particularly, Mode-I (opening mode) and Mode-III (tearing mode) [87, 96, 106, 107, 108]. Other experimental works exploring pure Mode-III fracture toughness in polymers have observed similar twist hackles; however, the number of twist hackles and their sizes are far larger owing to those tests being purely Mode-III or larger degrees of mode mixity [105, 106, 109]. Experimental errors such as minor sample misalignment, grip fixture misalignment, or non-parallel clevis pins can induce some level of mode mixity in the test. However, the origin of these twist hackles was observed to be on the pre-crack surface, indicating that

---

[9] In Figure 4.11, the crack growth starts at the pre-crack front (red line) and extends away from the root of the pre-crack indicated on the figure.

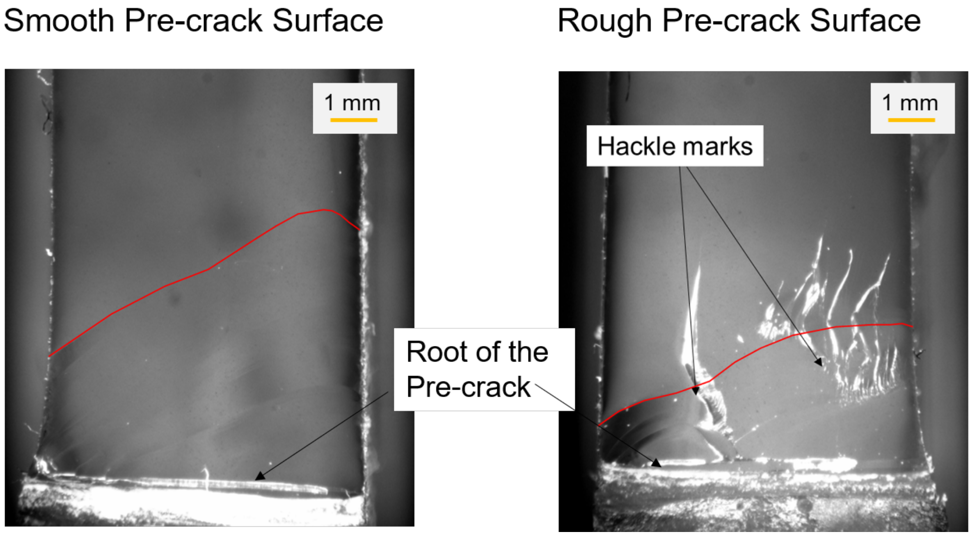

Figure 4.11: Left: a smooth fracture surface with no hackles or surface roughness present. Right: a rough pre-crack surface exhibiting presence of hackle marks in the pre-crack region, which extend in to the crack growth region as well.

they must have formed before testing during the pre-cracking process. It is believed that minor variations in the angle at which the razor blade strikes the sample during razor blade tapping, and misalignment of the sample notch relative to the direction of the tapped razor blade may have resulted in the formation of the observed twist hackles. If the pre-crack plane profile is inclined relative to the through-thickness direction, it may also create a component of force in the through-thickness direction under Mode-I loading and may result in mode mixity.

The samples that undergo fracture by pure Mode-I loading result in a smooth flat fracture surface, and thus require lesser amount of work to create two new fracture surfaces which allows crack growth [87, 105, 106]. This is owing to the lesser surface area of the fracture surface in this configuration. However, with the presence of twist hackles, the surface area is larger for the same thickness, and hence more energy is required for fracture [105, 110]. In this study, a slow displacement rate of 0.5 mm/min was used for fracture testing. It is believed that at this rate, the strain energy accumulation occurring in the sample is gradual enough to capture this difference in energy required for crack propagation. Thus, for a sample containing twist hackles, the energy required for fracture is accumulated slowly after crack initiation, resulting in the reloading behavior that is observed. From Figure 4.11 (Right), it can be observed that the twist hackles propagate further as the crack initiates and extends, and finally, the hackles merge into the flat horizontal plane. This indicates that twist hackles originating in the pre-crack surface affect the crack propagation as well by increasing the surface area along the path of crack propagation.

Another important factor contributing to the reloading behavior is the occurrence of localized plastic flow ahead of the crack tip. At lower strain rates, the time scale permits polymer chains to have a higher degree of mobility leading to more plastic flow resulting in localized plastic behavior [110, 111, 112]. In contrast, at higher strain rates the time scale does not allow much polymer chain mobility and thus lesser amount of localized plastic flow occurs [110, 111, 112]. It is believed that at the 0.5 mm/min displacement rate, localized plastic flow occurs ahead of the crack tip, resulting in crack tip blunting [28, 111]; as crack tip blunting occurs, additional energy is required to overcome the plastic deformation thereby causing reloading until the critical fracture energy is reached again before the crack is allowed to extend. To test this hypothesis, one additional batch of 8 neat epoxy samples was tested at a 2 mm/min displacement rate. Figure 4.10 shows the load-displacement curves for the batch of samples tested at 2 mm/min. Although there were some samples that showed pre-crack surfaces containing twist hackles (Figure 4.11 (right)) and some that exhibited smooth surfaces (Figure 4.11 (left)), none of the higher loading rate samples exhibited reloading behavior. Rather, the load dropped after crack initiation and gradually reduced to zero load. Thus, the higher displacement rate disallowed significant plastic flow and prevented crack tip blunting. Moreover, the faster rate of strain energy accumulation meant that the critical fracture energy was attained rapidly, leading to crack extensions without any reloading behavior.

The new methods of quantifying pre-crack characteristics as well as the in-depth understanding of how pre-crack characteristics influence the fracture toughness of the material and its crack propagation may lead to better engineering design and post-design evaluations of epoxy composites used in structural applications.

Part II

Structural Health Monitoring of Polymer Bonded Energetics

Chapter 5

Introduction

(The following chapter contains sections taken from "N Shirodkar et al 2019 Smart Mater. Struct. 28 104006 - Strain and damage sensing of polymer bonded mock energetics via piezoresistivity from carbon nanotube networks `http://dx.doi.org/10.1088/1361-665X/ab3dcd`. (`https://iopscience.iop.org/article/10.1088/1361-665X/ab3dcd/meta`)". This paper is a published manuscript authored by the Nishant Shirodkar, who is also the author of this dissertation document.)

5.1 Polymer Bonded Energetics/Explosives (PBE/PBX): A Review

Polymer bonded energetics are a classification of composites that combine energetic particulates into a polymer matrix. The polymer binder protects the energetics from stimuli such as inadvertent mechanical or thermal loading and adds stability and strength to the material [113]. These materials commonly find applications in the aerospace propulsion sector and several other military applications as well. Binders often used for energetic applications include epoxy, HTPB (Hydroxyl-terminated polybutadiene), and PDMS (Polydimethylsiloxane)[113]. Common energetic particulates like HMX (cyclotetramethylene-tetranitramine), TATB (triamino- trinitrobenzene), PETN (pentaerythritol-tetranitrate), and RDX (trinitroperhydro-triazine), and are used in a variety of propulsive and explosive applications. A major factor at play in the processing of polymer bonded energetics is safety; accidental fracture or other damage due to impact or fatigue strain can compromise the composite's stability prior to or during ignition. Specifically, damage of this kind could allow localized high-temperature regions or "hot-spots" to appear within the material [114]. Current methods for predicting the potential of such dangerous reactions are stochastic, unreliable, and often reduce to a tested probability of instances in a closed environment when a reaction is instigated [115].

To appease safety and cost considerations of working with these materials, many experimental investigations, including the effort discussed herein, have chosen to substitute the particulate with more inert, and even mock energetic substances which provide similar crystal size and shape, and therefore, can offer similar microstructure and corresponding mechanical behavior [114]. Balzer et al. selected non-aluminized ammonium perchlorate (AP) as a reliably inert energetic crystal with a prevalent history of application in solid rocket propellants to explore mechanical properties and ignition mechanisms [114, 116]. Other studies performed comparisons of typical crystal size and shape between ammonium perchlorate and sugar, finding that the monoclinic crystalline structure of sugar makes it a valid candidate to match the geometry of energetic crystals in actual application [114, 117, 118, 119]. These efforts justify the use of sugar as a safe mock energetic particulate to simulate real energetic crystals' microstructure and capture similar mechanical properties.

The ability to perform diagnostics on energetic materials post-manufacturing has become a strongly supported endeavor. Studies have demonstrated that crystal coarseness has direct impact on the strength of various particulate compositions within the same binder, showing that composites of higher coarseness had the lowest mechanical strength of materials tested

[113, 118]. Palmer et al. explored the material properties of a variety of energetics with various combinations of binders and particulate crystal sizes utilizing Brazilian disk tests to determine tensile strength of tested energetics [120]. It was noted that the primary mechanisms of damage for the class of energetics with rubbery elastomer binders were debonding, binder void formation, and void expansion on the microscale, all of which highlight the influence of binder on failure characteristics [120]. X-ray tomography was performed during these experiments, showing no obvious crystal fracture in either the actual energetics, ammonium perchlorate, or sugar, proving instead that debonding and void growth dominated the modes of failure.

With both mechanical failure and hot-spot initiation in energetics occurring due to complexities at the microscale, current methods of structural health monitoring (SHM) operating on the macroscale are therefore, incapable of capturing these potential failure modes prior to possible accidental ignition. The field of SHM is currently dominated by externally mounted sensors which can function in real-time but only offer relatively large crack detection, and visualization techniques like X-ray tomography and micro-CT which can only diagnose internal damage after, rather than during loading [121, 122]. As such, producing a micro/nanoscale sensing network internally suspended within the matrix of a composite could be the exact development which makes real-time damage diagnosis possible, revolutionizing the methods of characterizing energetic material integrity. Carbon nanotube (CNTs) embedded nanocomposites are currently being studied for their multi-functional benefits in piezoresistivity [123, 124]. A nanocomposite can, in principle, offer SHM capability by developing localized changes in electrical properties when experiencing micro/nanoscale damage which interrupts the conductive pathways of CNTs throughout an otherwise insulative binder material. Additionally, a real-time sensing system offsets the down-time maintenance/diagnosis costs associated with the methods mentioned above, thereby leading to cheaper monitoring solutions in the long term. The specific application of nanocomposite piezoresistivity to energetic materials have been explored thoroughly with proof of concepts for SHM. Experiments have been conducted to obtain significant resistive and dielectric sensitivity to quasi-static mechanical tension and compression to failure, dynamic low-velocity impact, and thermal loading [117, 119, 123, 124, 125, 126].

The addition of an ignition accelerant such as aluminum powder to ammonium perchlorate crystals, has been demonstrated to cause a significant increase in the combustion performance[127]. For the purposes of our work, this augmentation of energetics with the inclusion of aluminum powder increases overall material conductivity and, therefore, requires additional investigation into their effects on the piezoresistive response of nanocomposites. Zhang *et al.* implemented the use of conductive filler particles on their own in piezoresistive applications, demonstrating that a conductive filler like aluminum powder, in large enough concentration dispersed in a rubbery elastomer binder, could experience piezoresistive response to mechanical load [128]. In this experimental effort, sugar crystals representing mock energetic particles were used in formation of the tested nanocomposites. Multi-walled carbon nanotubes were added to the PDMS polymer binder to impart strain/damage sensing abilities, and aluminum powder was also added to the material to investigate its effect on the sensing abilities of the MWCNT networks. Thus, four material systems, sugar-PDMS, sugar-Al-PDMS, MWCNT-sugar-PDMS, and MWCNT-sugar-Al-PDMS were fabricated. The piezoresistive response was observed in conjunction with the strain and mechanical load. This response was quantified via gauge factors (GF) which related the change in electrical properties to the applied strain. It is noted in literature that carbon-fiber composite laminates, and other MWCNT/SWCNT embedded polymer strain sensing devices have a reported gauge factor of 3-10 within the elastic regime [129, 130]. Some commercial polysilicon strain sensors and high strain graphitic based sensors have reported resistance gauge factors of 30-300 in the elastic regime [129, 130, 131]. Calculating the GFs for the mock energetics studied herein, a comparable evaluation of the structural health monitoring capabilities of dispersed MWCNT networks in polymer bonded energetic materials was made.

Chapter 6

Strain and Damage Sensing in Mock PBEs emmbedded with Carbon Nanotube (CNT) Networks

(The following chapter contains sections taken from ”N Shirodkar et al 2019 Smart Mater. Struct. 28 104006 - Strain and damage sensing of polymer bonded mock energetics via piezoresistivity from carbon nanotube networks `http://dx.doi.org/10.1088/1361-665X/ab3dcd`*. (*`https://iopscience.iop.org/article/10.1088/1361-665X/ab3dcd/meta`*)”. This paper is a published manuscript authored by the Nishant Shirodkar, who is also the author of this dissertation document.)*

6.1 Fabrication of Polymer Bonded Energetic Nanocomposites

6.1.1 Materials

In this study, the polymer binder used is Polydimethylsilioxane (PDMS), an elastomer polymer purchased from Dow Corning (product sold under the commercial name “Slyguard

184"). Monoclinic sugar crystals with an average particle size of ∼230 μm (Domingo®) granulated cane sugar) were used as mock energetic particulates. Atomised aluminum powder was purchased from Pyrochemicals Ltd. having a reported particle size of ∼30 μm and was used in aluminized specimens. The multiwalled carbon nanotubes (MWCNTs) used in this study were obtained from NanoLabs Inc. (PD15L1-5, research grade MWCNTs) and have a reported purity in excess of 95% (impurities typically of residual iron and sulphur). The outer and inner diameter of the MWCNTs was reported as 15±5 nm and 7±2 nm, respectively, with a reported longitudinal length of 3±1.5 μm.

6.1.2 Preparation of mock energetic composites

Four different types of polymer bonded mock energetics were fabricated, each with a different constituent material. This was done to assess the effects of mock energetic constituents on the piezoresistive response and mechanical properties. The types of mock energetics fabricated and their respective constituent compositions are shown in Table 6.1.

Table 6.1: Compositions of the four material systems developed. All the percentages shown are in terms of weight percent. MWCNTs weight percent is defined as a percent of PDMS weight (relative to the weight of PDMS). *In materials with MWCNTs, the mixture of PDMS and MWCNTs is first obtained and then the required quantity of 20% of the CNT embedded polymer binder is utilized for fabrication.

Material System	Sugar	Aluminum	Total Particulates	Polymer Binder	MWCNTs	Total
Sugar-PDMS	80%	0%	80%	20%	0%	100%
MWCNT-Sugar-PDMS	80%	0%	80%	20%	0.8%	100%*
Sugar-Al-PDMS	64%	16%	80%	20%	0%	100%
MWCNT-Sugar-Al-PDMS	64%	16%	80%	20%	0.8%	100%*

Material systems without MWCNTs are referred to as ”Neat” whereas those with added MWCNTs are referred to as ”Hybrid” mock energetics. It is noted in several other works that polymer bonded energetics are manufactured with mixing ratios of ∼80-95% solid particulate matter (energetic particles) and ∼20-5% polymer binder depending upon their applications[114, 132, 133, 134, 135, 136, 137]. In this study, a consistent weight ratio of 80:20 corresponding to 80% by weight, particulates; and 20% by weight, polymer binder PDMS was maintained for preparation of all the material systems. For Hybrid specimens, an additional 0.8% by weight MWCNTs were added to PDMS (calculated relative to the weight of the PDMS in grams, corresponding to 0.16% of the entire weight of the mixture). The MWCNTs and PDMS mixture was first obtained and then weight equivalent to 20% was utilized for fabrication. Polydimethylsiloxane (PDMS) is used as a polymer binder due to its ability as an elastomer to sustain good amount of mechanical insult which makes it safer to work with energetics as they are less sensitive to mechanical damage. PDMS has a ∼90 min working time which allows sufficient degassing and mixing of particles before curing begins leading to easier material fabrication.

The tension and compression specimens were prepared in batches of four specimens (of the same material system) according to ASTM standards D638 and D695, respectively [138, 139]. Type I dog-bone type tension specimen and cylindrical long compression specimens, weighing ∼30 g and ∼20 g respectively, are shown in Figure 1 (electrode placements for piezoresistive measurements, as shown in the figure, are not prescribed in ASTM standards).

Figure 1c illustrates the expected piezoresistive response of the material under tension and compression. An important note in this expected outcome is the behavior in compression where the response changes its trend due to occurrence of damage, which is explain further.

For preparation of neat specimens, measured quantities of individual constituents were first collected under a fume hood in glass beakers. In aluminized specimens i.e. material systems

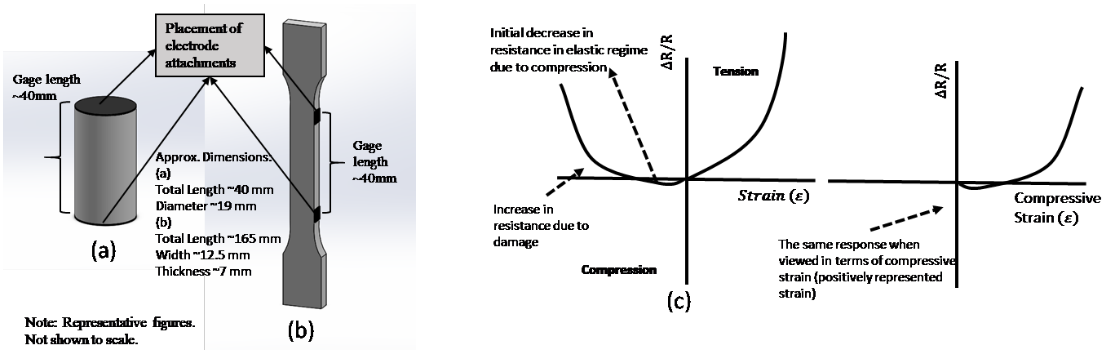

Figure 6.1: Schematic representation of the prepared ASTM standard specimens shown along with the location of the electrode attachments on the specimens. (a) Long Compression specimen (b) Dog-bone Tension specimen. The electrodes in both specimens were attached at ∼40 mm apart, thus keeping the gauge length for electrical measurements consistent for both specimens. Figures shown are not to scale. (c) Expected piezoresistive response of MWCNT specimens in tension and compression. Same response as viewed when represented in compressive strain (downward direction is taken as positive)

with a particulate mixture of sugar crystals and aluminum powder, the particulate mixture was mechanically mixed thoroughly for ∼10 min. until a visually homogenous distribution was obtained. The polymer PDMS has a binder resin (Part A) and a curing agent (Part B) both of which were mixed in a ratio of 10:1. Through mechanical mixing, a homogenous mixture of Part A and Part B was obtained. The particulate mixture was added slowly in small quantities to the PDMS mixture. The particulate and PDMS mixture was degassed in a vacuum chamber for ∼30 minutes under 90 MPa vacuum pressure to remove entrapped air. This degassed mixture was then pressed in the molds and degassed for a second time for ∼20 minutes under 90 MPa vacuum pressure to remove remaining trapped air. The presence of voids was reduced further by compressing the pressed specimen with a counter-mold using a compression weight of ∼10 N (corresponding to a 1 kg metal cube placed on top of the counter mold). The prepared mold is then cured in an oven (MTI corp. Vacuum Oven) at 135°C for 40 minutes, found to be the optimum temperature and time for uniform curing via trial and error. The specimens were removed from the oven and allowed to cool at room temperature for a period of 24 hours before being extracted from the molds.

For preparation of hybrid specimens, the same process was followed, except that the MWCNTs had to be mixed with the Part A of the PDMS polymer prior to mixing with Part B. The MWCNTs were first mixed with a measured quantity of acetone (2.5 ml for every 0.01 g of MWCNTs), a low viscosity liquid that aids in the proper dispersion of MWCNTs during ultra-sonication. The acetone and MWCNT mixture were sonicated using a Qsonica Sonicator Q500A at 20 kHz frequency and 30% amplitude in a water bath for one hour. The Part A was added to MWCNTs dispersed in acetone and stirred with a magnetic stirrer for ∼15 minutes at 400 rpm. The sonication was repeated again with the Part A, MWCNTs and acetone mixture for an hour with the same parameters. The acetone was then extracted from this mixture using a rotary evaporator (IKA RV-10 rotary evaporator) to obtain a mixture containing randomly oriented dispersed MWCNTs and PDMS Part A. The blend of dispersed MWCNTs in the PDMS Part A was now collected and mixed with Part B and the subsequent processes used for neat specimen fabrication were followed.

A ∼40 mm gauge length for electrical measurements was maintained in both tension and compression specimen types. As shown in Figure 1, the electrodes were applied to the flat surface at the top and bottom of the cylindrical compression specimen on a surface area equal to the surface area of the flat face. In the tension specimens, the two electrodes were attached on the side of the specimen on surface area composed of the specimen thickness (∼7 mm) and 10 mm in length along the gauge section. These surfaces were first coated with high conductivity silver-epoxy (MG Chemicals Silver Conductive Epoxy) to minimize contact resistance. After the epoxy had completely cured for ∼1 hour at room temperature, 30-gauge tin coated copper wires were attached using conductive paint (Bare® Conductive Paint) and allowed to dry at room temperature for a period of 24 hours. The conductive paint was observed to have sufficient strength to hold the wire electrode in place throughout testing.

6.2 Mechanical and Electrical Characterization

For characterization of mechanical properties and to evaluate the piezoresistive response of the different composites, quasi-static mechanical tests were conducted. Composite specimens were subjected to a monotonic uniaxial tensile load and a monotonic compressive load using a universal testing frame (Admet MttestQuattro). These tests were displacement-controlled. A constant crosshead displacement of 1 mm/min corresponding to ∼0.025 mm/mm/min strain rate and 4 mm/min corresponding to ∼0.025 mm/mm/min was used for the compression and tension tests, respectively. In conjunction with the mechanical loading, using a two-point measurement technique, the resistance and the reactance of the specimens under mechanical load was gathered by an inductance, capacitance, resistance (LCR) meter (Agilent Technologies E4980A Precision LCR meter)[117, 119, 125, 126]. The LCR meter operated with an output voltage of 2V AC and a measurement frequency of 10 kHz. It is noted that the fabricated neat composite specimens display an insulator type behavior and therefore demonstrate a dependence on input frequency. At the chosen 10 kHz frequency, the resistance was low enough (in the kΩ range) to get reliable readings and there was no strong charging behavior exhibited by the specimens.

The universal testing frame has manually tightened grips and hence the gripping pressure may vary across repetition of tensile tests. The metal grips were first discharged and then completely insulated electrically using paper and electrical tape as shown in Figure 2a. In the compression tests, additional wooden chips were attached to the testing frame fixtures to completely insulate the specimen from making electrical contact with any metal surfaces

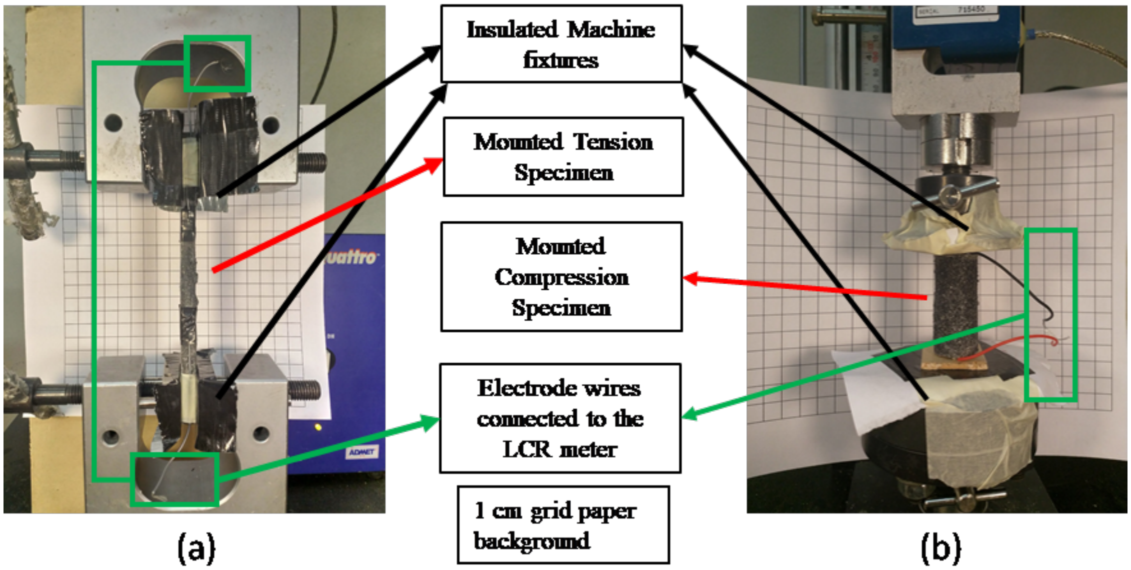

Figure 6.2: Photograph of the test setup and testing frame fixtures. (a) MWCNT-sugar-Al-PDMS tension test specimen and (b) MWCNT-sugar-Al-PDMS compression specimen mounted in the electrically insulated testing fixtures. In the image above the electrode wires attached to the specimens are shown as connected to the LCR meter during testing.

during testing (see Figure 2b). Four samples for each material type and loading were fabricated and tested (until failure) to understand repeatability and to obtain average bulk properties and their variation. Through the piezoresistive response i.e. change in bulk resistance and reactance as a function of applied strain, the damage/strain-sensing abilities of the dispersed MWCNTs were studied.

6.3 Results and Discussion

6.3.1 Qualitative/Visual Assessments

The particle sizes of the materials used were observed to play an important role in affecting the mechanical properties, surface finish, visual/chromatic characteristics and more importantly the piezoresistive response. Figures 3a and 3b show SEM microscopic images demonstrating nominal particle sizes for as received sugar crystals and aluminum particles. The disparity in particle size between sugar and aluminum powder creates a bimodal distribution of particles in the sugar and aluminum material systems. Figure 4(a-d) shows images of tension and compression specimens of all the material systems (tested to failure) investigated in this study. The neat sugar-PDMS has a distinct white color arising from the transparent PDMS and apparent white hue of sugar crystals. Introduction of even a small concentration (0.8 wt%) of MWCNTs into this material system imparts a distinct black hue to the MWCNT-sugar-PDMS specimens [119, 125]. Addition of aluminum powder imparts a greyish hue to sugar-Al-PDMS specimens, and when combined with the addition of MWCNTs in the MWCNT-sugar-Al-PDMS, the resulting specimens are dark-greyish in color.

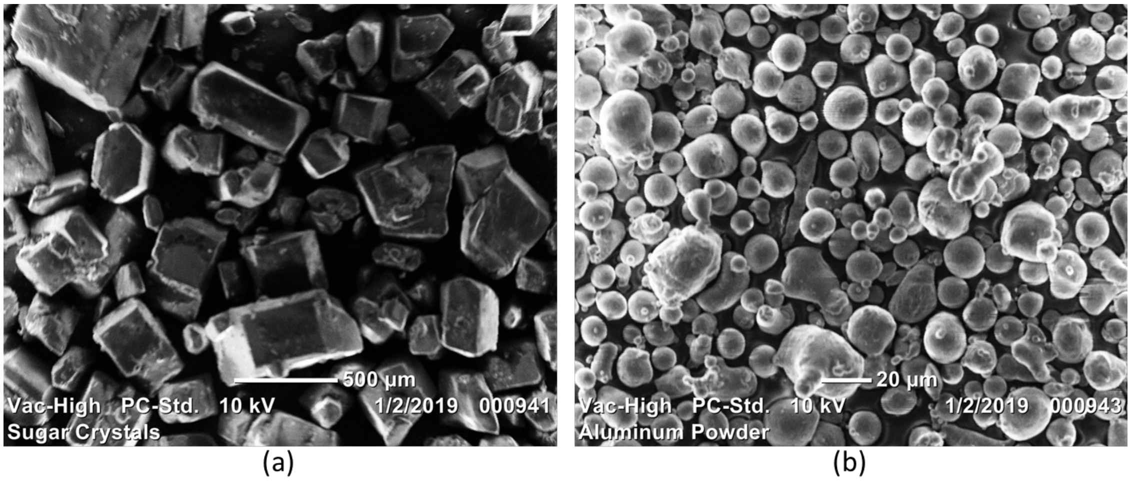

(a) (b)

Figure 6.3: SEM images of particulates used (a) Monoclinic Sugar Crystals ∼230 μm (b) Aluminum Powder ∼30 μm. These images were used to verify the manufacturer specification for particle size and compared with particle size distributions obtained via previous studies for the same materials obtained from same manufacturers

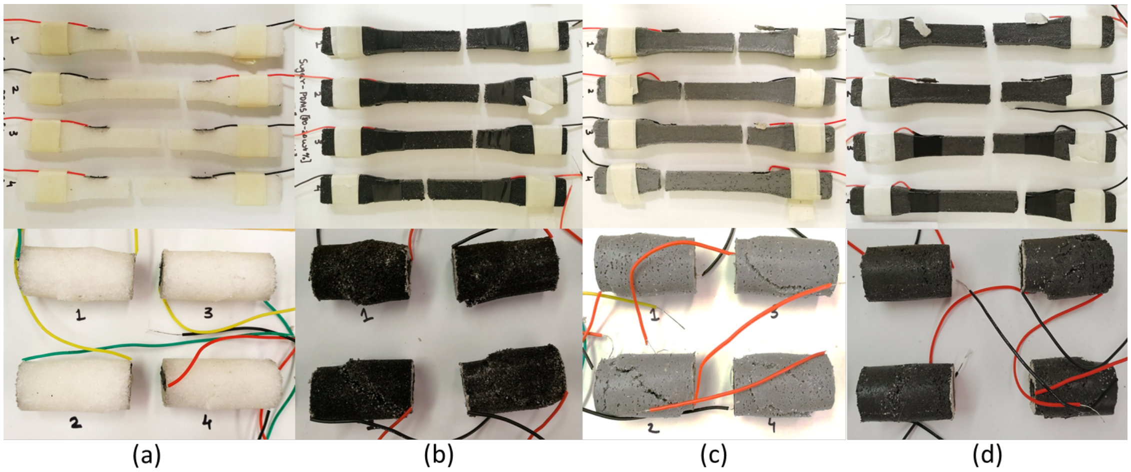

Figure 6.4: Photographs of tested specimens of all material systems post failure (a) Neat Sugar-PDMS (b) Hybrid MWCNT-Sugar-PDMS (c) Neat Sugar-Al-PDMS (d) Hybrid MWCNT-Sugar-Al-PDMS

6.3.2 Effects of adding CNTs on Mechanical Properties

Uniaxial and monotonic tensile and compression tests were conducted to evaluate the mechanical properties of all the material systems. In Figure 5, the stress-strain curves for neat sugar-PDMS and hybrid MWCNT-sugar-PDMS specimens in tension (Figure 5a-b) and compression (Figure 5c-d) are shown. The shadow regions shown in the stress-strain response represent two standard deviations of the results obtained and averaged from four test specimens of each type and each loading case for each material system. The averaged data has sharp changes in the shadow regions corresponding to different failure strains for the specimens, and thus reduction in the number of specimens averaged at higher strain levels. This abrupt change may not be very distinct in some cases if the fracture strain is fairly consistent for a given material system. However, in order to be able to directly assess the correlation between the stress-strain response and the piezoresistive response consistently for all material systems, one specimen stress-strain response is plotted as a solid line along with the shadow region. The representative tension specimen is selected by observing the location of failure in each specimen and ideally selecting one with the visible macroscale crack forming closest to the middle of the gauge section. In compression, the representative specimen is selected as the one with a clear crack formed furthest from the electrode surfaces on the top and bottom of the specimen.

In tension, as seen in Figure 5a and 5b, the mechanical response of sugar-PDMS and MWCNT-sugar-PDMS shows an initial elastic response, followed by a region of slightly changing stress plateau (believed to be caused by steady growth of distributed micro-cracks) and finally, a brittle-like failure due to macroscopic crack formation and subsequent failure (5,11,14). Such a stress-strain behavior is not observed in prior mechanical characterization studies with just PDMS and is likely a result of the particulate nature of the mock energetics. The observed stress plateau (referred to as microscopic damage region hereafter) is believed to be caused due to interfacial de-bonding between the particulates and the polymer leading to formation of voids from which micro-cracks nucleate. The sharp edges of the monoclinic sugar particles additionally create stress concentrations adversely affecting the strength [117, 125]. As these micro-cracks begin to grow in number, the stress distribution throughout the specimen influences the formation of large macroscopic cracks, and then an abrupt, brittle-like failure follows [120, 140]. In contrast with expected outcomes, the tensile modulus reduced with addition of MWCNTs. (The apparent increase in slope in the elastic region of Figure 5b is a result of the larger strain axis scale needed to accommodate the larger variation in stress-strain response with the addition of MWCNTs). A tensile modulus of 25.6±6.8 MPa for the neat sugar-PDMS and 21.3±12.3 MPa for hybrid MWCNT-sugar-PDMS was calculated for the elastic region. A key factor during fabrication of hybrid specimens is the use of acetone to disperse CNTs. It is noted in other studies that acetone can permeate PDMS even at room temperature. Since the fabrication was done in room temperature and the PDMS was subjected to a long period of exposure to acetone during sonication, it is hypothesized that some acetone might still be present in the PDMS, which evaporates during curing leaving behind some voids. These voids may cause the observed reduction in the tensile modulus of the MWCNT-sugar-PDMS and MWCNT-sugar-Al-PDMS as compared to their non-MWCNTs variants, respectively. Solubility of sugar crystals and aluminum in acetone is practically insignificant, and moreover, the particulates are added post acetone extraction and hence acetone is not expected to have any effect on the sugar crystals or aluminum. The peak stress was slightly higher for the hybrid MWCNT-sugar-PDMS at 0.16±0.03 MPa as compared to 0.11±0.005 MPa for the neat sugar-PDMS. The average fracture strain for neat sugar-PDMS was 4.33±0.35% and 15±0.49% for hybrid MWCNT-sugar-PDMS, indicative of the potential for MWCNTs' ability to bridge nanoscale cracks.

Unlike in the tensile response, a distinct plateau is not seen in compression. Instead, there is a more gradual transition to microscale and macroscale damage regimes with the peak stress much closer to the region II – region III transition than region I – region II as was the case under tensile loading. It was noted that PDMS and sugar crystals do not form chemical bonds, but rather the sugar crystals are shrunk fit by the PDMS and have a weak cohesive zone due to van der Waals effects. These characteristics cause tensile peak stress to be near the region I to region II transition with a plateau of distributed damage, justifying the comparative strength of the material systems in compression. Furthermore, the microscale and macroscale cracks formed during loading, re-establish contact and better maintain load columns in compression, justifying why peak stress appears near region II - region III transition. As a result, there is not a noticeable abrupt macroscopic failure as observed in tension, but rather a peak and then reduction in stress carrying capacity of the material as macroscale damage occurs. The average compressive modulus was calculated as 37.04±13.6 MPa for neat sugar-PDMS and 36.11±15.2 MPa for hybrid MWCNT-sugar-

PDMS. The peak stress was measured as 0.39±0.09 MPa and 0.54±0.031 MPa, respectively. The average fracture strain (measured when the stress dropped to approximately ∼30-50% of peak stress) for neat sugar-PDMS was 17.35±2.78%, with an increase for hybrid MWCNT-sugar-PDMS at 25.30±1.40%.

(a) Sugar-PDMS (Tension)

(b) Sugar-PDMS-CNT (Tension)

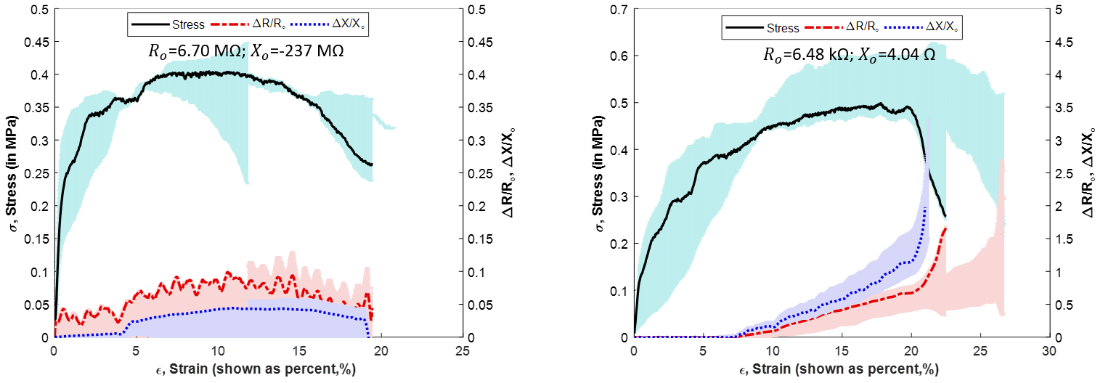

(c) Sugar-PDMS (Compression)

(d) Sugar-PDMS-CNT (Compression)

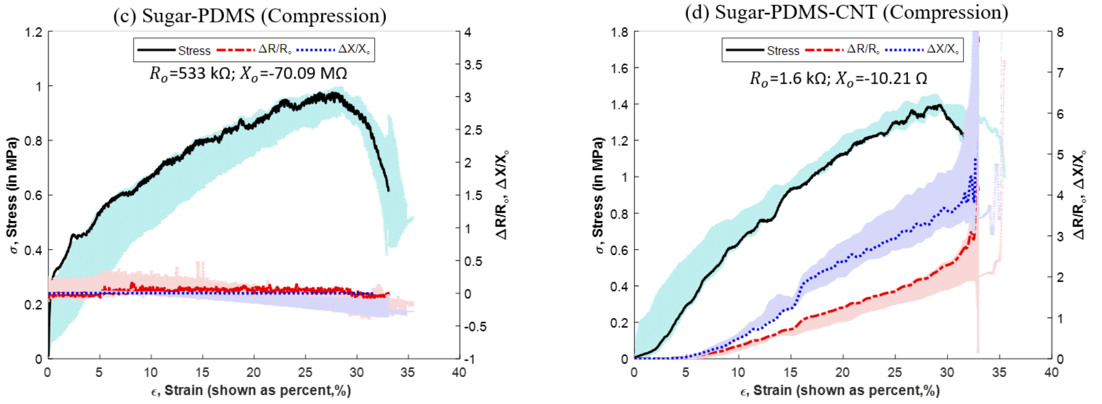

Figure 6.5: Stress vs Strain curves (black solid line) for tension and compression of neat sugar-PDMS, and hybrid MWCNT-sugar-PDMS shown with the piezoresistive response upon applied strain represented by the instantaneous change in resistance $R/R_{\circ}$ (red dashed-dotted line), and reactance $X/X_{\circ}$ (blue dotted line). (a) Neat sugar-PDMS in tension and (c) in compression (b) Hybrid MWCNT-sugar-PDMS in tension (d) in compression

6.3.3 Effects of addition of Aluminum Powder on Mechanical properties

Figure 6 demonstrates the effects of adding of aluminum particles to mock energetics on the mechanical properties. A marked increase in mechanical properties was observed in sugar-Al-PDMS and MWCNT-sugar-Al-PDMS in comparison with the sugar-PDMS and MWCNT-sugar-PDMS, respectively. This increase is thought to be a result of addition of stiffer aluminum which increases the overall stiffness of the specimen. Additionally, a smaller particle size is known to improve mechanical strength of polymer composites with bi-modal particulate fillers due to increased van der Waals interactions. The smaller, stronger spherical aluminum particles are more densely packed and shrunk fit by the binder making the van der Waals force more significant.

The tensile modulus was calculated as 51.7±9.95 MPa for sugar-Al-PDMS, and 32.5±11.7 MPa for the MWCNT-sugar-Al-PDMS. It is again believed that the decrease in modulus of the hybrid aluminized MWCNT specimens relative to the neat aluminized specimens is due to the adverse effects of residual acetone on PDMS during curing as discussed earlier. The average peak stress for the aluminized materials was measured as 0.36±0.03 MPa and 0.31±0.049 MPa, with and without MWCNTs respectively. The average fracture strain was measured as 13.26±0.32% for neat sugar-Al-PDMS and 20.08±1.21% for hybrid MWCNT-sugar-Al-PDMS. No significant difference in the compressive modulus and fracture strain of the aluminized materials was observed. The compressive modulus was calculated as 65.79±17 MPa for neat sugar-Al-PDMS and 66.67±9.7 MPa for hybrid MWCNT-sugar-Al-PDMS. There is noticeable enhancement in peak stress due to addition of MWCNTs with 1.41±0.021 MPa for the hybrid MWCNT-sugar-Al-PDMS and 0.96±0.019 MPa for the neat sugar-Al-PDMS. The average fracture strain was measured as 34.06±0.62% and 33.77±0.85%,

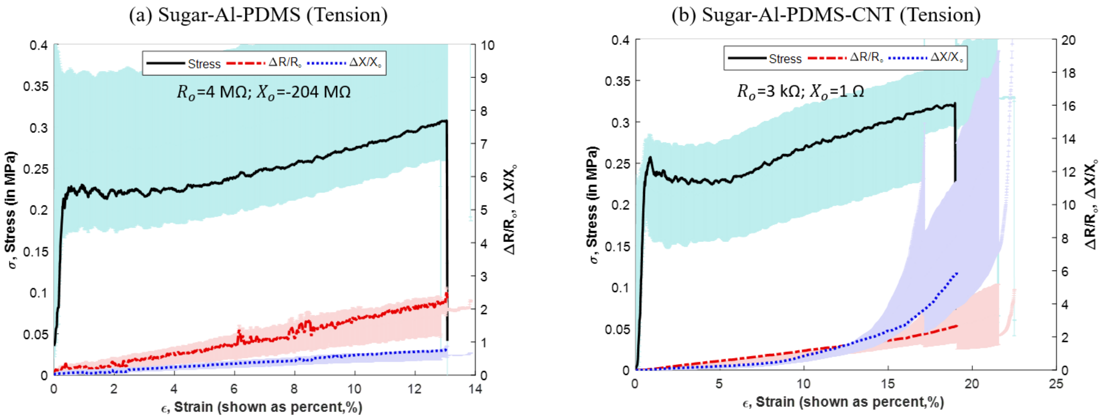
(a) Sugar-Al-PDMS (Tension)

(b) Sugar-Al-PDMS-CNT (Tension)

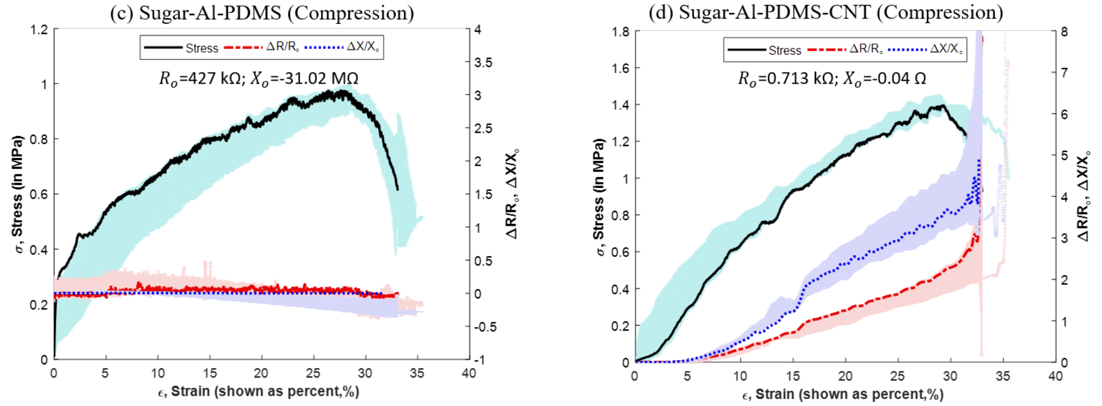
(c) Sugar-Al-PDMS (Compression)

(d) Sugar-Al-PDMS-CNT (Compression)

Figure 6.6: Stress vs Strain curves (black solid line) for tension and compression of aluminized sugar, and hybrid sugar-Al-CNT shown with the piezoresistive response upon applied strain represented by the instantaneous change in resistance $R/R_\circ$ (red dashed-dotted line), and reactance $X/X_\circ$ (blue dotted line). (a) Neat sugar-Al-PDMS in tension and (c) in compression (b) Hybrid MWCNT-sugar-Al-PDMS in tension (d) in compression

respectively for neat sugar-Al-PDMS and hybrid MWCNT-sugar-Al-PDMS. These values correspond to an approximate 150% increase in peak stress and 60% increase in fracture strain relative to their non-aluminized counterparts. Figure 7 summarizes the comparisons in tensile and compressive modulus, peak stress, and failure strain for all material systems tested.

Figure 8(a-d) shows the SEM micrographs of post-failure fracture surfaces for the four different material systems tested in this study. At lower magnification (∼50x) several sugar crystal pull-out regions are observed. The particles still present on the surface have a

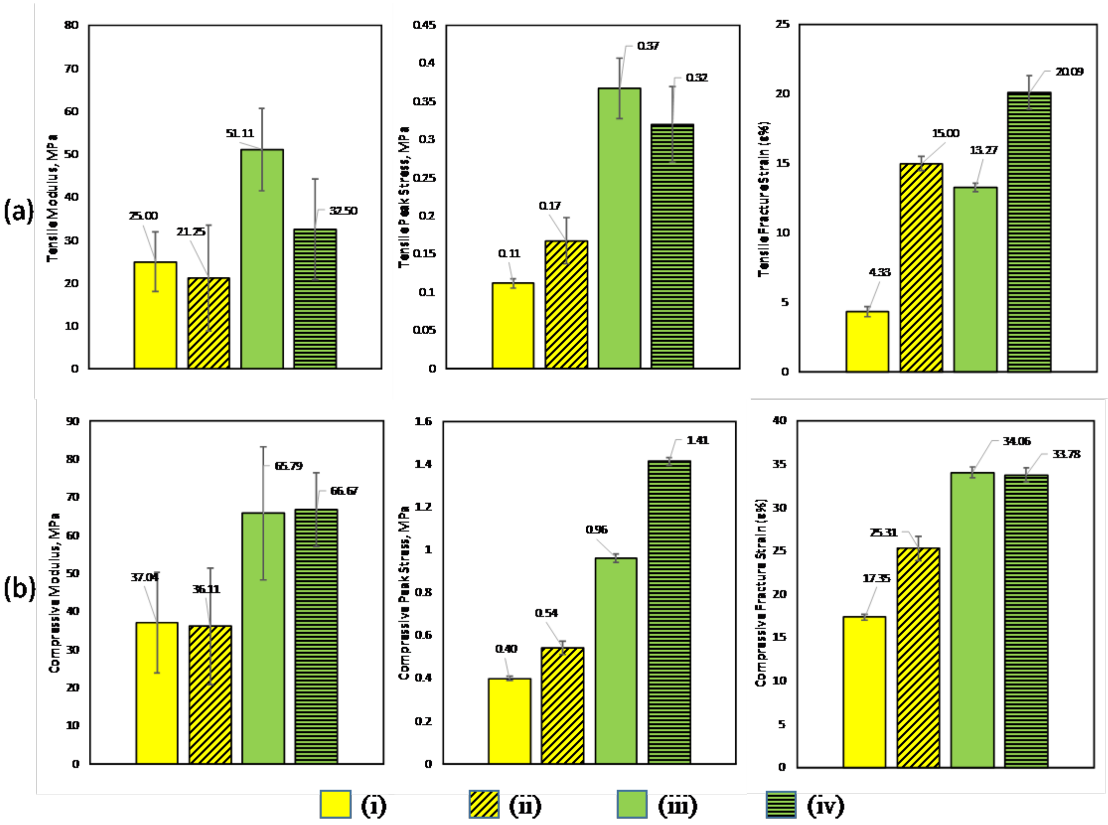

Figure 6.7: Comparison of mechanical properties of the various material systems tested (i) Sugar-PDMS (ii) MWCNT-Sugar-PDMS (iii) Sugar-Al-PDMS and (iv) MWCNT-Sugar-Al-PDMS. (a) Tensile Modulus, Peak Stress, and Fracture Strain of all material systems under tension (b) Compressive Modulus, Peak Stress, and Fracture Strain of all material systems under compression.

distinct surface separation from the PDMS binder around it. This separation is more evident in sugar crystals which suggests that sugar forms very weak bonds with PDMS largely comprised of van der Waals interactions. Additionally, It has been observed in other literature that aluminum powders have a surface roughness with peaks and valleys ranging in the nanometer scale. It is believed that this roughness increases the wetted area of the filler and adds to the cohesion strength of aluminum particles with the polymer matrix. Smaller surface separation zones seen in Figure 8d are indicative of relatively better cohesion with the PDMS binder. Moreover, observations from the SEM micrographs

(Figure 8d) show that owing to the disparity in the particles sizes of sugar and aluminum, the aluminum powder can seep through the small spaces between sugar particles and reinforce the polymer matrix in that region as well.

At higher magnifications (<=1 μm), dispersed MWCNTs are observed in the PDMS binder (Figure 8b and 8d). It must be noted that despite the $\sim 3\mu$m average length of the MWCNTs, on the fracture surface we can observe only those MWCNTs that have pulled out from opposite fracture surface. Additionally, the MWCNTs on the observed surface are partially visible, with a possibility that a significant portion is embedded beneath the fracture surface. The presence of MWCNTs near the fracture surfaces is a strong indication that the resulting piezoresistive sensing observed in the hybrid specimens results from MWCNTs networks.

Figure 9a shows an SEM micrograph of one of the many micro-cracks observed on the fracture surface. These micro-cracks are responsible for distribution of damage throughout the specimen resulting in a distinct stress plateau (microscale damage region). It is believed that the presence of MWCNTs in regions near or at these micro-cracks lends the MWCNTs network the ability to sense microscale damage. Figure 9b shows a SEM micrograph of a MWCNT-sugar-PDMS specimen, that highlights the presence of micro-porosities in hybrid specimens discussed earlier.

6.3.4 Piezoresistive Response

In conjunction with the mechanical loading, the piezoresistive response was obtained using a two-point measurement method. To evaluate the total effective resistance of a material to AC current, the impedance was measured using an LCR meter and the real and imaginary components, resistance and reactance, respectively, were separated and analyzed. Table 2 provides the average initial values for resistance (R_o) and reactance (X_o) for the tension

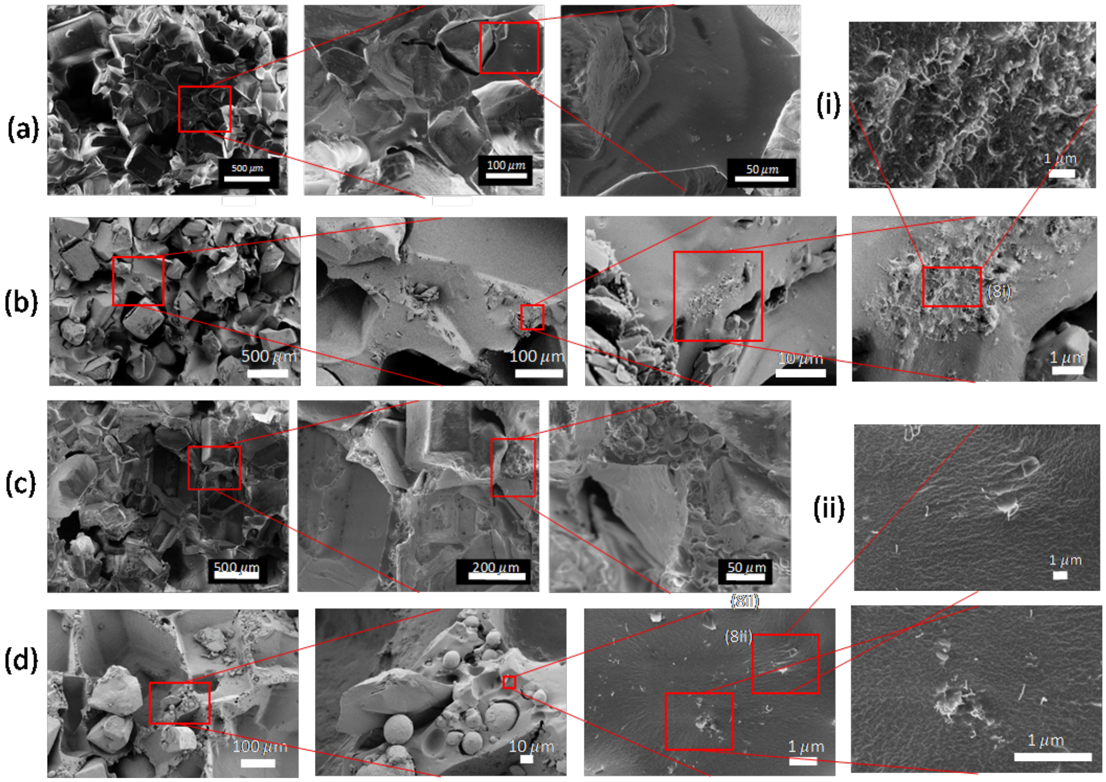

Figure 6.8: SEM micrographs of post-failure fracture surfaces of (a) Sugar-PDMS (b) MWCNT-Sugar-PDMS (c) Sugar-Al-PDMS (d) MWCNT Sugar-Al-PDMS. Zoomed in regions rich in MWCNTs are shown separately in the last row and are interlinked in the larger scale SEM images. MWCNT rich region observed on the fracture surface of (i) MWCNT-sugar-PDMS specimens and (ii) MWCNT-sugar-Al-PDMS specimens. Scale bars for every image are shown in the bottom right corner of that respective image. Regions highlighted by the red boxes are zoomed in further and shown sequentially at different length scales.

and compression specimens of all material systems under absence of mechanical loading (i.e. zero strain values). The piezoresistive response is quantified via the electrical sensitivity to mechanical load given by the gauge factor (shown in equation 1a and 1b) which essentially relates the instantaneous change in resistance (R) or reactance (X) to the corresponding strain. In this study, tangent gauge factors are calculated i.e. the slope of the tangent at the point of interest is used. Note that the strain ε, defined as L/L and measured via crosshead

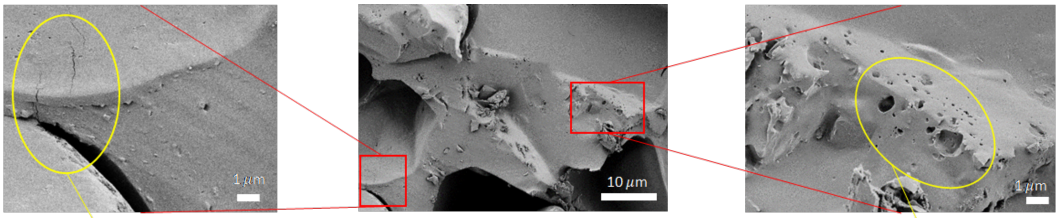

(a) Micro-cracks observed in the polymer matrix surrounding a sugar crystal

SEM micrograph of the fracture surface of a MWCNT-sugar-PDMS specimen

(b) Micro-voids observed in the polymer matrix

Figure 6.9: (a) Micro-cracks observed on the fracture surface, thought to be responsible for sensing in the micro-scale damage region. (b) Micro-porosities observed in the hybrid specimens, i.e. specimens with MWCNTs, due to permeation of acetone in PDMS and subsequent void formation, due to evaporation during curing.

displacement, is used in the gauge factor calculations rather than percent strain.

$$GF_R = \frac{R/R_\circ}{\varepsilon} \quad where \;\; \mathrm{R} = R_i - R_o \;\; (1a)$$

$$GF_X = \frac{X/X_\circ}{\varepsilon} \quad where \;\; \mathrm{X} = X_i - X_o \;\; (1b)$$

The initial electrical properties in Table 2 are higher for tension and lower for compression specimens although the material system is the same. It must be noted that the tension and compression specimens were prepared from the same batch of fabrication and hence consistency is expected in the inherent material properties for both tension and compression samples. Additionally, the electrodes were also attached at a constant gauge length of ∼40 mm in both tension and compression specimens. Considering the relation for resistance, R=ρL/A, where ρ, resistivity and L, length are constant, changes in the effective cross-sectional area of the current path “A” can affect R_o. In tension, the electrodes are attached to the side and therefore, the effective cross-sectional area of current path may not be the cross-sectional area of the tension specimen (∼84 mm^2) but rather may be much lesser than that should the current take a path closer to the electrode side of the specimen. For the

Table 6.2: Average initial resistance and reactance of all the material systems tested herein.

Material System	Tension Specimens		Compression Specimens	
	$R_\circ$	$X_\circ$	$R_\circ$	$X_\circ$
Neat Sugar-PDMS	6.70±0.95 MΩ	-237±13.9 MΩ	533±119.2 kΩ	-70.09±12.6 MΩ
MWCNT-sugar-PDMS	6.48±0.28 kΩ	4.04±0.48 Ω	1.6±0.226 kΩ	-10.21±8.18 Ω
Neat sugar-Al-PDMS	4.05±1.06 MΩ	-204±11.77 MΩ	427±11.65 kΩ	-31.02±4.71 MΩ
MWCNT-sugar-Al-PDMS	3.2±0.24 kΩ	1.37±0.18 Ω	0.713±0.045 kΩ	-2.04±0.02 Ω

same material system, the compression specimens with electrodes on the top and bottom have an effective current cross-sectional area of ~280 mm^2 across the gauge length, which is ~3.5 times higher than the maximum cross-section area available in the tension specimens.

Since reactance measured in this study is generally negative, the following interpretation of negative reactance (capacitive reactance, X_C) in terms of overall capacitance of the system must be noted. Since, capacitance is negatively and inversely proportional to reactance, a higher magnitude negative X_C would mean the system is not very capacitive, where as a smaller magnitude negative X_C value would mean a larger capacitance at a given measurement frequency. This relation is shown in equation (**??**) where f is the input AC measurement frequency, C is the capacitance, ϵ is the dielectric constant, d is the distance between parallel plates, and X_C is the capacitive reactance.

$$X_c = -\frac{1}{2\pi fC}\ where\ C = \frac{\epsilon A}{d}\ \ (2)$$

Corresponding to the I, II and III areas demarcated in Figures 5 and 6, the tangent gauge factors for resistance and reactance are calculated for each section and material system under tension and compression and the results are presented in Table 3. Synonymous to other strain sensing devices in existence, a change in mechanical load i.e. change in the stress state, when accompanied by a change in gauge factor (GF) is indicative of strain/damage sensing [117, 119, 126, 129, 131, 131, 141].

6.3.5 Piezoresistive response under tensile loading

In the sugar-PDMS tension specimens, the side by side placement of electrodes with the mock energetic in between creates a very small capacitance (in the order of pF). Addition of micron sized aluminum particles in sugar-Al-PDMS results in the formation of localized capacitors which leads to a small increase in the overall zero-strain capacitance. However, with addition of MWCNTs to MWCNT-sugar-PDMS and MWCNT-sugar-Al-PDMS, the PDMS binder becomes near percolated as observed by the ∼3 orders of magnitude decrease in resistance in both the materials. Subsequently, it is assumed that between the two electrodes there are many conductive paths formed due to the dispersed MWCNTs. However, the MWCNTs also form localized micro-capacitors. Figure 10 illustrates the expected formations of conductive paths and micro-capacitors due to the dispersed MWCNTs in the PDMS binder and compares it with a representative parallel RC circuit. The side by side placement of the electrodes influence the measurement of reactance—the electric current prefers conductive paths over dielectric mediums and hence we get a pseudo resistor-like impedance response. (Known resistors were tested with the LCR meter used in this study and increasing positive reactance, X_L, directly proportional to increasing resistance was observed. Inductive reactance (X_L) depends on the measurement frequency f, and inductance L, of the circuit through the relation $X_L=2\pi fL$). Thus, in hybrid MWCNT-sugar-PDMS and MWCNT-sugar-Al-PDMS tension specimens, a false positive zero-strain reactance is observed which increases with more damage (a consequence of increasing resistance due to damage).

In the tension results shown in Table 3 and Figure 5a, it can be seen that for neat sugar-PDMS specimens the GF for resistance and reactance in region I is smaller as compared to regions II and III. This is believed to be a result of minor changes in electrical properties due to geometric changes in the elastic regime. During the transition from region I to II, microscopic damage begins to occur. A consequence of the onset of microscopic damage, an increase in resistance and reactance is observed. However, this is not indicative of damage sensing as this change follows a linear trend in region II and III, suggesting that the material is incapable of sensing damage as a non-linear function of applied strain in the micro/macroscale damage regime. From Table 3, it can be observed that the addition of MWCNTs to sugar-PDMS increases the resistance and reactance GF in the elastic regime by ∼2 times. This is because the inherent resistivity of the material is itself altered by addition of MWCNTs. The transition from region I to II is captured by the ∼1.3 times higher resistance GF and ∼3.2 times higher reactance GF. In Figure 5b, the scale of X axis makes the R/R response look linear. However, there is a distinct change in resistance and reactance GFs in the transition regions between I, II and III. This is indicative of good strain and damage sensing.

It has been noted that sensing due to piezoresistive MWCNT networks is best near percolation [117, 126]. Addition of conductive grains, therefore, might cause the system to be fully percolated which would then overshadow the sensing abilities of the MWCNT network. This concern was addressed by evaluating the piezoresistive response of aluminized specimens. With addition of aluminum—due to inclusion of conductive elements in the material—the overall zero-strain resistance of the material decreases and a weakly connected conductive network forms. Similar weak conductive networks due to addition of micron size metallic particles in matrix materials have been observed in other studies[113, 142, 143]. This suggests that the higher magnitude change of normalized resistance and reactance (Figure 6a) in the sugar-Al-PDMS was influenced more by the weakly connected network rather than geometric effects. Resistance and reactance GF factors for sugar-Al-PDMS show change in transition region I to II, however, there is no significant sensing in the system evident by the linear trend of resistance and reactance GFs in region II and III. In the MWCNT-sugar-Al-PDMS, normalized resistance ∼1.3 times higher than in sugar-Al-PDMS is observed in elastic region I. There is a distinct change in the resistance and reactance GFs for MWCNT-sugar-Al-PDMS in regions II and III corresponding to the mechanical loading. Compared to the sugar-Al-PDMS, the GFs for reactance are ∼1 order of magnitude higher in regions II and III. Furthermore, the resistance and reactance GFs for MWCNT-sugar-Al-PDMS are ∼2 times higher in region III than the GFs for region II. The overall change (at complete failure) in R/R and X/X is ∼3 times higher in magnitude than MWCNT-sugar-PDMS due to additional conductive aluminum particles. This indication of sensing with respect to mechanical loading demonstrates that the addition of conductive grains—despite forming weak networks—does not fully percolate the material system. Thus, even with MWCNTs and aluminum, the material remains near percolation and is a good sensing system.

6.3.6 Piezoresistive response under compressive loading

In the compression testing response shown in Figure 5c and Figure 6c for sugar-PDMS and sugar-Al-PDMS, respectively, an almost negligible change in resistance is observed. It is noted in literature that within the elastic regime, resistance decreases for a specimen in compression due to higher current penetration [144]. Within the elastic region, this decrease in resistance due to compressive geometric changes is observed in the neat and hybrid specimens and quantified via the GF. Damage however, regardless of tension or compression, causes an increase in resistance. The initial resistance GFs are positive in region I (since gauge factors are calculated with strain which is negative in compression as opposed to its positive representation as compressive strain; this signifies decreased resistance: see Figure 1c). As the effects of damage and geometric changes on resistance begin to counteract each other in regions II and III, a minimal change in resistance of neat specimens is observed evident by the very low negative resistance GFs (which can be interpreted as increase in resistance). In comparison, the zero-strain resistance values are ∼2 orders of magnitude lesser for hybrid MWCNT-sugar-PDMS and MWCNT-sugar-Al-PDMS which indicates the specimens are more conductive. In these near percolated systems, occurrence of damage (disruption of conductive paths) is accompanied with a large increase in resistance which exceeds the counteracting effects of decreasing resistance due to geometric effects. Furthermore, the inherent change in the material's resistivity also contributes to the piezoresistive change. Hence, a significant increase in normalized resistance in region II and III is observed corresponding to the mechanical loading (resistance GFs become negative and increase by ∼5-10 times at transition regions) indicating their good sensing abilities.

The mechanisms of reactance change are more complex than resistance. The overall observed capacitance of the material system is dictated by the effective dielectric constant of the material sandwiched between the conductive electrode layers and existence of localized micro-capacitors formed by conductive particle inclusions. In sugar-PDMS, there are no conductive grains, and the distance between electrodes is large leading to an extremely low capacitance observed through the higher magnitude negative reactance (Table 2; equation 2). In contrast, the inclusion of conductive MWCNTs in MWCNT-sugar-PDMS results in the formation of localized micro-capacitors (shown in

Figure 10). These localized micro-capacitors increase the overall capacitance, evident by the ∼6 order magnitude smaller zero-strain reactance (Table 2). As the compressive load increases and damage occurs in the specimen, the network of micro-capacitors is disrupted which causes a decrease in overall capacitance (Figure 5d). Reactance GFs for regions II and III demonstrate a large change corresponding to increasing damage. However, the very high negative of reactance (in the ∼MΩ range), when compared with positive resistance (in ∼kΩ range) implies that the GFs for resistance can be measured more reliably. Addition of conductive aluminum particles in sugar-Al-PDMS results in the formation of localized capacitors too—albeit they are at much higher length scales than the MWCNT micro-capacitors. The localized aluminum capacitors increase the overall zero-strain capacitance by a factor of ∼2, as compared with sugar-PDMS. Although, there is localized capacitor network, the length scale is insufficient to detect any microscopic damage. The reactance GFs for sugar-Al-PDMS in region II and III stay fairly the same and indicate that as damage occurs, the reactance remains fairly linear, indicating poor sensing abilities (Figure 6c, Table **??**). However, addition of MWCNTs to sugar-Al-PDMS creates additional networks of micro-capacitors, which decreases the overall capacitance by ∼6 orders of magnitude as compared to sugar-Al-PDMS. There is significant change in the normalized reactance corresponding to the compressive loading/damage. The reactance GFs increase by ∼1 order of magnitude for every region as the specimen undergoes the transitions between the three regions.

It must be noted that depending on the material system, either the resistance or reactance dominates the impedance (see Table 2). As such, the GFs of the dominating electrical property are more reliable measurements for a particular material system. Table **??** provides the tangent gauge factors (resistance and reactance) identified for the three regions for all material systems under tension and compression loading.

Table 6.3: Table 3: Tangent Gauge Factors for normalized resistance and reactance for the four materials systems under tension and compression. GF_R and GF_X represent the normalized resistance and reactance gauge factor, respectively.

Material System		Gauge Factor (Tension)			Gauge Factor (Compression)		
		I	II	III	I	II	III
Neat Sugar-PDMS	GF_R	2.35±0.01	6.54±0.08	6.69±0.07	1.21±0.25	-0.8±0.34	-0.6±0.74
	GF_X	1.42±0.32	5.52±1e-2	5.581±1.2	0.427±0.16	0.41±0.05	0.43±0.08
MWCNT-sugar-PDMS	GF_R	4.39±0.83	8.57±0.22	16.96±4.8	1.7±0.33	-4±1.2	-30.1±9.11
	GF_X	2.41±0.31	17.26±0.18	24.01±6.2	0.3±0.081	13.6±3.2	57.9±16.2
Neat sugar-Al-PDMS	GF_R	5.1±0.93	13.91±1.92	14.21±3.2	1.06±0.1	-0.92±0.03	-0.83±0.07
	GF_X	2.8±0.72	6.7±0.33	6.9±0.53	0.42±0.082	0.43±0.32	0.32±0.52
MWCNT-sugar-Al-PDMS	GF_R	7.1±1.13	16.3±2.14	27±1.1	1.6±0.76	-7.81±2.63	-21±5.8
	GF_X	2.6±0.73	40.2±1.3	83±4.7	2.4±0.92	28.4±5.17	151±18.9

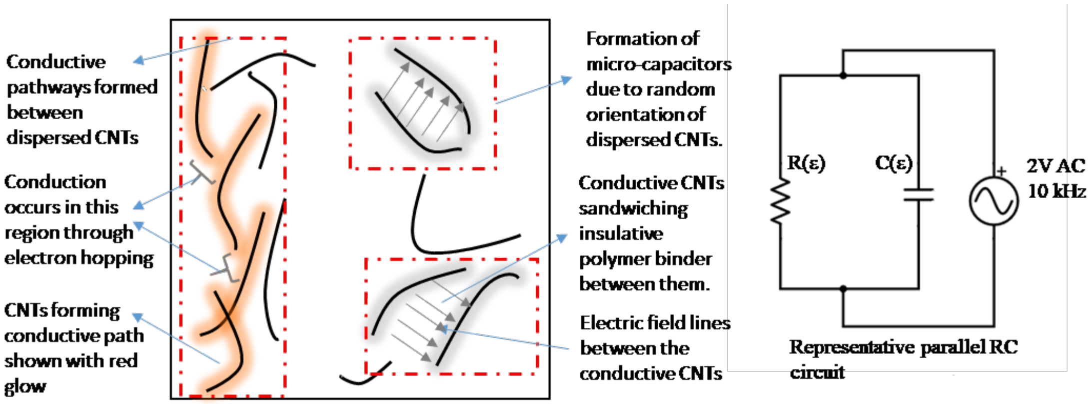

Figure 6.10: Illustration of possible formations of conductive pathways and micro-capacitors due to random distribution of MWCNTs in the PDMS binder shown along with a representative parallel RC circuit.

The resistance GFs in the elastic region I for the MWCNT specimens have a similar gauge factor range (∼2-10) as noted in other strain sensing devices; comparable to some commercial strain gauges as well [129, 130, 131, 141]. However, the highlight of MWCNT networks is its ability to sense microscale damage. Macroscale damage essentially leads to open circuits in the material systems causing a significant jump in the GFs. However, the near percolation of the polymer binder due to addition of MWCNTs causes a much higher change than observed in the neat specimens. The GFs in region I, II and III show a distinct change that accompanies strain and mechanical damage to the system, and the high gauge factors enable detection of this strain/damage with a fair degree of repeatability. The piezoresistive response quantified via the GFs strongly supports the ability of MWCNT networks to detect elastic strain, microscale and macroscale damage.

Chapter 7

Real-time damage assessment of polymer bonded energetics using nanocomposite binder phases embedded with multi-walled carbon nanotube sensing networks.

7.1 Introduction

Polymer bonded explosives/energetics (PBX/PBE) are a special class of particulate composite materials. They typically consist of two to three phases: an energetic/explosive powder phase, an ignition accelerator phase, and a binder phase. Depending on the application, several different materials (eg. HMX (Octogen), RMX (1,3,5-trinitro-1,3,5-triazine), AP (Ammonium Perchlorate)) can serve as the energetic/explosive phase [145]. Typically encountered matrix materials include epoxies, PDMS (poly-dimethylsilioxane), and HTPB (Hydroxyl-terminated polybutadiene) [145]. These materials protect the high energy, sensitive energetic/explosive phase by absorbing some mechanical stimuli but their primary function is to allow fabrication of complicated structural geometries and cross-sections which have tremendous operational significance [145, 146, 147]. For instance, by varying the cross-section across the length in solid rocket propellant motors (which is an application of PBEs) the amount of thrust produced by the motor can be controlled [147]. However, these materials generally tend to be very sensitive to mechanical stimuli. There are great risks associated with this material class in terms of material handling, where accidental detonation, and abrupt behavior during operation can result is serious consequences, and in the worst case, even loss of human life. The performance assurance, and safety of these materials, in the purview of their application, depends partly on the structural integrity of the polymer bonded energetics [148, 149]. Mechanical damage events such as crystal fracture, excessive debonding between crystal and binder, sagging due to creep, and binder fatigue can result in accidental detonation, uneven thrust distribution or combustion, and inefficient operation performance [148, 149]. In addition to mechanically induced damage, PBEs are exposed to vibrations and impact loads during transportation, and thermal loads due to environmental conditions [149, 150, 151]. The service life of PBE/PBX materials tends to be very large, oftentimes amounting to several decades [148, 152]. As such, it becomes very important to monitor the structural integrity of these PBE materials.

Current methods for assessing the presence of damage and cracks involve the use of non-destructive testing (NDT) techniques such as X-ray scanning, and ultrasound imaging in combination with conventional techniques like mounted external strain-gauges [153]. X-ray scanning is a fast method by which cracks and irregularities in the material can be detected[153]. It involves exposing the material to high-energy photons that pass through or are absorbed by the material [153]. Differences in the material density, molecular structure, and X-ray absorption capacity result in observable differences when the emitted X-rays are collected and analyzed [153]. *A priori* knowledge of the behavior of individual constituents under X-ray exposure can help identify material phases, irregularities, as well as cracks and damage (since cracks are phases where material density is drastically lower than the surrounding material) [154]. While X-ray scanning allows adequate damage assessment by providing a view of the internal structure of the material, its several drawbacks include radiation exposure, lack of depth perception in the micro-structure, poor resolution/contrast for similar material densities, and the associated downtime required for assessment [153]. Another method commonly used is ultrasound scanning wherein the high-frequency vibrations are emitted into the material via direct contact and the reflected waves are monitored to recreate the internal material structure [153]. Differences in material densities, irregularities, and degree of damping provided by the phases cause different degrees of reflection intensities which can be interpreted to analyze micro-structures [152, 153]. Typically, ultrasound techniques work well with the detection of delamination; however, it can be difficult to achieve significant depth penetration if metal-propellant boundaries are present within the PBE [153]. The application of high-frequency waves during ultrasound may lead to hotspot creation, which results in thermal load-induced stress and may severely inhibit operational performance or may lead to accidental detonation as well [155]. To address this issue, newer techniques involve the use of low-frequency vibrations which rely on different resonant frequencies of the constituent materials [156]. The response frequencies from a material can be isolated using methods such as fast Fourier transform, and the composition of the material can be determined [156]. However, this method struggles with highly heterogeneous materials, particularly PBEs/PBXs which have several phases consisting of particulate distributions [156]. As such, more innovative methods are needed to assess damage in PBEs.

Given the mechanical sensitivity of the PBE materials, an approach that relies on monitoring the non-mechanical properties of the material may be advantages. A solution can be found in approaches that exploit the change in electrical properties of material upon mechanical stimuli; such mechanisms involve the use of piezoelectric or piezoresistive sensors embedded within the polymeric matrix material [97, 157]. Previous works by Shirodkar et al. and Sengezer et al. have investigated the application of multi-walled carbon nanotube (MWCNT) networks embedded in elastomeric and rigid polymeric matrix materials of mock PBEs [97, 157, 158]. The mock PBEs utilized sugar crystals as a substitute for high-energy particulates like AP, HMX, and RDX. MWCNTs were dispersed in the polymeric binder, which was then used to fabricate the PBE materials, thus embedding MWCNT networks throughout the PBE material. The sample fabricated thereafter underwent mechanical testing in conjunction with monitoring of electrical resistance. The main challenges in implementing such a method for PBEs were the low binder concentration, high degree of heterogeneity in the microstructure, and the presence of conductive/non-conductive phases in the particulate mixture. These factors were believed to have the potential to inhibit MWCNT networks to form conductive pathways, and by extension, prevent any sensing capability. As preliminary proof-of-concept studies, these works established the viability of achieving substantial change in the electrical resistance of the nanocomposite PBE materials as a response to strain, microscale damage (invisible cracks), and macroscale damage (visible cracks) evolution. This current work extends these studies to evaluate the applicability of MWCNT networks as vehicles for structural health monitoring (SHM) in polymer bonded energetics. These materials will incorporate Ammonium Perchlorate (AP) crystals as the oxidizer energetic phase, Aluminum powder as the metallic fuel, and Polydimethylsiloxane (PDMS) as the polymer binder, together which will constitute a PBE. The experimental evaluation will focus on investigating the effects of each constituent on the overall sensing ability of the MWCNT network. As such, SHM capabilities of MWCNT/PDMS (nBinder) materials are first evaluated to study the binder's electromechanical response, followed by

AP/MWCNT/PDMS (nPBE) to assess the impact of AP addition, and finally, AP/AL/MWCNT/PDMS (nPBE-AL) to evaluate the impact of adding conductive grains such as aluminum. ASTM D695 based compression samples were prepared and monotonic compression tests were conducted in conjunction with electrical resistance monitoring. Change in resistance as a response to applied strain was quantified via gauge factors. Electrical behavior was studied with respect to the mechanical behavior and the resulting findings have been presented in this work.

7.2 Methodology

7.2.1 Materials

The Polymer bonded energetic (PBE) samples fabricated in this study were prepared with Ammonium Perchlorate (AP) powder, NH_4ClO_4, which served as the oxidizer component of the energetic particulate matter. The AP powder has an average particle size of ∼200 μm, as reported by the manufacturer [157]. Aluminum powder was used as a metallic fuel; a mixture of AP and aluminum powder results in a potent energetic particulate mixture and is commonly used as a solid rocket propellant [97]. The average particle size of the aluminum powder was reported as ∼30 μm by the supplier (Pyro Chemicals). Images acquired via scanning electron microscopy (SEM) showing the particle size distribution of the two particulate powders are presented in Figure 7.1a and 7.1b. Polydimethylsiloxane (PDMS), supplied by Dow Chemicals *(Sylgard 184)*, is a two-part silicone-based elastomer which was used as the polymer binder. Research grade (SKU: 030103) Multi-walled carbon nanotubes (MWCNTs), purchased from Cheap Tubes Inc, were used as nanofillers to prepare the nanocomposite PBE (nPBE) samples. The MWCNTs have a reported purity of greater than 95% and have the following dimensions: outer diameter = 10 to 20 nm, inner diameter = 3 to 5 nm, length = 10 to 30 μm.

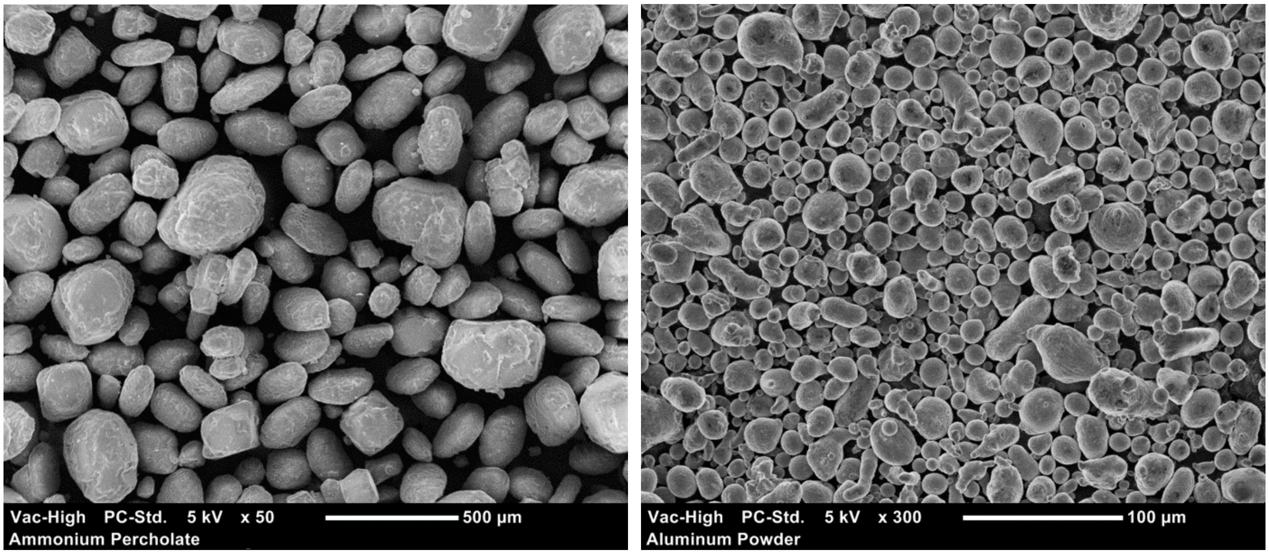

(a) Particle size distribution of Ammonium Perchlorate (AP) crystals

(b) Particle size distribution of Aluminum powder used in this study

Figure 7.1: Scanning Electron Microscope (SEM) images of the energetic particulate powders used in this study, showing the distribution of the particle sizes.

7.2.2 Fabrication of Polymer Bonded Energetics

The neat samples, i.e. samples without any MWCNTs dispersed in the polymer binder, were fabricated as follows. PDMS Part A and Part B were mechanically mixed in a 10:1 ratio (by weight). Measured quantities of particulate powders were added to the PDMS according to the desired ratio of particulate to binder—A particulate composition consisting of only AP resulted in PBE samples, whereas particulate compositions consisting of AP and aluminum powder resulted in PBE-Al samples[1]. The mixture was then degassed for 30 minutes in a vacuum chamber under a 90 kPa vacuum pressure. Aluminum molds prepared according to

---

[1] The samples with only AP in the particulate composition will be referred to as PBE samples, and samples with AP and aluminum will be referred to as PBE-Al samples hereafter in this study for brevity.

ASTM standards (ASTM D695: Long Compression samples) were prepared by applying a thin coat of mold release agent (Mann Release 200). The degassed mixture was then pressed into the molds and degassed for another 20 minutes using the same parameters to remove any remaining entrapped air. The pressed molds were cured at 135°C for 60 minutes in an oven (MTI DZF-6020-HT). The molds were allowed to cool to room temperature after which the long compression samples (ASTM D695) were extracted by hand.

The nanocomposite samples (nPBE, and nPBE-AL)[2], i.e. samples with MWCNTs dispersed in the polymer binder, were fabricated as follows. Required quantities of MWCNTs were measured as per the desired weight concentration, relative to the weight of PDMS. Acetone, equal in weight to the weight of PDMS Part A, was added to the measured MWCNTs and mixed thoroughly using a magnetic stirrer for 5 minutes at 400 rpm. Being a low viscosity solvent, acetone aids in the proper dispersion of the MWCNTs. The MWCNTs were dispersed in the acetone using an ice-water bath sonication (QSonica 500A) with a 20 kHz frequency and 30% amplitude for 1 hour. After the first sonication round, measured quantities of PDMS Part A were added to the acetone-MWCNT and mixed for 10 minutes at 400 rpm using a magnetic stirrer. The PDMS(Part A)-acetone-MWCNTs mixture was then sonicated for another hour using the same parameters. After dispersion, the acetone was extracted from the mixture using a rotary evaporator (IKA RV10 Rotary Evaporator) for 90 minutes using a 75 degree Celsius water bath. PDMS Part B was then added to the PDMS(Part A)-MWCNTs mixture obtained after acetone extraction and was mixed thoroughly by hand for 5 minutes. Required quantities of the binder were then collected in a glass beaker. Measured quantities of particulate powders, as required for the different compositions, were then added to the MWCNT-PDMS mixture and mixed by hand for 10 minutes. Subsequent processes for degassing, mold pressing, curing and sample extraction

---

[2] The samples containing multi-walled carbon nanotubes are indicated with the prefix ”n” applied to the PBE or PBE-Al abbreviation.

were the same for the nanocomposite and neat samples.

In addition to the neat and nanocomposite samples, a batch of samples containing just the binder and MWCNTs (referred to as the neat binder and nanocomposite binder ”nBinder” samples), with varying concentrations of MWCNTs, were also prepared to study the mechanical and electrical behavior of the binder and MWCNTs, without the influence of particulate matter. The fabrication process for these samples was consistent with that of the neat and nanocomposite samples; the exception being the addition of particulate powders to the mixture.

Table 7.1 highlights the materials test matrix, i.e. all the materials investigated in this study. Figure 7.2 shows photographs of the long compression samples for some of the materials mentioned in Table 7.1.

Table 7.1: Material compositions of all the material systems fabricated in this study.

Material	Particulate	Particulate	Binder	Nanoparticle
-	*% total wt*	*% total wt*	*% total wt*	*% wt of binder*
-	*Ammonium Perchlorate*	*Aluminum Powder*	*PDMS*	*MWCNTs*
Neat Binder	-	-	100	-
0.8% nBinder	-	-	99.5	0.8
1% nBinder	-	-	99.2	1
2% nBinder	-	-	99	2
Neat PBE	80	-	20	-
1% nPBE	80	-	19	1
2% nPBE	80	-	18	2
Neat PBE-AL	64	16	20	-
2% nPBE-AL	64	16	18	2

7.2.3 Mechanical Testing

Monotonic compression tests were conducted according to ASTM D695 in an Instron double-column universal testing machine (5900 series) using compression plate fixtures and a 5 kN

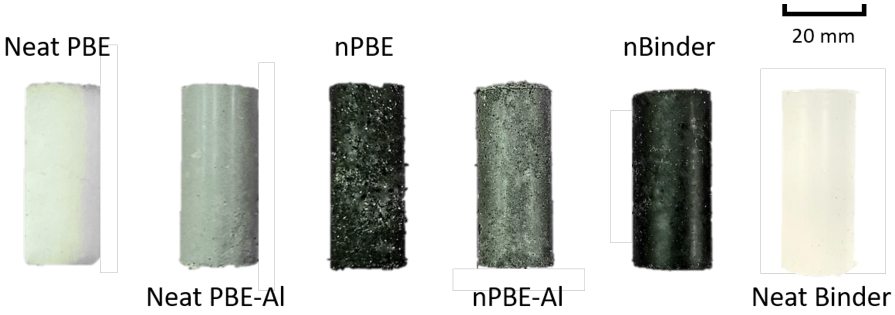

Figure 7.2: Photographs showing long compression samples of neat Binder, nBinder, neat PBE, nPBE, PBE-Al, and nPBE-Al. As a representation, only one MWCNT weight concentration for nBinder, nPBE and nPBE-Al material systems is shown.

load cell. A pre-load of 2 N was applied to ensure complete contact of the sample with the fixture plates. The test was conducted as a displacement controlled test with a displacement rate of 5 mm/min. Load and displacement data was recorded for each test. A total of four samples for each material system were tested. Compressive modulus and compressive strength were calculated for each sample of each material system.

7.2.4 Sample Preparation for Electrical Characterization

The cured compression samples were first sanded down face-wise using a belt sander (fine grit) such that all the samples had similar nominal lengths of 40 mm. A flat surface was ensured after the sanding operation. Sanding also led to a smooth surface enabling proper electrode attachment. A thin coat of high conductive silver epoxy (MG Chemicals 8330) was applied on both faces of the long compression sample to minimize contact resistance. The exposed end of a stripped 30 gauge copper-tin wire was then glued on both the faces of the sample using a drop of conductive paint (Bare conductive Paint). The electrode wires were then secured on the sample using electrical tape and the silver epoxy and conductive paint were allowed to fully cure for 24 hours. Figure 7.3 shows a PBE compression sample with the electrodes attached. The electrical tape used to secure the wires was carefully removed just before testing, thus preventing any accidental damage to the electrodes before testing.

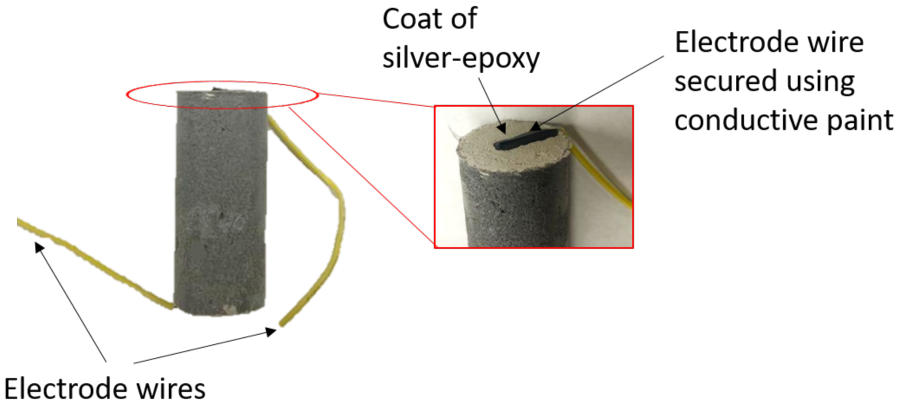

Figure 7.3: A Neat nPBE-Al compression sample with two electrodes attached to the top and bottom faces. (Inset) Detailed view of the electrode. Electrodes were placed on both faces (top and bottom) of the compression sample.

7.2.5 Electrical Characterization and Electro-mechanical Testing

In this study, all the electrical data was acquired via an LCR meter (Agilent E4980) using a two-point measurement system, similar to previous works [97, 98, 99, 159, 160]. The electrical data, resistance, and reactance, was acquired using a 2 Volt AC signal with a measurement frequency of 100 kHz[3]. To evaluate the piezoresistive response, only the acquired resistance data was used. Equation 7.1 shows the formula for resistance, which involves material resistivity as well as the sample geometry parameters.

$$R = \rho \frac{L}{A} \tag{7.1}$$

where R is the resistance (in Ohms), L is the length of the conductor, A is the cross-section area of the conductor, and ρ is the material resistivity.

---

[3] A frequency sweep was performed on the samples and it was observed that at frequencies of 100 kHz and higher, the electrical measurements were frequency independent and hence 100 kHz was selected as the measurement frequency.

The base electrical properties of all the fabricated compression samples (referred to as the ”unstrained electrical properties”) were measured under zero mechanical strain before electro-mechanical testing. The electrical data was gathered for 30 seconds and the average resistance was subsequently calculated from the resulting data set. Electrical data was also gathered during mechanical testing to observe changes in electrical properties as a function of strain. The samples were carefully placed between two electrically insulated compression plate fixtures, which were insulated using electrical tape and wooden chips. The open ends of the attached electrodes were then connected to the LCR meter test leads. The compression plates were then lowered to apply a pre-load of 2 N on the sample, thus also firmly pressing down on the electrode contacts attached to the samples. Due to the placement of the electrodes on the top and bottom faces of the sample, the length of the sample is equivalent to the electrical gauge length. The resistance data was then acquired in conjunction with the mechanical test. Gauge factors (GF) were calculated for each sample of each material system to quantify the change in electrical properties as a function of applied strain. Equation 7.2 shows the formula used to calculate gauge factors, which is defined as the change in normalized resistance upon strain.

$$GF = \frac{\Delta R/R_o}{\varepsilon} \tag{7.2}$$

where $\Delta R/R_o$ is the change in normalized resistance (change in resistance relative to initial resistance upon initial resistance) and ε is the mechanical strain.

7.3 Results and Discussion

7.3.1 Mechanical Properties

Figures 7.4a, 7.4b, and 7.4c show the compressive stress-strain curves obtained for all the materials tested in this study. The solid lines indicate the mean stress-strain curves, whereas the shaded regions corresponding with every solid line show the variation in the data, representing two standard deviations. Figures 7.5a, 7.5b, and 7.5c show the reduced mechanical data for compressive modulus, strength, and compressive strain at peak stress presented in the column chart format, where the columns indicate the mean value and the error bars indicate a variation of one standard deviation. It can be observed in Figure 7.4a that the nanocomposite binder samples exhibit an initial linear region, followed by strain hardening behavior until the end-of-test. Rather than sample rupture or failure, the elastomeric binder samples buckled and slipped out of the grips[4] resulting in abrupt load drops seen in the stress-strain curves at higher strains. The test was stopped and the load-displacement was not recorded after the occurrence of such an event. The 1% and 2% nBinder samples exhibited statistically similar[5] compressive modulus compared with the neat binder, all lying in the range of 2.5-3 MPa. Similar compressive modulus and variations have been observed in other works exploring MWCNT/PDMS composites [161, 162, 163, 164]. The 0.8% nBinder samples showed a slight reduction in the modulus, with an average value of ∼1.56 MPa. The increased compliance in the 0.8% samples can be attributed to the presence of voids underneath the sample faces, which were an artifact of experimental error during degassing[6]. The compressive strengths for the nBinder samples

---

[4] To avoid constraining Poisson's expansion of the sample in the lateral direction due to longitudinal compression, the fixture grips were greased thus allowing sliding of the sample faces.

[5] statistically similar implies that the modulus mean values lied between one standard deviation of the reference mean value.

[6] These voids were discovered post-testing by cutting through all the samples.

were statistically similar to the neat binder and varied between 1-7 MPa. While the results for compressive strength are presented for the nBinder samples, they do not represent actual compressive strength since the samples do not actually fail, but rather slip out of the grips, as discussed earlier. As a consequence, there is significant variation in the data and hence the error bars in the compression strength data for the nBinder samples are very large (approximately +/- 80% of the mean). Similarly, the strain at peak stress presented in Figure 7.5c, which is a value related to the compressive strength, also has no physical meaning as a material property; but is a consequence of sample slippage out of the grips.

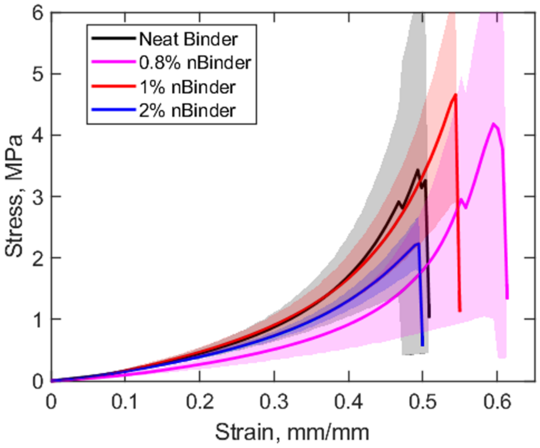

(a) nBinder Samples (MWCNT/PDMS)

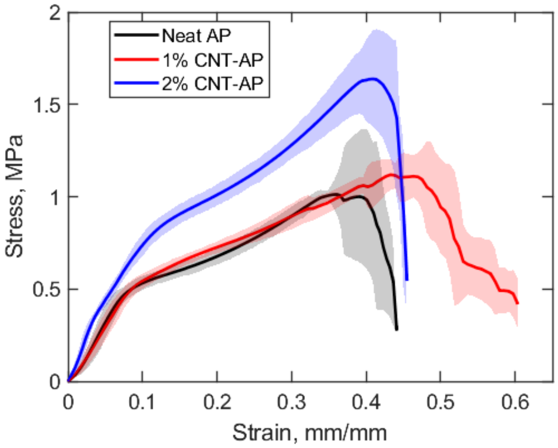

(b) nPBE Samples (MWCNT/PDMS + AP crystals)

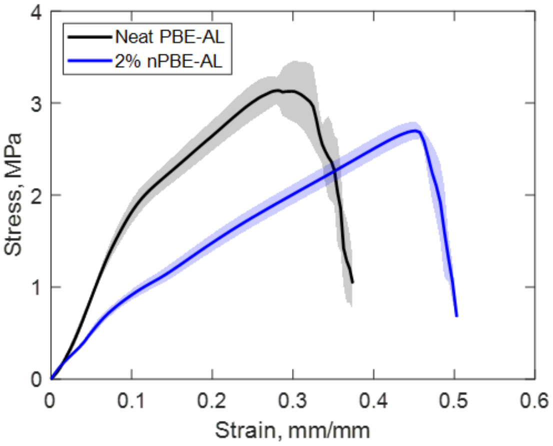

(c) nPBE-AL Samples (MWCNT/PDMS + AP crystals + Aluminum powder)

Figure 7.4: Compression Stress-Strain curves for all the material systems tested in this study. Neat samples which serve as the baseline samples for each sub-category (nBinder, nPBE and nPBE-AL) are shown with a black solid line. The shaded regions indicate the variation in the data representing two standard deviations.

It can be observed from Figure 7.4b, that the mechanical behavior exhibited by the nPBE samples differs significantly from that observed in the nBinder samples. While the nBinder samples only consist of PDMS/MWCNTs, the nPBE samples have 80% particulate matter by composition, and only 20% binder. This significantly affects the elastic response of the material, indicated by the small linear region of the nPBE stress-strain curves. After the linear region, an elbow can be observed proceeded by strain hardening and ultimately, sample failure through macroscale damage. As indicated by the overall increase in compressive modulus, the stiffness values for nPBE samples are ∼4 times higher compared to the nBinder samples. This increase can be attributed to the addition of stiffer AP crystals and MWCNTs. The 2% nPBE and the 1% nPBE samples exhibited a statistically similar compressive modulus compared to the neat PBE. Comparing the compressive strength, the 2% nPBE samples exhibited a ∼50% increase compared to the neat PBE samples. As seen in Figure 7.5c, the strain at peak stress is statistically similar for all nPBE samples compared with the neat PBE samples.

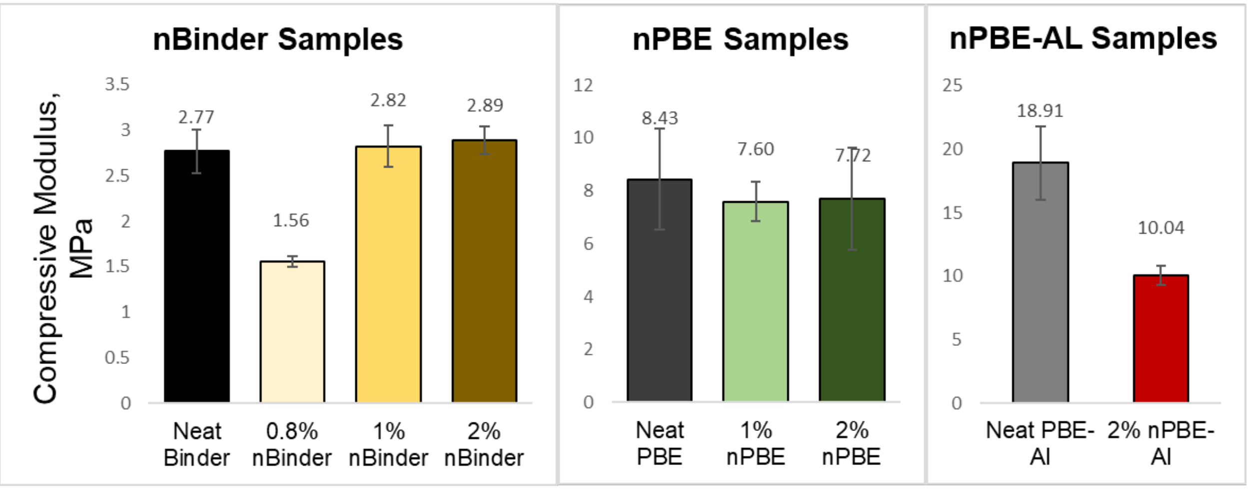

(a) Compressive Modulus, MPa

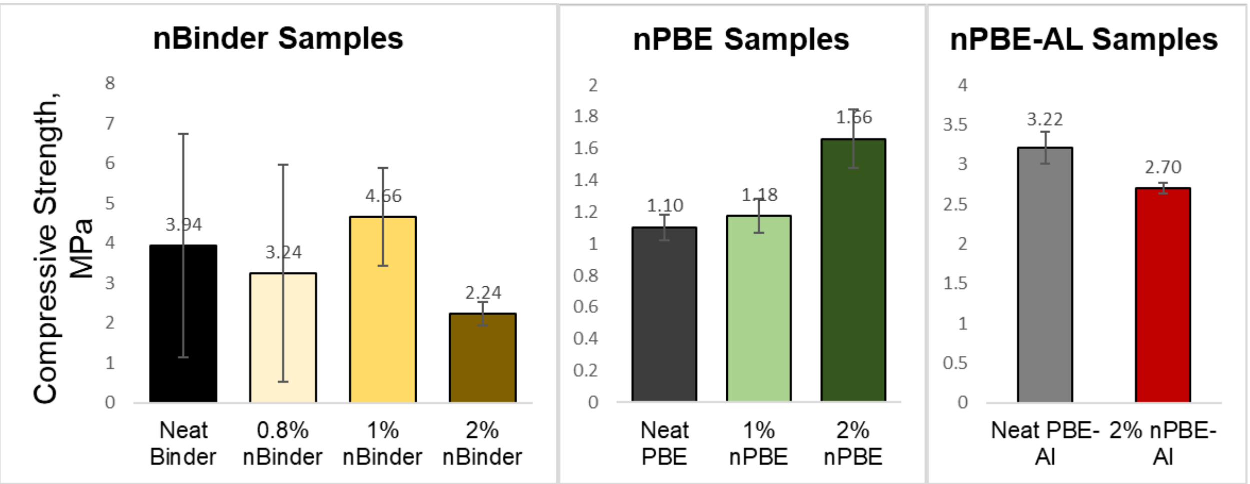

(b) Compressive Strength, MPa

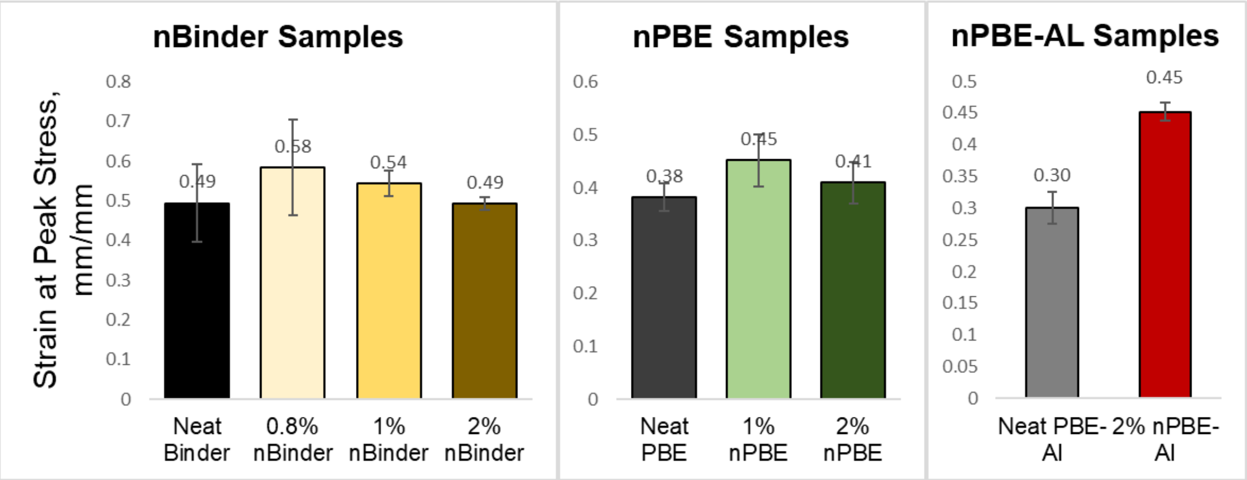

(c) Strain at Peak Stress, mm/mm

Figure 7.5: The average values for compressive modulus, compressive strength and strain at peak compressive stress are shown for all the materials tested in this study. Error bars indicate the variation in the data representing one standard deviation.

Palmer et al. [146] explored the material properties of several PBE compositions of binders and particulate crystal sizes via Brazilian disk tests to determine tensile strength. It was found that the primary mechanisms of damage in PBEs with rubbery elastomers as binders were debonding, binder void formation, and void expansion [146]. X-ray tomography performed by Palmer et al in their experiments shows no obvious crystal fracture in AP, proving that debonding dominated the modes of failure [146]. Evidence of similar behavior can be observed in the mechanical failure analysis of the samples tested in the present study. Figure 7.6a shows an SEM image of the fracture surface of a neat PBE sample where examples of particle-binder debonding, and matrix cracking/rupture can be seen. In the present study, the AP crystals are not chemically bonded to the PDMS binder but are rather shrunk fit due to curing contraction and weak van der Waals forces [97]. As a result, weak interfaces are formed between the AP grains and the binder which results in widely visible crystal-binder debonding throughout the fracture surface leading to it being deemed the primary mechanism for failure, followed by matrix rupture as the second most dominant failure mechanism.

Figure 7.4c shows the stress-strain curves obtained for the aluminized AP-based PBEs, namely PBE-AL and 2% nPBE-AL. Compared to the size of the AP crystals, the 1/6th smaller particle size of the Aluminum powder results in a bi-modal particulate distribution, leading to a higher particulate packing efficiency in the Aluminized PBE samples. The higher packing of stiff phases improves the load transfer through the material, thus resulting in a more stiff material compared to PBE samples. The neat PBE-AL samples exhibited an average compressive modulus of 18.91 MPa, which is ∼2 times higher than the neat PBE samples. Improvements in the compressive strength were also observed, with the neat PBE-AL samples exhibiting compressive strengths ∼3 times higher than the neat PBE samples. As a result of the increased stiffness, the strain-to-failure observed in the neat PBE-Al samples decreased to an average value of 0.3, compared to the ∼0.38 observed for the neat PBE samples. A decrease in the compressive modulus of 2% nPBE-AL samples (10.04 MPa) was observed compared to the neat PBE-AL samples (18.91 MPa). However, the modulus values for 2% nPBE-AL were still greater compared to the 2% nPBE samples, indicating the contribution of the Aluminum powder in the overall properties of the bulk material. While a slight decrease in modulus can be observed upon the addition of MWCNTs in the PBE samples as well, it is believed that differences in compaction of the aluminized PBE samples during fabrication may have resulted in more pronounced differences in the modulus. The average compressive strength of the 2% PBE-AL (2.70 MPa) was slightly lower than neat PBE-AL (3.22 MPa). As a result of the differences in the modulus, the strain-to-failure of the 2% nPBE-AL samples (0.45) was greater than the neat PBE-AL samples (0.30). Upon inspection of the failure modes of the two aluminized PBE materials, distinct behaviors were observed. The neat PBE-AL samples exhibited a shear-dominated failure, failing through an inclined plane under compression. However, the nPBE-AL samples exhibited a central crack propagating through the middle of the sample, indicating tensile-dominated failure due to bulging under compression. Such failure modes, driven by tensile failure, commonly occur in particulate materials and ceramics, where the material's tensile strength is less than its compressive strength [165, 166].

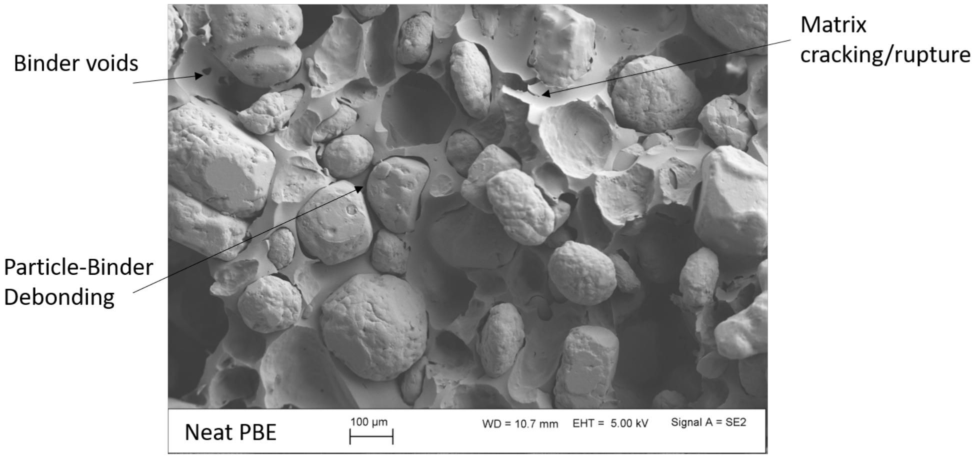

(a) Neat PBE sample

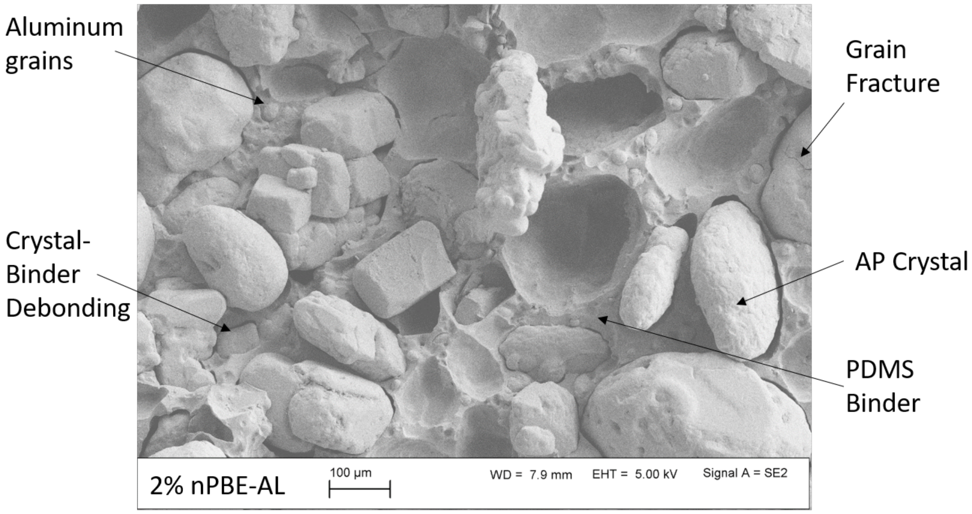

(b) Neat PBE-AL sample

Figure 7.6: SEM images of the fracture surfaces of neat PBE, and neat PBE-AL samples showing examples of the various failure mechanisms observed. Similar surface features and topographies were observed in all the nPBE and nPBE-AL samples.

7.3.2 Strain Sensing in nanocomposite binder samples (PDMS based nBinder samples)

In conjunction with the mechanical testing, the electrical data was monitored for the samples to establish the electro-mechanical sensing capabilities of the nBinder samples. Before the samples could be tested under mechanical strain, it is important to know the base resistance value of every sample under no strain. To that effect, the unstrained resistance values for every sample of every material system were calculated by collecting ∼200 independent electrical readings while the sample was subjected to zero strain, and then the data was averaged. Table 7.2 presents the unstrained resistance values for all the material systems explored in this study. To identify the acceptable level of variation in the electrical resistance readings, the variance-to-mean ratios (a.k.a index of dispersion) were also calculated from the unstrained resistance data. The VMRs indicate the reliability of the measured electrical signals; if the VMR<1 then the electrical readings are considered to be under-dispersed, meaning that there is very less variation in the measured value and hence the signal is deemed accurate and reliable[7]. Table 7.2 presents the unstrained VMRs calculated for every material system explored in this study.

It can be observed that the base resistance values of the nBinder samples decrease with the addition of MWCNTs. The neat binder, as expected, exhibited the highest base resistance of ∼450.92 kΩ while the 2% nBinder samples exhibited the lowest value at ∼23.48 kΩ. The change in the base resistance values also provides an idea of the percolation concentration of the MWCNTs in the binder. As can be seen in Figure 7.7, the weight concentrations above 1% can be taken to be at or near percolation. This value is very sensitive to the dispersion of the MWCNTs and the type of CNTS used as well. Several works in the literature provide the the percolation thresholds for PDMS/MWCNT materials, and it has been observed that

---

[7] The variance to mean ratio (VMR) is a simple tool through which the dispersion of a probability distribution can be quantified. The VMR, also referred to as the ”index of dispersion”, is equal to zero when the measured value is constant. It is exactly equal to 1 in a perfect Poisson distribution. If the VMR is >1 then the distribution is deemed to be overdispersed, whereas if the VMR is between zero and 1, then the distribution is deemed to be under-dispersed. In the purview of the electrical-mechanical sensing work presented in this work, the VMR shall be applied to quantify the dispersion of the electrical reading taken for a particular sample at a particular strain level. If the VMR is lesser than 1, the electrical readings will be considered to be stable and reliable, implying that the electrical data gathered for that sample, can be used to characterize material behavior.

the percolation threshold can vary between 0.5-10% [97, 98, 99, 161, 167, 168, 169, 170, 171, 172, 173].

The VMRs calculated for the nBinder samples decrease with increasing MWCNT concentration. The average VMRs for 1% and 2% nBinder samples were calculated as 0.12 and 0.5×10^{-5}, respectively, both of which are well below the threshold value of 1. Thus the 1% and 2% nBinder samples exhibit reliable electrical readings and are considered for further detailed analysis.

Table 7.2: Unstrained base resistance values and associated variance-to-mean ratios calculated for all the material systems considered in this study

Material	Unstrained Resistance	Unstrained Variance-mean Ratio
-	*kilo-Ohms, kΩ*	*VMR*
Neat Binder	450.92±47.35	6.10±3.9
0.8% nBinder	40.29±15.10	1.31±0.7
1% nBinder	27.75±15.06	0.12±0.05
2% nBinder	23.48±4.02	$(0.5 \pm 0.4) \times 10^{-5}$
Neat PBE	1429.36±481.90	18.26±4.98
1% nPBE	68.72±14.35	$(1.15 \pm 0.59) \times 10^{-5}$
2% nPBE	12.81±1.92	$(0.91 \pm 0.16) \times 10^{-5}$
Neat PBE-AL	63.26±18.06	$(0.57 \pm 0.19) \times 10^{-4}$
2% nPBE-AL	3.49±0.53	$(0.22 \pm 0.13) \times 10^{-9}$

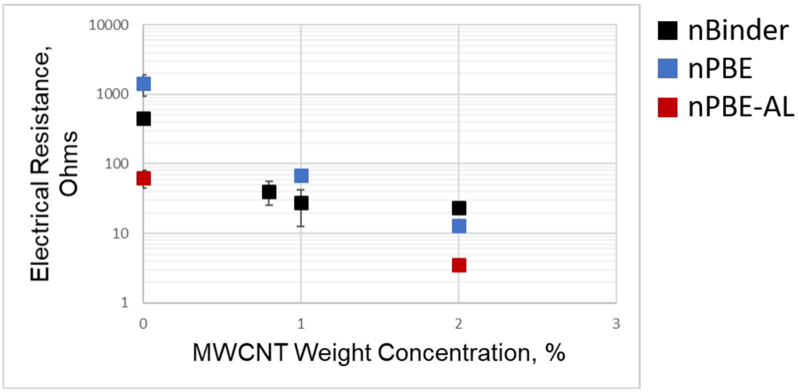

Figure 7.7: Variation of the base electrical resistance as a function of the MWCNT weight concentration for all the material systems explored in this study.

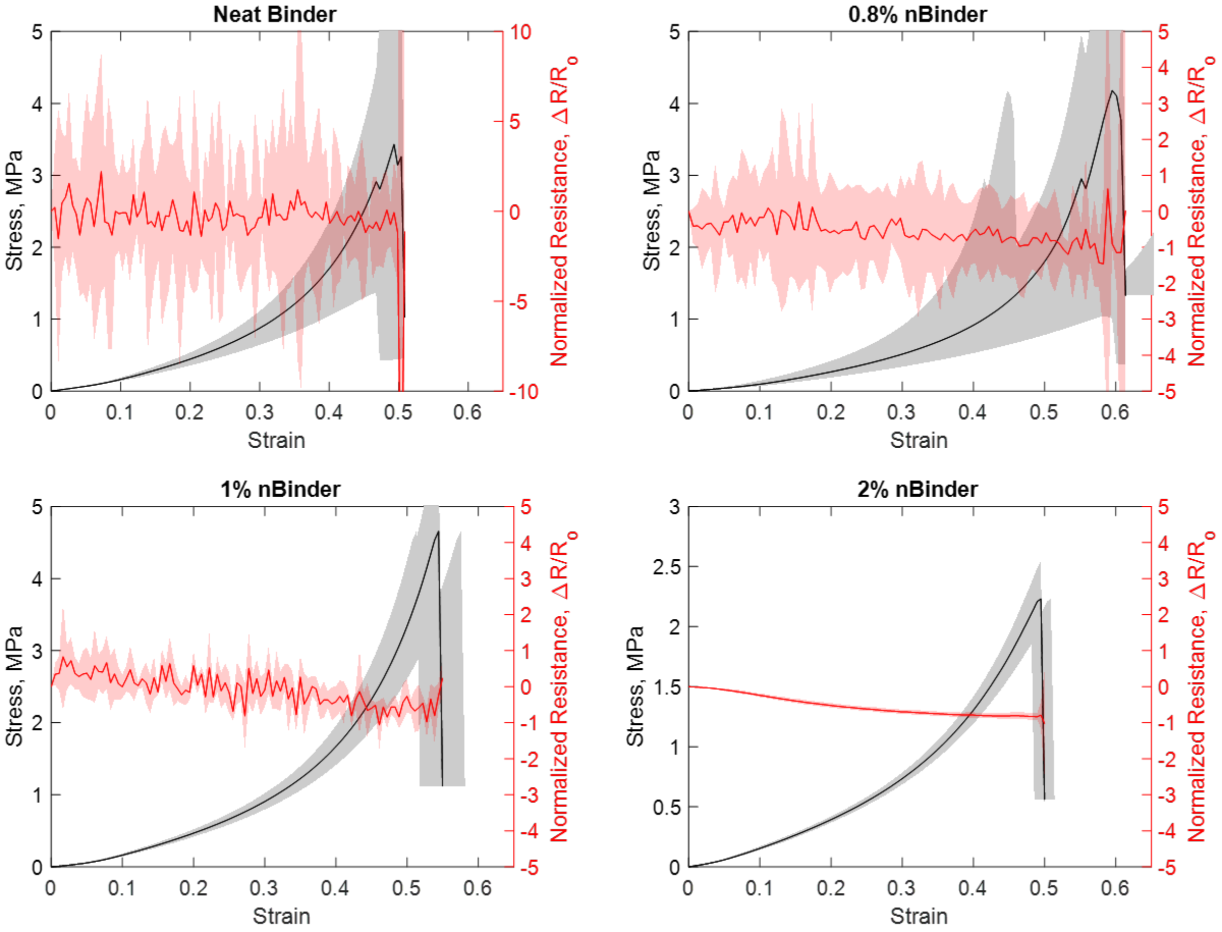

Figure 7.8: Change in normalized resistance as a function of strain plotted in conjunction with the stress-strain curve for the neat binder and nBinder samples. The solid lines represent the average value, while the shaded regions represent the variation in the data.

Figure 7.8 shows the change in normalized resistance as a function of mechanical strain, plotted in conjunction with the stress-strain curve for neat binder, 0.8%, 1%, and 2% nBinder samples. The solid line represents the mean curve while the shaded region indicates the variation. As indicated by the unstrained VMR for neat binder and 0.8% nBinder, electrical resistance data has far too much variation to be able to see any definitive trends for the normalized change in resistance curve. At 1% MWCNT concentration, the signal variation reduces drastically compared to the 0.8% nBinder. A rough trend can be observed where the resistance value seems to be decreasing, however, the signal noise prevents a confident assessment of the electro-mechanical sensing behavior. At 2%, the MWCNT weight concentration is well above the percolation threshold, and that can be observed by the reduction in the signal noise, as well as improvements in the signal quality. A definitive decreasing trend can be observed, where the resistance decreases with increasing strain. Figure 7.9 show the electro-mechanical behavior of the 2% nBinder samples in more detail. The decrease in resistance as a response to an increase in strain can be clearly seen. This is the expected behavior for strain sensing during compression, as can bee seen in the theoretical model shown in Figure 7.9(b)[8]. As the sample undergoes compression, the length, L decreases, and the cross-section area, A increases due to Poisson's ratio of the material; since resistance is proportional to the geometric factor, L/A, the overall resistance decreases during compression. The nBinder samples behave very much like elastomers and hence, damage is not expected; the decreasing resistance values further confirm this. The tangent gauge factors for the 2% nBinder samples calculated for the three regions of interest shown in Figure 7.9(b-d) are listed in Table 7.3. At strains lesser than 30% where the stress-strain response is fairly linear, the gauge factors obtained are comparable with those obtained for conventional metal strain gauges which are typically around 2 [174]. It can be observed from the gauge factor that at 2% MWCNT weight concentration, the MWCNT network lends the PDMS binder good electro-mechanical sensing ability. Consequently, for the more complex material compositions explored in this study, later on, the 2% MWCNT weight concentrations will be studied in more detail.

---

[8] Additional information about the theoretical models is presented in Appendix D

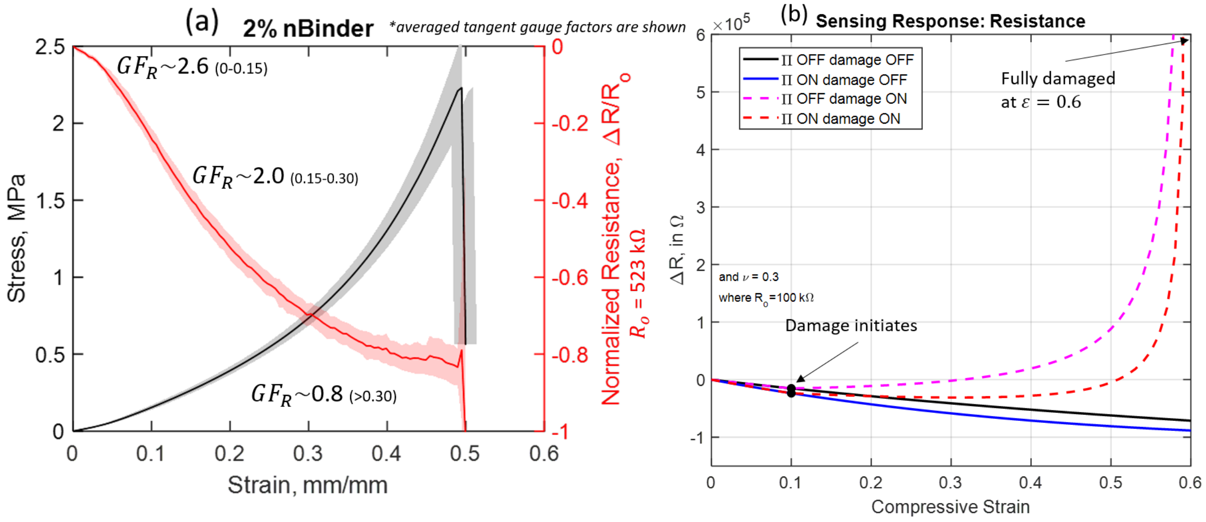

Figure 7.9: (a) The electromechanical response of 2% nBinder samples. (b) Theoretical model showing the behavior of a homogeneous solid under strain and subsequent damage. Detailed information about the theoretical models are presented in Appendix D.

Table 7.3: Average tangent gauge factors (GF) calculated for the materials systems exhibiting electromechanical sensing behavior. The negative value of GFs indicate the inverse relation of resistance with strain, i.e. decreasing resistance with increasing strain or vice-versa. The positive value of GF indicates a direct relation between resistance and applied strain.

Material	Strain Range	Gauge Factor
-	%	*GF*
2% nBinder	0-15	-2.76
	15-30	-2.03
	30-45	-0.84
2% nPBE	0-5	10
	5-15	17.7
	15-40	6.7
2% nPBE-AL	0-5	19
	5-15	22.4
	15-40	5.1

Discussion on origins of piezoresistive electrical sensing for MWCNT/PDMS nanocomposite binders

For a nanocomposite binder with embedded MWCNT networks, macroscale resistance change is driven by the following factors: geometric effect (changes in the L/A ratio in Equation 7.1), formation and disruption of conductive pathways in the MWCNT network, and inherent MWCNT piezoresistivity [157, 158, 175, 176, 177, 178, 179, 180]. The formation and disruption of conductive pathways are very dependent on the MWCNT weight concentration and quality of dispersion. A simplified explanation is provided next. A very high concentration of MWCNTs would result in a very well-connected MWCNT network. However, this is undesirable as the MWCNT network would not be very sensitive to mechanical stimuli owing to the presence of an excessively connected network, which will be difficult to disrupt without significant material damage. A very low concentration would also impede sensing as there will be very few instances of connected conductive pathways if any. Thus the ideal concentration and dispersion would be such, where the MWCNTs are adequately connected [97, 167, 168, 169, 171, 173]; when such a condition is met, the MWCNT network is referred to as a percolated network of MWCNTs. With a percolated network, small strains cause large changes in resistance, owing to the changes in the connectivity of the MWCNT network. This mechanism is the primary driver of macroscale resistance change in MWCNT/PDMS samples [177, 178]. Figures 7.10b and 7.10a show SEM images of the MWCNTs distributed in the PDMS binder phase of nPBE-AL and nPBE samples, respectively. These MWCNTs lodged in the binder phase are believed to form conductive pathways which impart low conductivity to the otherwise insulative PDMS binder. The formation and disruption of the conductive pathways result in large changes in the overall resistance of the material [177, 178]. Upon mechanical stimuli, the effects of inherent MWCNT piezoresistivity leads to a change in the resistivity of the bulk material itself, thereby adding significant non-linearity in the macroscale resistance change [176, 177, 178, 179]. Geometric effects are enhanced by the addition of MWCNT network owing to the decrease in the overall conductivity of the bulk material. A combination of all these mechanisms are responsible for the sensing behavior observed in MWCNT/PDMS nanocomposite binders [170, 171].

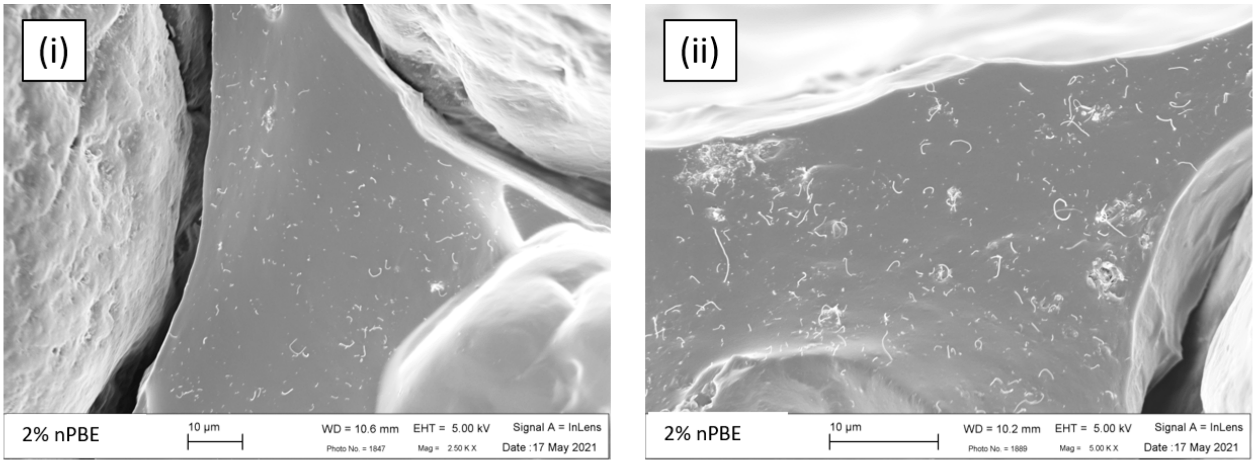

(a) i-ii: SEM images of 2% nPBE samples acquired at different locations on the fracture surface showing the presence and distribution of MWCNTs within the binder.

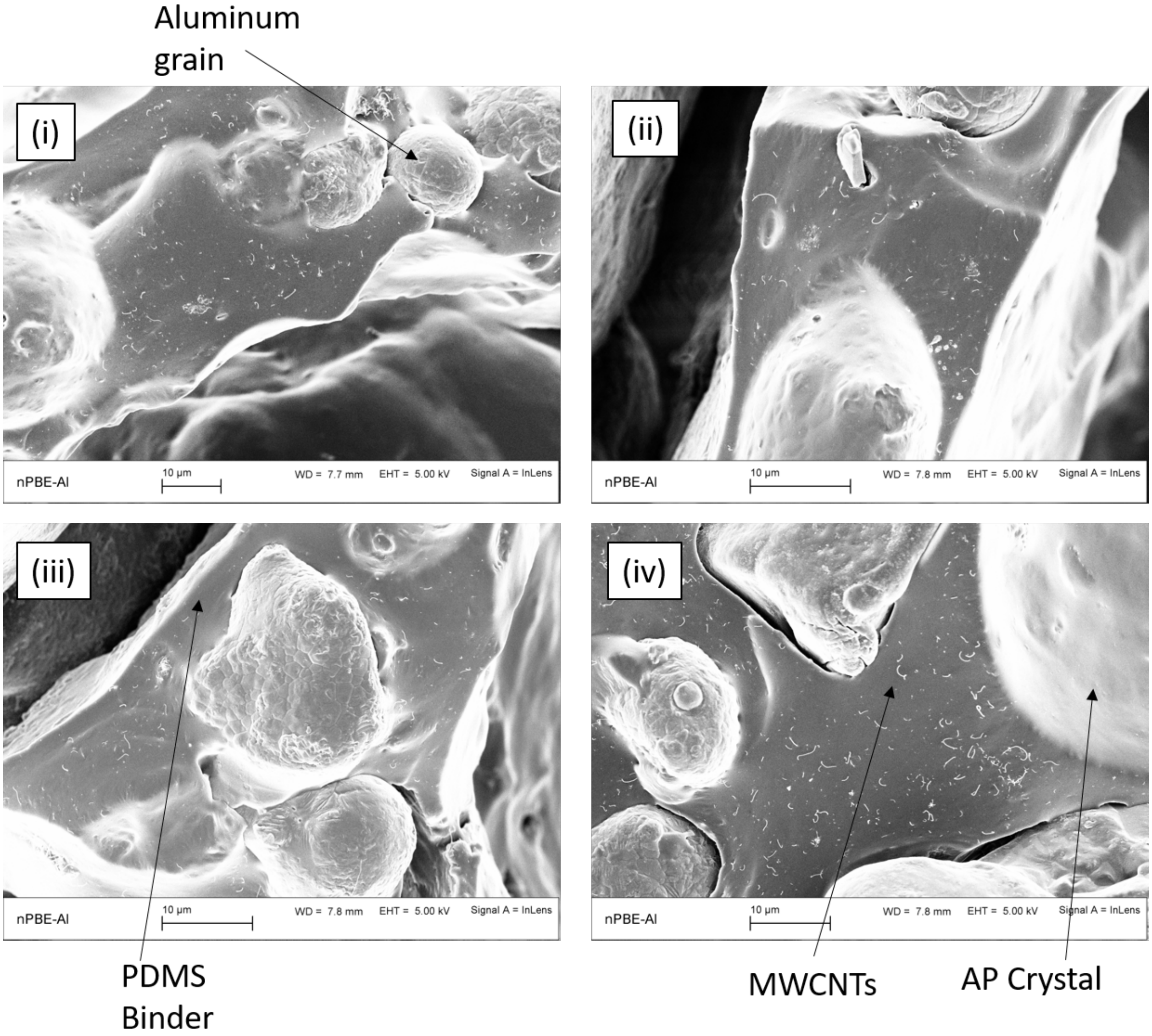

(b) i-iv: SEM images of 2% nPBE-AL samples acquired at different locations on the fracture surface showing the presence and distribution of MWCNTs and aluminum grains within the binder.

7.3.3 Electro-mechanical sensing in polymer bonded energetic nanocomposites (AP based nPBE sample)

Based on the electrical results obtained from the nBinder samples, certain inferences are drawn which shall direct the focus for nPBE samples. Primarily, the study with the nBinder samples revealed critical information about the percolation threshold and weight concentration at which the MWCNT network is able to obtain reliable and quality signals. Accordingly, the 2% nPBE samples were selected to be studied in detail[9]. Figure 7.11 shows the change in normalized resistance as a function of mechanical strain, plotted in conjunction with the stress-strain curve for the 2% nPBE samples. Additionally, zoomed-in graphs show distinct areas from the stress-strain curve and the change in normalized resistance curve for detailed viewing.

The electrical response for the nPBE samples behave differently compared to the nBinder samples. There is a small region (approximately <0.8% strain) where the resistance shows a plateau, after which the resistance starts to increase slightly (indicated by the small normalized change value). This occurs in a region where, from the stress-strain curve, elastic behavior is expected (and by extension, a decrease in resistance, similar to the nBinder samples). Figure 7.6a shows an SEM image of the microstructure of an nPBE sample which highlights the distribution of the binder and the AP crystals. It can be observed that the nanocomposite PDMS binder forms narrow struts, beams, and columns between adjacent AP crystals. During compression, complex stress states exist within such heterogeneous nPBE microstructures, with some regions under compression and some regions under tension [165, 166, 177, 178]. It is believed that during compression, the beam-like binder structures undergo bending resulting in compressive and tensile stress

---

[9] 0.8%, and 1% nPBE samples were also studied. However, a similar trend was observed where the 2% nPBE samples exhibited reliable and good electrical sensing behavior, and hence only that data is presented to avoid repetitiveness.

states, which have a net-zero effect on resistance change[10]. This explains the unchanged resistance values at <0.8% strain. At strains >0.8%, increasing resistance suggests that the electrical signal may be picking up microscale damage events such as crystal-binder debonding or void expansions, very early on even during mechanical elastic behavior. The average gauge factor calculated for this region is ∼10 which is still significantly higher than conventional strain gauges.

Between 3% and 18% strain, a distinct change in the slope of the mechanical stress-strain curve can be seen, indicating the onset of damage, which is replicated by the change in the slope of the resistance curve. As damage occurs, there are disruptions in the electrical conductive pathways, and hence the resistance increases (as seen in the theoretical model graph shown in Figure 7.9). The gauge factor in this region increases to about 17.7, indicating the massive effect of conductive pathway disruption due to damage at the microscale. Additionally, upon further observation, the resistance curve changes its slope ∼0.025 strain before the mechanical damage initiates (at 0.1 strain), indicating that the nanoscale MWCNT network is more sensitive to mechanical stimuli than the macroscale mechanical response measured via the load cell. Beyond 18% strain, strain hardening behavior is observed until macroscale failure occurs around ∼42% strain. The electrical response is sensitive to the effective change in distance between individual MWCNTs as well as the formation and disruption of conductive pathways. At the nanoscale, strain hardening in elastomeric binders is caused by changes in the molecular structure resulting in increased stiffness [181]. However, the change in the physical distance between individual MWCNTs in the network is reduced due to increased constraint within the material causing a slight decrease in the MWCNT network's sensitivity [181, 182]. This can be verified via the gauge factor for this region which drastically reduces to 6.7,

---

[10] Tension causes the resistance to increase, whereas compression causing the resistance to decrease in a homogeneous conductor.

indicating reduced MWCNT network's electromechanical sensitivity. The overall increasing resistance in this region indicates that the accumulation of microscale damage is the dominant driver of the resistance change, however, the negative change in slope indicates the decreased sensitivity of the MWCNT network due to strain hardening. A similar resistance response can be observed in the nBinder samples in the strain hardening region of the stress-strain curve. Towards the end of the stress-strain curve (>42% strain), large macroscale cracks and ruptures occur in the PBE samples, which substantially severs the electrical circuit causing very high resistance values[11].

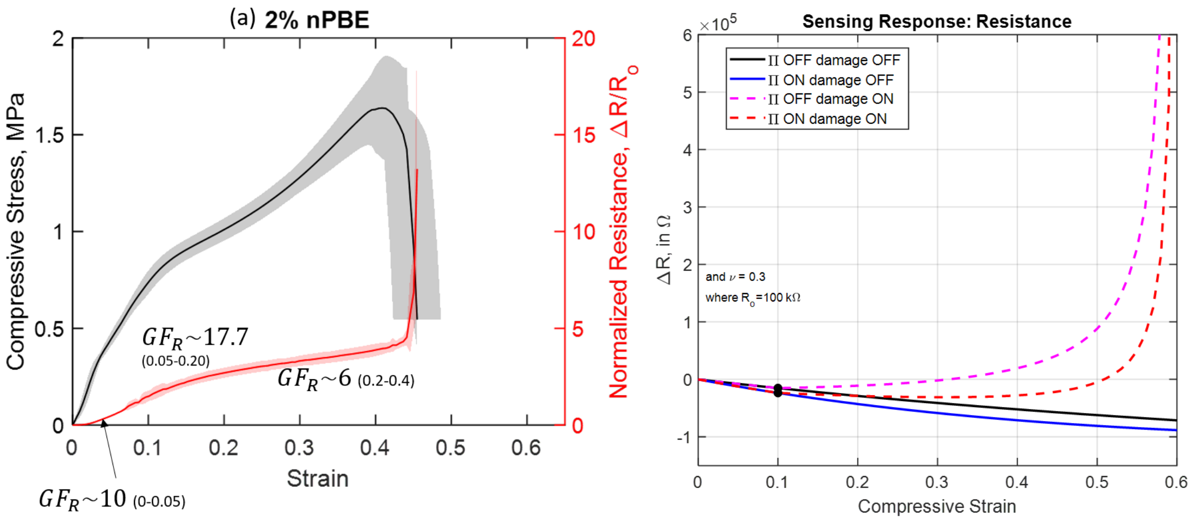

Figure 7.11: (a) The electromechanical response of 2% nPBE samples. (b) Theoretical model showing the behavior of a homogeneous solid under strain and subsequent damage. Detailed information about the theoretical models are presented in Appendix D.

---

[11] Since the sample is under compression, there is some degree of contact between ruptured surfaces through which an electrical signal may be obtained.

7.3.4 Electro-mechanical sensing in polymer bonded energetic nanocomposites (Aluminized AP based nPBE-Al samples)

The addition of Aluminum powder to the PBE sample composition represents a complete polymer bonded energetic composition, often used to fabricate solid rocket motors [97, 145, 157, 158]. Since Aluminum is an electrically conductive material, its addition introduces a conductive phase in the PBE composition. The influence of this conductive grain phase on the sensing abilities of the MWCNT network is evaluated in this section. Figures 7.12a and 7.12b show the change in normalized resistance plotted in conjunction with the stress-strain curve for the neat PBE-AL and 2% nPBE-AL samples, respectively. The solid lines represent the average response, while the shaded regions indicate the variation in the data representing two standard deviations.

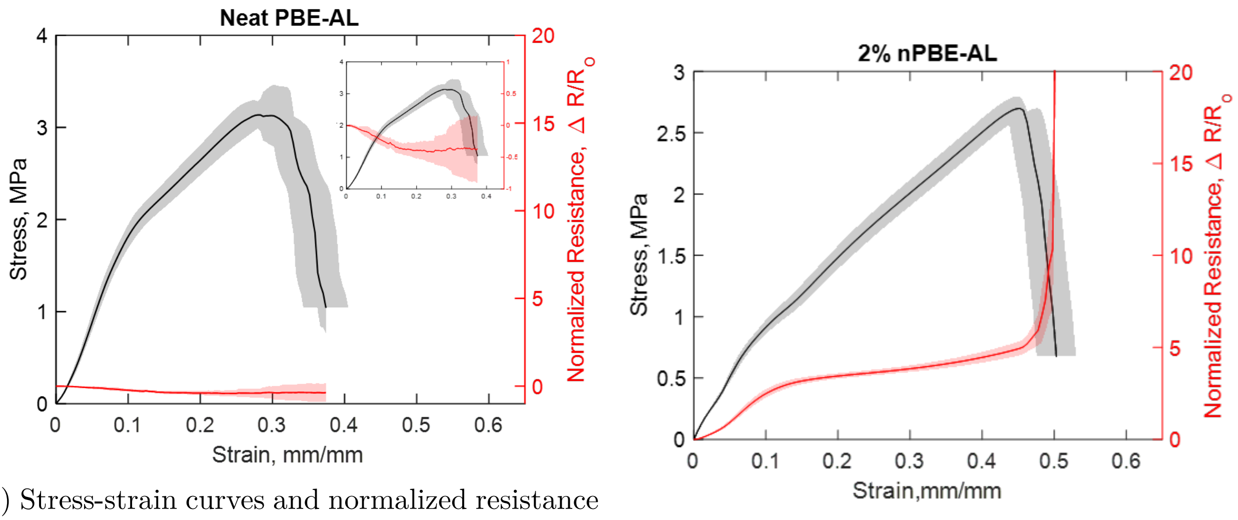

(a) Stress-strain curves and normalized resistance curves for Neat PBE-AL. (Inset): same plot showed with a re-scaled right y-axis to allow better visualization of the electrical response

(b) Stress-strain curves and normalized resistance curves for 2% nPBE-AL.

Figure 7.12: Stress-Strain and normalized resistance curves for the aluminized PBE samples. Solid black lines represent the average stress-strain, while solid red lines represent the average change in normalized resistance. Shaded regions indicate the variation in data representing two standard deviations.

It can be observed in Figure 7.12a that the resistance decreases initially during the linear portion of the curve for PBE-AL samples. This is consistent with the strain sensing results observed in the nBinder samples. The base resistance of the PBE-AL samples is relatively low and is comparable to the 1% nPBE samples (∼65 kΩ). Additionally, they also exhibit acceptable variance-to-mean ratios indicating that the bulk material can produce reliable electrical measurements. The effect of the addition of aluminum can be clearly seen on the electrical resistivity of the bulk material as it drastically lowers the overall resistance of the material (reduced from ∼1400 to ∼65 kΩ for neat samples; from ∼12 to ∼3 kΩ for 2% nanocomposite samples). In addition, the size, concentration and distribution of the aluminum may be less sensitive to matrix damage thus leading to lessened disruptions in conductive pathways. These factors allow the neat PBE-AL samples to exhibit sensing driven by changes in the geometric dimensions of the sample i.e. geometric sensing. During this process, the resistance decreases by ∼40 % of the base resistance value. As the strain increases, it can be observed that the noise in the resistance data recorded increases. However, the average resistance values remain fairly unchanged, indicating that the neat PBE-AL samples do not have an appreciable increase in resistance due to damage. This is believed to be due to continued contact between fractured surfaces of the sample even after damage which allows electrical conduction to occur. The increase in noise may occur due to electrode deterioration at higher strains and increased contact resistance between the re-connected fracture surfaces of the sample which undergo constant movement as the strain increases progressively.

In the case of the nanocomposite PBE-AL samples, it is hypothesized that the piezoresistive ability of MWCNT networks may detect damage and cause large increases in the resistance which overcome the competing effect of geometric sensing. Such behavior can indeed be observed in Figure 7.12b, where the resistance increases up to 5 times its base value until macroscale failure occurs, at which point the resistance increases many folds. The initial plateau and gradual increase in resistance during the linear portion of the stress-strain curve is consistent with the behavior of the 2% nPBE samples. The gauge factor calculated in this region is 19, which exceeds the gauge factors of conventional strain gauges. At ∼6% strain where the first instance of damage can be observed in the stress-strain curve, the resistance increases sharply sloping upwards. The slope of the resistance curve changes once again during strain hardening, and the change in resistance becomes more gradual (reduces to 5.1), similar to that observed in the nBinder and nPBE samples during their respective strain hardening regions. The gauge factors calculated in these regions are 22.4 and 5.1, respectively (shown in Table 7.3); these GFs indicate the effectiveness of MWCNT networks as damage sensors during microscale damage evolution. At ∼45% strain, macroscale cracks begin to appear in the sample and the ruptures lead to severe loss in conductivity, indicated by the rapid increase in resistance. The significant amount of overall resistance change observed in the 2% nPBE-AL samples between 0-45% strain points to the increased electrical sensitivity brought about by the MWCNT network. Additionally, the MWCNT network is able to detect damage and influence the overall bulk resistance of the material such that the competing geometric effects can be overcome. Thus, the addition of aluminum, or in other words, the addition of a conductive phase in polymer bonded energetics does not seem to inhibit the piezoresistive sensing abilities of the MWCNT networks.

Chapter 8

Conclusions

In this experimental work, material property enhancement capabilities of the carbon-based nanoparticle dispersions are explored. Overall, two primary research areas are investigated under this theme: fracture toughness enhancement in structural epoxy matrix materials, and electro-mechanical sensing via multifunctional nanocomposite polymer bonded energetics (PBEs). The former leverages the mechanical enhancement capability of carbon nanotube (CNT) and graphene nanoplatelet (GNP) dispersions, while the latter leverages the multifunctional abilities of dispersed CNT networks with regards to their piezoresistive abilities. For simplicity, this written work is divided into two parts, each representing the two research areas described above. This chapter summarizes the conclusions, contributions, key observations, and key takeaways of the various studies/investigations presented as chapters in this dissertation.

In Chapter 2, enhancements in initiation fracture toughness of structural epoxies brought about by the addition of carbon nanotubes (CNTs) and graphene nanoplatelets (GNPS) have been investigated. Samples with different weight concentrations of nanofillers were studied. High shear mixing was employed as the method for nanofiller dispersion. CNT-Epoxy, GNP-Epoxy, and CNT/GNP-Epoxy compact tension samples at 0.1% and 0.5% nanofiller weight concentration were fabricated. Mode-I fracture toughness tests were conducted according to ASTM D5045. Results were compared with those from neat epoxy samples, which served as a baseline. Following is a summary of the key observations of this study.

1. Significant enhancements in the critical stress intensity factor (K_{IC}) and the critical fracture energy (G_{IC}) were observed in all the reinforced nanocomposite epoxy samples relative to the neat epoxy samples.

2. Statistically similar enhancements were observed at the same weight concentration of the nanofillers.

3. Similar initiation fracture toughness values (K_{IC}) were observed for CNT-Epoxy and GNP-Epoxy at 0.1% and 0.5% weight loading.

4. SEM images of CNT-Epoxy samples' fracture surfaces reveal the presence of CNT agglomerations. An increasing number of agglomerations were observed at higher weight loadings.

5. Identifying GNPs with complete certainty is challenging via SEM imaging. Instead, GNPs can be observed by the virtue of the fractographical artifact they produce during crack propagation.

6. Instances of crack bridging and crack deflection were observed, through their fractographical artifacts, on fracture surfaces of CNT-Epoxy and GNP-Epoxy, respectively.

7. For CNT-Epoxy samples, the increased strain energy accumulation due to high stiffness and strength, and the energy penalty associated with CNT pullouts result in an enhancement of initiation fracture toughness.

8. For GNP-Epoxy samples, the increased strain energy accumulation due to high stiffness and strength, and the energy penalty associated with crack deflection around GNPs result in an enhancement of initiation fracture toughness.

9. Upon studying the working mechanics of crack deflection and crack bridging, it was understood that there are certain favorable orientations where maximum resistance to crack growth can be obtained. As such, nanofiller alignment may result in higher levels of enhancement.
10. Preliminary results with CNT/GNP 1:1 dual filler samples indicate an absence of synergy between the two nanoparticles.

In Chapter 3, the initiation fracture toughness study was continued and extended to more dual nanofiller ratios. The motivation behind investigating dual nanofiller reinforcements lies in their possible synergistic advantage over the single nanofiller reinforcements. Ultra-sonication was employed as the method of dispersion of nanofillers, to study the influence of the dispersion method. CNT/GNP ratios of 1:3, 1:1, and 3:1 were explored along with single nanofiller systems. The testing procedure, material fabrication, and sample preparation methods were kept consistent with the previous study. The key observations from this study are summarized below:

1. Significant levels of enhancement in the critical stress intensity factor (K_{IC}) and critical fracture energy (G_{IC}) were observed in all the reinforced epoxies, relative to the baseline neat epoxy.
2. No particular synergy was observed in the dual nanofiller epoxies. The reinforced epoxies experienced a statistically similar enhancement in K_{IC} and G_{IC} relative to the neat epoxy.
3. The enhancement obtained via ultra-sonication dispersion was lower than that obtained via high shear mixing. This was due to the different processing conditions during ultra-sonication. Particularly, the epoxy is exposed to acetone during the dispersion process which affects its mechanical properties.

4. SEM imaging showed that better dispersion was achieved in CNT-Epoxy samples via the sonication method.
5. Artifacts of crack bridging and crack deflection were observed via SEM imaging in the CNT-Epoxy, and GNP-Epoxy, respectively.
6. SEM imaging of the dual nanofiller epoxies showed artifacts of crack bridging as well as crack deflection. The frequency of crack deflection events decreased as the dual nanofiller ratios transitioned from being GNP dominated to CNT dominated.
7. Increased agglomeration behavior was observed in the dual nanofiller samples, pointing to poorer dispersion (relative to the single nanofiller systems). This is believed to have affected any possible synergistic interactions between CNT/GNP reinforcements.

In Chapter 4, the influence of pre-crack characteristics, such as the pre-crack length, crack front shape, and crack plane profile, on the Mode-I fracture toughness of epoxy polymer was investigated. K_{IC} values were calculated using the data processing guidelines established by the ASTM D5045 standard, and subsequently, the influence of the pre-crack characteristics on the K_{IC} values was evaluated. The work presented herein aims at allowing better engineering design decisions as well as better operational evaluations of cracks in structures by quantifying the pre-crack characteristics and explaining their influence on the fracture toughness properties of polymeric materials. Key contributions, observations, and results are summarized below:

1. In the correlation for pre-crack length and K_{IC}, it was found that after an initial plateau, the K_{IC} values dropped significantly accompanied by higher variation in the data as well. This suggests that a maximum permissible pre-crack length exists, proportional to the sample geometry, under which consistent K_{IC} values can be obtained.

2. A quantitative method for quantifying the crack front shape is introduced using crack front inclination, which refers to the inclination of the best-fit linear line passing through the traced pre-crack front shape; and arc-chord tortuosity, which indicates the degree of the waviness of the traced pre-crack front shape.

3. It was observed that samples having crack front shape inclinations lesser than 10 degrees relative to the through-thickness direction; and tortuosity less than 1.05 exhibited the most reproducible and consistent K_{IC} values.

4. Fractographical analysis via digital microscopy revealed that the crack plane profiles can be classified as two distinct types: a smooth, featureless surface and a surface containing twist hackles parallel to the direction of macroscale crack propagation.

5. The presence of twist hackles indicated the presence of mode mixity occurring during the pre-cracking process.

6. Two different post-initiation crack behaviors were observed in the load-displacement curves which were directly correlated to the surface features observed on the pre-crack plane profile. The smooth surfaces resulted in a load drop followed by a gradual reduction to zero load, indicating pure Mode-I fracture failure. The rough surfaces containing twist hackles resulted in reloading after crack initiation, which can be attributed to the higher energy required for crack growth owing to mixed Mode I/III presence.

7. Tests performed at a two displacement rates (0.5 and 2 mm/min) confirmed that plastic flow ahead of the crack tip is inhibited at higher strain rates, and the faster accumulation of strain energy in the sample exceeds the critical fracture energy more quickly leading to rapid crack growth. This results in a load drop after crack initiation followed by a gradual reduction to zero load, with no instances of reloading observed.

In Chapter 6, strain and damage sensing in polymer-bonded mock energetics (mock PBEs) was investigated through the characterization of the piezoresistive response of carbon nanotube sensing networks subjected to quasi-static tensile and compressive mechanical loading. The mock PBEs were prepared with sugar crystals as a substitute for energetic particulates. Polydimethylsiloxane (PDMS) was used a the poymer binder. Aluminized mock PBEs were fabricated as well to study the effects of conductive grains on the sensing abilities of CNT networks. In total, four material systems were fabricated to assess the individual contributions of constituents to the piezoresistive response. The electrical response was monitored in conjunction with the mechanical response. Monotonic tension and compression tests were conducted until sample failure to assess strain and damage sensing capabilities. Key contributions, observations, and results are summarized below:

1. Addition of CNTs to mock PBEs drastically reduced their base resistance value such that practical measurement could be taken for structural health monitoring applications.

2. In general, the neat samples with CNTs exhibited geometric sensing only; however, the high base resistance values resulted in noisy and unreliable electrical data.

3. The nanocomposite mock PBEs exhibited a change in their resistance value as a function of the applied strain. This was observed in both, tension and compression, indicating the ability of the CNT networks to sense strain and damage.

4. The change in normalized resistance and reactance as a function of applied strain was quantified by the use of tangent gauge factors.

5. Distinct gauge factors were obtained corresponding to different regions of the stress-strain curves (the elastic strain region, beyond which the evolution of damage occurs).

6. SEM imaging revealed the presence of CNTs dispersed in the binder phase of the nanocomposite mock PBEs.
7. Mock crystal and binder debonding, and matrix rupture were the dominant failure mechanisms in all the mock PBE samples.
8. Increased number of voids were observed in the nanocomposite samples.
9. FE-SEM imaging of the fractured surfaces confirmed the presence of MWCNTs in microscopic cracks and on the fracture surface, which is thought to be responsible for the microscopic strain/damage sensing abilities in nanocomposite mock PBEs.
10. The piezoresistive characteristics of the dispersed CNT networks were not hindered by the inclusion of conductive aluminum grains.
11. The addition of aluminum significantly decreased the base resistance value of the mock PBE samples. This made the electrical signals more reliable and more practically measureable thereby improving the sensing ability of the effective material.

In Chapter 7, an experimental investigation of a real-time, in-situ structural health monitoring (SHM) system for actual polymer bonded energetics (PBEs) is presented. Ammonium perchlorate (AP) is utilized as the primary energetic particulate, while aluminum powder is added as a metallic fuel which serves the purpose of accelerating the ignition. Polydimethylsiloxane (PDMS) is used as the binder phase. The SHM system is based on the piezoresistive abilities of embedded multi-walled carbon nanotube (MWCNT) networks distributed within the binder phase of PBEs. As such, the effect of each constituent in the PBE material system is comprehensively studied. To that effect, the SHM capabilities of MWCNT/PDMS (nBinder) materials were evaluated to study the binder's electromechanical response, followed by AP/MWCNT/PDMS (nPBE) which assessed the impact of AP addition, and finally, AP/AL/MWCNT/PDMS (nPBE-AL) which evaluated the impact of adding conductive grains such as aluminum. Electromechanical tests were conducted by subjecting compression samples (ASTM D695) to monotonic compression while the electrical resistance was recorded. Gauge factors were calculated to quantify the sensitivity of the MWCNT network to mechanical stimuli.

1. The theoretical models (Appendix D) indicate that in compression, the electrical resistance should decrease. When damage occurs, the electrical response should increase.

2. It was observed that the 2% nBinder exhibited excellent strain sensing ability. Damage was not particularly expected to occur during compression in the nBinder samples since PDMS exhibits strong elastomeric behavior. Hence, upon compression the resistance decreased since the conductive CNT network was more compacted, thereby increasing bulk conductivity.

3. The gauge factors obtained for 2% nBinder samples are comparable with conventional strain gauges. Beyond the linear elastic region, strain hardening occurred during which the CNT network exhibited decreased electrical sensitivity, indicated by a ∼60% drop in the gauge factor value.

4. Upon addition of the AP particulate phase, the stress-strain response changed; distinct regions of elastic strain, damage initiation, and damage evolution were now observed.

5. The 2% nPBE samples exhibited unchanged resistance followed by a non-linearly increasing resistance value during the linear portion of the stress-strain curve. Since the occurrence of damage causes the resistance values to increase, it is hypothesized that the MWCNT network can pick up microscale damage events such as crystal-binder debonding even during the linear stress-strain growth.

6. The initial unchanged resistance is attributed to alternating states of tension and compression, which have competing effects on resistance change, that may exist in the complex microstructure of the PBEs which indicate the presence of struts, columns, and beams formed by the binder that occupies the space between the crystals (observed in the SEM images of the fracture surfaces as well).

7. As damage initiation occurs, the CNT networks start to disrupt thus causing the resistance values to increase quickly. This is reflected by the high gauge factors obtained in this region of the stress-strain curve. It was also observed that the MWCNT network begins to change slopes slightly before the stress-strain curve changes, indicating the superior sensitivity of the MWCNT network compared to the mechanical load cell.

8. Similar to the nBinder samples, the sensitivity of the MWCNT network decreases during strain hardening.

9. During macroscale damage, large cracks cause massive disruptions in the electrical connectivity, and hence the resistance sharply increases.

10. The 2% nPBE-AL samples, in terms of electrical sensing, behaved similarly to the 2% nPBE samples. The addition of conductive grains does not seem to inhibit the MWCNT network sensitivity.

11. The overall base resistance of the nPBE-AL samples was much lower, which is a practically beneficial characteristic in terms of the final application.

12. Based on the current results and observations, a structural health monitoring system based on embedded MWCNT networks shows the potential to address the key issue of real-time damage assessment in polymer bonded energetic materials.

Chapter 9

Future Work

Polymer matrix fiber-reinforced composites often have good strength-to-weight ratios and high stiffnesses; however, they typically have low fracture toughness values. In the first part of this work, this issue has been addressed. Specifically, successful efforts were carried out to mitigate matrix cracking, a failure mode where cracks develop in the matrix material due to cohesive failure of the matrix. This was achieved via nanofiller reinforcements dispersed within the polymer matrix. However, this approach and its resulting enhancement is only one piece of the puzzle in the grand scheme of improving the fracture toughness of fiber-reinforced polymer composites. Other failure modes such as fiber-matrix debonding, and delamination also result in the formation of cracks wherein different approaches for fracture toughness enhancement will be required. Continuing on the theme of the use of carbon-based nanoparticles, the issue of fiber-matrix debonding can be addressed using fuzzy fibers, which involves growing CNTs on carbon fibers such that the adhesive strength between the fiber and matrix is enhanced due to inter-penetration of the matrix and fiber interface [183]. For delamination, in-plane ply stitching is a viable approach that is analogous to crack bridging at the macroscale [184]. Nanofiller reinforced adhesive layers between lamina layers are also been investigated as a solution to mitigate delamination. A holistic approach where these various approaches for fracture toughness enhancement are combined is required. Future work in this direction will significantly improve the usability of fiber-reinforced polymer matrix composites as structural materials. Chapter 4 also investigated the effect of pre-crack characteristics on the initiation fracture toughness values. This novel work can be expanded by systematically identifying and studying more factors that may affect the initiation and subsequent propagation of cracks thereby allowing better engineering design decisions as well as better operational evaluations of cracks in structures. In the second part of this dissertation, a successful demonstration of a structural health monitoring system for polymer-bonded energetics was presented. This proof-of-concept demonstration was conducted under quasi-static, monotonic tension/compression loads. Further efforts are required to investigate the behavior of piezoresistive CNT networks under dynamic loadings and thermal loads. Additionally, more information about the microstructure of these heterogeneous polymer bonded energetics will help in understanding the damage mechanisms occurring within the material, further demystifying the correlation between the electrical and the stress-strain response. Increased understanding of the material behavior will improve the proof-of-concept structural health monitoring system developed herein and can comprehensively address the key issue of damage assessment in polymer bonded energetic materials.

Bibliography

[1] B. Farahmand, *Fracture Mechanics of Metals, Composites, Welds, and Bolted Joints.* US: Springer, 2001.

[2] "Liberty ship failure via fracture." https://metallurgyandmaterials.wordpress.com/2015/12/25/liberty-ship-failures.

[3] N. E. Dowling, *Mechanical behavior of materials: engineering methods for deformation, fracture, and fatigue; 4th ed.* Boston, MA: Pearson, 2012.

[4] "Mixed-mode fracture toughness of composite." https://www.compositesworld.com/articles/mixed-mode-fracture-toughness-of-composites.

[5] ASTM International, "(ASTM D 5054) - Standard Test Methods for Plane-Strain Fracture Toughness and Strain Energy Release Rate of Plastic Materials," *ASTM Book of Standards*, vol. 99, no. Reapproved 2007, pp. 1–9, 2013.

[6] J. L. Koenig, P. Materials, E. I. Materials, P. Matrix, C. Materials, C. Angle, M. Goniometers, and Radford, "D 5528 – 94a Standard Test Method for Mode I Interlaminar Fracture Toughness of Unidirectional Fiber-Reinforced Polymer Matrix Composites," vol. 12, no. 2, pp. 1–8, 2004.

[7] ASTM D7905, "Standard test method for determination of the mode II interlaminar fracture toughness of unidirectional fiber-reinforced polymer matrix composites," *Astm*, pp. 1–18, 2014.

[8] P. Materials, E. I. Materials, P. Matrix, C. Materials, and P. Specimens, "D 6671 – 01 Standard Test Method for Mixed Mode I-Mode II Interlaminar Fracture Toughness

of Unidirectional Fiber Reinforced Polymer Matrix Composites," vol. 15, no. January 2004, pp. 1–15, 2016.

[9] E. E. Miller, Y. Hua, and F. H. Tezel, "Materials for energy storage: Review of electrode materials and methods of increasing capacitance for supercapacitors," *Journal of Energy Storage*, vol. 20, no. September, pp. 30–40, 2018.

[10] G. Mittal, V. Dhand, K. Y. Rhee, S. J. Park, and W. R. Lee, "A review on carbon nanotubes and graphene as fillers in reinforced polymer nanocomposites," *Journal of Industrial and Engineering Chemistry*, vol. 21, pp. 11–25, 2015.

[11] D. C. Hofmann, J. Y. Suh, A. Wiest, G. Duan, M. L. Lind, M. D. Demetriou, and W. L. Johnson, "Designing metallic glass matrix composites with high toughness and tensile ductility," *Nature*, vol. 451, no. 7182, pp. 1085–1089, 2008.

[12] A. S. Argon, R. E. Cohen, and T. M. Mower, "Mechanisms of toughening brittle polymers," *Materials Science and Engineering A*, vol. 176, no. 1-2, pp. 79–90, 1994.

[13] N. Domun, H. Hadavinia, T. Zhang, T. Sainsbury, G. H. Liaghat, and S. Vahid, "Improving the fracture toughness and the strength of epoxy using nanomaterials-a review of the current status," *Nanoscale*, vol. 7, no. 23, pp. 10294–10329, 2015.

[14] F. H. Gojny, M. H. Wichmann, B. Fiedler, and K. Schulte, "Influence of different carbon nanotubes on the mechanical properties of epoxy matrix composites - A comparative study," *Composites Science and Technology*, vol. 65, no. 15-16 SPEC. ISS., pp. 2300–2313, 2005.

[15] P. Rosso, L. Ye, K. Friedrich, and S. Sprenger, "A toughened epoxy resin by silica nanoparticle reinforcement," *Journal of Applied Polymer Science*, vol. 100, no. 3, pp. 1849–1855, 2006.

[16] G. Gkikas, N. M. Barkoula, and A. S. Paipetis, "Effect of dispersion conditions on the thermo-mechanical and toughness properties of multi walled carbon nanotubes-reinforced epoxy," *Composites Part B: Engineering*, vol. 43, no. 6, pp. 2697–2705, 2012.

[17] M. Ravandi, W. S. Teo, L. Q. Tran, M. S. Yong, and T. E. Tay, "The effects of through-the-thickness stitching on the Mode I interlaminar fracture toughness of flax/epoxy composite laminates," *Materials and Design*, vol. 109, pp. 659–669, 2016.

[18] D. M. Nuruzzaman, "Composites Communication," 2020.

[19] S. S. Wicks and B. L. Wardle, "Interlaminar fracture toughness of laminated woven composites reinforced with aligned nanoscale fibers: Mechanisms at the macro, micro, and nano scales," *54th AIAA/ASME/ASCE/AHS/ASC Structures, Structural Dynamics, and Materials Conference*, pp. 1–9, 2013.

[20] N. Sela and O. Ishai, "Interlaminar fracture toughness and toughening of laminated composite materials: a review," *Composites*, vol. 20, no. 5, pp. 423–435, 1989.

[21] H. T. Truong, D. C. Lagoudas, O. O. Ochoa, and K. Lafdi, "Fracture toughness of fiber metal laminates: Carbon nanotube modified Ti-polymer-matrix composite interface," *Journal of Composite Materials*, vol. 48, no. 22, pp. 2697–2710, 2014.

[22] N. T. Kamar, L. T. Drzal, A. Lee, and P. Askeland, "Nanoscale toughening of carbon fiber reinforced/epoxy polymer composites (CFRPs) using a triblock copolymer," *Polymer*, vol. 111, pp. 36–47, 2017.

[23] M. Bakar and F. Djaider, "Effect of plasticizers content on the mechanical properties of unsaturated polyester resin," *Journal of Thermoplastic Composite Materials*, vol. 20, no. 1, pp. 53–64, 2007.

[24] Z. Heng, Y. Chen, H. Zou, and M. Liang, "Simultaneously enhanced tensile strength and fracture toughness of epoxy resins by a poly(ethylene oxide)-block-carboxyl terminated butadiene-acrylonitrile rubber dilock copolymer," *RSC Advances*, vol. 5, no. 53, pp. 42362–42368, 2015.

[25] M. R. Dadfar and F. Ghadami, "Effect of rubber modification on fracture toughness properties of glass reinforced hot cured epoxy composites," *Materials and Design*, vol. 47, pp. 16–20, 2013.

[26] M. G. A. Vieira, M. A. Da Silva, L. O. Dos Santos, and M. M. Beppu, "Natural-based plasticizers and biopolymer films: A review," *European Polymer Journal*, vol. 47, no. 3, pp. 254–263, 2011.

[27] J. T. Van Oosterhout and M. Gilbert, "Interactions between PVC and binary or ternary blends of plasticizers. Part I. PVC/plasticizer compatibility," *Polymer*, vol. 44, no. 26, pp. 8081–8094, 2003.

[28] A. Kumar, S. Li, S. Roy, J. A. King, and G. M. Odegard, "Fracture properties of nanographene reinforced EPON 862 thermoset polymer system," *Composites Science and Technology*, vol. 114, pp. 87–93, 2015.

[29] N. Shirodkar, S. Rocker, and G. D. Seidel, "Strain and damage sensing of polymer bonded mock energetics via piezoresistivity from carbon nanotube networks," *Smart Materials and Structures*, vol. 28, no. 10, p. 104006, 2019.

[30] A. K. Chaurasia and G. D. Seidel, "Computational micromechanics analysis of electron-hopping-induced conductive paths and associated macroscale piezoresistive response in carbon nanotube–polymer nanocomposites," *Journal of Intelligent Material Systems and Structures*, vol. 25, no. 17, pp. 2141–2164, 2014.

[31] A. K. Chaurasia, X. Ren, and G. D. Seidel, "Computational micromechanics analysis of electron hopping and interfacial damage induced piezoresistive response in carbon nanotube-polymer nanocomposites," *Smart Materials and Structures*, vol. 23, p. 075023, jun 2014.

[32] A. Chaurasia and G. Seidel, "Computational micromechanics analysis of electron hopping and interfacial damage induced piezoresistive response in carbon nanotube-polymer nanocomposites subjected to cyclic loading conditions," *European Journal of Mechanics - A/Solids*, vol. 64, pp. 112 – 130, 2017.

[33] A. K. Chaurasia, A. M. Rukangu, M. K. Philen, G. D. Seidel, and E. C. Freeman, "Evaluation of bending modulus of lipid bilayers using undulation and orientation analysis," *Physical Review E*, vol. 97, pp. 032421 – 12 pgs, 2018.

[34] A. K. Chaurasia, E. C. Sengezer, K. K. Talamadupula, S. Povolny, and G. D. Seidel, "Experimental characterization and computational modeling of deformation and damage sensing through the piezoresistive response of nanocomposite bonded surrogate energetic materials," *Journal of Multifunctional Composites*, vol. 2, no. 4, pp. 227–253, 2014.

[35] G. Domínguez-Rodríguez, A. Tapia, G. D. Seidel, and F. Avilés, "Influence of structural defects on the electrical properties of carbon nanotubes and their polymer composites ," *Advanced Engineering Materials*, vol. 18, no. 11, pp. 1897–1905, 2016.

[36] G. Dominguez-Rodriguez, A. Chaurasia, G. Seidel, A. Tapia, and F. Aviles, "Hierarchical multiscale modeling of the effect of carbon nanotube damage on the elastic properties of polymer nanocomposites," *Journal of Mechanics of Materials and Structures*, vol. 12, no. 3, pp. 263 – 287, 2017.

[37] J. J. Ku-Herrera, F. Avilés, and G. D. Seidel, “Self-sensing of elastic strain, matrix yielding and plasticity in multiwall carbon nanotube/vinyl ester composites,” *Smart Materials and Structures*, vol. 22, p. 085003, jun 2013.

[38] Y. Li and G. D. Seidel, “Multiscale modeling of the effects of nanoscale load transfer on the effective elastic properties of unfunctionalized carbon nanotube–polyethylene nanocomposites,” *Modelling and Simulation in Materials Science and Engineering*, vol. 22, p. 025023, feb 2014.

[39] Y. Li and G. Seidel, “Multiscale modeling of functionalized interface effects on the effective elastic material properties of cnt–polyethylene nanocomposites,” *Computational Materials Science*, vol. 107, pp. 216 – 234, 2015.

[40] Y. Li and G. Seidel, “Multiscale modeling of the interface effects in cnt-epoxy nanocomposites,” *Computational Materials Science*, vol. 153, pp. 363 – 381, 2018.

[41] A. Oliva-Avilés, F. Avilés, V. Sosa, and G. Seidel, “Dielectrophoretic modeling of the dynamic carbon nanotube network formation in viscous media under alternating current electric fields,” *Carbon*, vol. 69, pp. 342 – 354, 2014.

[42] N. Prakash and G. D. Seidel, “Electromechanical peridynamics modeling of piezoresistive response of carbon nanotube nanocomposites,” *Computational Materials Science*, vol. 113, pp. 154 – 170, 2016.

[43] N. Prakash and G. D. Seidel, “Computational electromechanical peridynamics modeling of strain and damage sensing in nanocomposite bonded explosive materials (ncbx),” *Engineering Fracture Mechanics*, vol. 177, pp. 180–202, 2017.

[44] N. Prakash and G. D. Seidel, “Effects of microscale damage evolution on piezoresistive sensing in nanocomposite bonded explosives under dynamic loading via

electromechanical peridynamics," *Modelling and Simulation in Materials Science and Engineering*, vol. 26, no. 1, p. 015003, 2018.

[45] X. Ren and G. D. Seidel, "Computational micromechanics modeling of piezoresistivity in carbon nanotube–polymer nanocomposites," *Composite Interfaces*, vol. 20, no. 9, pp. 693–720, 2013.

[46] X. Ren and G. D. Seidel, "Computational micromechanics modeling of inherent piezoresistivity in carbon nanotube–polymer nanocomposites," *Journal of Intelligent Material Systems and Structures*, vol. 24, no. 12, pp. 1459–1483.

[47] X. Ren, J. Burton, G. D. Seidel, and K. Lafdi, "Computational multiscale modeling and characterization of piezoresistivity in fuzzy fiber reinforced polymer composites," *International Journal of Solids and Structures*, vol. 54, pp. 121 – 134, 2015.

[48] X. Ren, A. K. Chaurasia, A. I. Oliva-Avilés, J. J. Ku-Herrera, G. D. Seidel, and F. Avilés, "Modeling of mesoscale dispersion effect on the piezoresistivity of carbon nanotube-polymer nanocomposites via 3d computational multiscale micromechanics methods," *Smart Materials and Structures*, vol. 24, p. 065031, may 2015.

[49] X. Ren, A. K. Chaurasia, and G. D. Seidel, "Concurrent multiscale modeling of coupling between continuum damage and piezoresistivity in cnt-polymer nanocomposites," *International Journal of Solids and Structures*, vol. 96, pp. 340 – 354, 2016.

[50] R. Seifert, M. Patil, G. Seidel, and G. Reich, "Multifunctional topology optimization of strain-sensing nanocomposite beam structures," *Structural and Multidisciplinary Optimization*, vol. 60, no. 4, pp. 1407 – 1422, 2019.

[51] R. Seifert, M. Patil, and G. Seidel, "Topology optimization of self-sensing

nanocomposite structures with designed boundary conditions," *Smart Materials and Structures*, vol. 28, no. 7, pp. 074006 – 14 pgs, 2019.

[52] E. C. Sengezer, G. D. Seidel, and R. J. Bodnar, "Phenomenological characterization of fabrication of aligned pristine-swnt and cooh-swnt nanocomposites via dielectrophoresis under ac electric field," *Polymer Composites*, vol. 36, no. 7, pp. 1266–1279, 2015.

[53] E. C. Sengezer, G. D. Seidel, and R. J. Bodnar, "Anisotropic piezoresistivity characteristics of aligned carbon nanotube-polymer nanocomposites," *Smart Materials and Structures*, vol. 26, p. 095027, aug 2017.

[54] E. C. Sengezer and G. D. Seidel, "Structural health monitoring of nanocomposite bonded energetic materials through piezoresistive response," *AIAA Journal*, vol. 56, no. 3, pp. 1225–1238, 2018.

[55] K. K. Talamadupula, S. J. Povolny, N. Prakash, and G. D. Seidel, "Mesoscale strain and damage sensing in nanocomposite bonded energetic materials under low velocity impact with frictional heating via peridynamics," *Modelling and Simulation in Materials Science and Engineering*, vol. 28, p. 085011, nov 2020.

[56] K. K. Talamadupula, S. J. Povolny, N. Prakash, and G. D. Seidel, "Piezoresistive detection of simulated hotspots and the effects of low velocity impact at the mesoscale in nanocomposite bonded energetic materials via multiphysics peridynamics modeling," *Computational Materials Science*, vol. 188, pp. 110211 – 30 pgs, 2021.

[57] L. Sun, G. L. Warren, J. Y. O'Reilly, W. N. Everett, S. M. Lee, D. Davis, D. Lagoudas, and H. J. Sue, "Mechanical properties of surface-functionalized SWCNT/epoxy composites," *Carbon*, vol. 46, no. 2, pp. 320–328, 2008.

[58] F. Wang, L. T. Drzal, Y. Qin, and Z. Huang, "Size effect of graphene nanoplatelets on the morphology and mechanical behavior of glass fiber/epoxy composites," *Journal of Materials Science*, vol. 51, no. 7, pp. 3337–3348, 2016.

[59] Y. Zhou, F. Pervin, L. Lewis, and S. Jeelani, "Fabrication and characterization of carbon/epoxy composites mixed with multi-walled carbon nanotubes," *Materials Science and Engineering A*, vol. 475, no. 1-2, pp. 157–165, 2008.

[60] T. H. Hsieh, A. J. Kinloch, A. C. Taylor, and I. A. Kinloch, "The effect of carbon nanotubes on the fracture toughness and fatigue performance of a thermosetting epoxy polym," *Journal of Materials Science*, vol. 46, no. 23, pp. 7525–7535, 2011.

[61] I. Zaman, T. T. Phan, H. C. Kuan, Q. Meng, L. T. Bao La, L. Luong, O. Youssf, and J. Ma, "Epoxy/graphene platelets nanocomposites with two levels of interface strength," *Polymer*, vol. 52, no. 7, pp. 1603–1611, 2011.

[62] M. A. Rafiee, J. Rafiee, Z. Wang, H. Song, Z. Z. Yu, and N. Koratkar, "Enhanced mechanical properties of nanocomposites at low graphene content," *ACS Nano*, vol. 3, no. 12, pp. 3884–3890, 2009.

[63] M. M. Shokrieh, S. M. Ghoreishi, M. Esmkhani, and Z. Zhao, "Effects of graphene nanoplatelets and graphene nanosheets on fracture toughness of epoxy nanocomposites," *Fatigue and Fracture of Engineering Materials and Structures*, vol. 37, no. 10, pp. 1116–1123, 2014.

[64] M. R. Ayatollahi, S. Shadlou, and M. M. Shokrieh, "Fracture toughness of epoxy/multi-walled carbon nanotube nano-composites under bending and shear loading conditions," *Materials and Design*, vol. 32, no. 4, pp. 2115–2124, 2011.

[65] S. Chatterjee, F. Nafezarefi, N. H. Tai, L. Schlagenhauf, F. A. Nüesch, and B. T.

Chu, “Size and synergy effects of nanofiller hybrids including graphene nanoplatelets and carbon nanotubes in mechanical properties of epoxy composites,” *Carbon*, vol. 50, no. 15, pp. 5380–5386, 2012.

[66] B. Ahmadi-Moghadam and F. Taheri, “Fracture and toughening mechanisms of GNP-based nanocomposites in modes I and II fracture,” *Engineering Fracture Mechanics*, vol. 131, pp. 329–339, 2014.

[67] A. Hernández-Pérez, F. Avilés, A. May-Pat, A. Valadez-González, P. J. Herrera-Franco, and P. Bartolo-Pérez, “Effective properties of multiwalled carbon nanotube/epoxy composites using two different tubes,” *Composites Science and Technology*, vol. 68, no. 6, pp. 1422–1431, 2008.

[68] J. Cha, G. H. Jun, J. K. Park, J. C. Kim, H. J. Ryu, and S. H. Hong, “Improvement of modulus, strength and fracture toughness of CNT/Epoxy nanocomposites through the functionalization of carbon nanotubes,” *Composites Part B: Engineering*, vol. 129, pp. 169–179, 2017.

[69] J. Cha, J. Kim, S. Ryu, and S. H. Hong, “Comparison to mechanical properties of epoxy nanocomposites reinforced by functionalized carbon nanotubes and graphene nanoplatelets,” *Composites Part B: Engineering*, vol. 162, no. July 2018, pp. 283–288, 2019.

[70] A. Bisht, K. Dasgupta, and D. Lahiri, “Effect of graphene and CNT reinforcement on mechanical and thermomechanical behavior of epoxy—A comparative study,” *Journal of Applied Polymer Science*, vol. 135, no. 14, pp. 1–11, 2018.

[71] N. Domun, K. R. Paton, H. Hadavinia, T. Sainsbury, T. Zhang, and H. Mohamud, “Enhancement of fracture toughness of epoxy nanocomposites by combining nanotubes and nanosheets as fillers,” *Materials*, vol. 10, no. 10, 2017.

[72] A. Zeinedini, M. M. Shokrieh, and A. Ebrahimi, “The effect of agglomeration on the fracture toughness of CNTs-reinforced nanocomposites,” *Theoretical and Applied Fracture Mechanics*, vol. 94, no. November 2017, pp. 84–94, 2018.

[73] ISO 13586:2000, “Plastic – Determination of Fracture Toughness (GIC and KIC) – Linear Elastic Fracture Mechanics (LEFM) Approach,” *61010-1 © Iec:2001*, vol. 1, p. 16, 2000-03.

[74] H. EPIKOTE, “[DATASHEET] Epikote Resin 862/ Epikure Curing Agent W System,” pp. 1–11, 2016.

[75] M. Quaresimin, K. Schulte, M. Zappalorto, and S. Chandrasekaran, “Toughening mechanisms in polymer nanocomposites: From experiments to modelling,” *Composites Science and Technology*, vol. 123, no. October 2017, pp. 187–204, 2016.

[76] S. Chandrasekaran, N. Sato, F. Tölle, R. Mülhaupt, B. Fiedler, and K. Schulte, “Fracture toughness and failure mechanism of graphene based epoxy composites,” *Composites Science and Technology*, vol. 97, pp. 90–99, 2014.

[77] S. Chatterjee, F. Nafezarefi, N. H. Tai, L. Schlagenhauf, F. A. Nüesch, and B. T. Chu, “Size and synergy effects of nanofiller hybrids including graphene nanoplatelets and carbon nanotubes in mechanical properties of epoxy composites,” *Carbon*, vol. 50, no. 15, pp. 5380–5386, 2012.

[78] Y. Liu, C. Ramirez, L. Zhang, W. Wu, and N. P. Padture, “In situ direct observation of toughening in isotropic nanocomposites of alumina ceramic and multiwall carbon nanotubes,” *Acta Materialia*, vol. 127, pp. 203–210, 2017.

[79] P. H. Wang, S. Sarkar, P. Gulgunje, N. Verghese, and S. Kumar, “Fracture mechanism

of high impact strength polypropylene containing carbon nanotubes," *Polymer (United Kingdom)*, vol. 151, pp. 287–298, 2018.

[80] C. V. Opelt, D. Becker, C. M. Lepienski, and L. A. Coelho, "Reinforcement and toughening mechanisms in polymer nanocomposites - Carbon nanotubes and aluminum oxide," *Composites Part B: Engineering*, vol. 75, pp. 119–126, 2015.

[81] Q. Liu, S. V. Lomov, and L. Gorbatikh, "The interplay between multiple toughening mechanisms in nanocomposites with spatially distributed and oriented carbon nanotubes as revealed by dual-scale simulations," *Carbon*, vol. 142, pp. 141–149, 2019.

[82] M. Li, M. Tsujimura, and M. Sakai, "Crack-face grain interlocking/bridging of a polycrystalline graphite: the role in mixed mode fracture," *Carbon*, vol. 37, no. 10, pp. 1633–1639, 1999.

[83] S. Cui, Z. Lu, and Z. Yang, "Effect of interlocking structure on mechanical properties of bio-inspired nacreous composites," *Composite Structures*, vol. 226, no. July, p. 111260, 2019.

[84] Q. Liu, S. V. Lomov, and L. Gorbatikh, "The interplay between multiple toughening mechanisms in nanocomposites with spatially distributed and oriented carbon nanotubes as revealed by dual-scale simulations," *Carbon*, vol. 142, pp. 141–149, 2019.

[85] N. Shirodkar, S. Cheng, and G. D. Seidel, "Enhancement of mode i fracture toughness properties of epoxy reinforced with graphene nanoplatelets and carbon nanotubes," *Composites Part B: Engineering*, vol. 224, p. 109177, 2021.

[86] J. Cha, J. Kim, S. Ryu, and S. H. Hong, "Comparison to mechanical properties of epoxy nanocomposites reinforced by functionalized carbon nanotubes and graphene

nanoplatelets," *Composites Part B: Engineering*, vol. 162, no. November 2018, pp. 283–288, 2019.

[87] M. Hayes, D. Edwards, and A. Shah, *Fractography in Failure Analysis of Polymers*. 2015.

[88] S. K. Maiti, *Fracture Mechanics: Fundamentals and Applications Surjya Kumar Maiti*, vol. 41. 2016.

[89] A. Patterson, C. Chadha, I. Jasiuk, and J. Allison, "Design and repeatability analysis of desktop tool for rapid pre-cracking of notched ductile plastic fracture specimens," *Engineering Fracture Mechanics*, vol. 217, p. 106536, 07 2019.

[90] J. M. De Souza, H. N. Yoshimura, F. M. Peres, and C. G. Schön, "Effect of sample pre-cracking method and notch geometry in plane strain fracture toughness tests as applied to a PMMA resin," *Polymer Testing*, vol. 31, no. 6, pp. 834–840, 2012.

[91] A. Kamal, A. H. Elsheikh, and E. Showaib, "Pre-Cracking techniques of polymeric materials: An overview," *IOP Conference Series: Materials Science and Engineering*, vol. 973, no. 1, 2020.

[92] A. Salazar, Y. Patel, and J. G. Williams, "Influence of crack sharpness on the fracture toughness of epoxy resins," *13th International Conference on Fracture 2013, ICF 2013*, vol. 5, pp. 4057–4066, 2013.

[93] E. Haddadi, N. Choupani, and F. Abbasi, "Investigation on the effect of different pre-cracking methods on fracture toughness of RT-PMMA," *Latin American Journal of Solids and Structures*, vol. 13, no. 11, pp. 2012–2026, 2016.

[94] X. Keqin, Y. Lin, and K. Yuk Sum, "Effects of pre-cracking methods on fracture

behaviour of an Araldite-F epoxy and its rubber-modified systems," vol. 33, no. 11, pp. 1573–4803, 1998.

[95] N. Kuppusamy and R. A. Tomlinson, "Repeatable pre-cracking preparation for fracture testing of polymeric materials," *Engineering Fracture Mechanics*, vol. 152, pp. 81–87, 2016.

[96] G. D. Seidel and N. Shirodkar, *Exploring Possible Synergy Between Carbon-Based Nanofiller Reinforcements with Regards to Fracture Toughness Enhancement in Dual Filler Epoxy Nanocomposites.*

[97] N. Shirodkar, S. Rocker, and G. D. Seidel, "Strain and damage sensing of polymer bonded mock energetics via piezoresistivity from carbon nanotube networks," *Smart Materials and Structures*, vol. 28, no. 10, p. 104006, 2019.

[98] N. Shirodkar and G. D. Seidel, *Experimental Investigation of Self-Sensing Mock Polymer-Bonded Energetic Nanocomposites Under Cyclic Compressive Loads.*

[99] N. Shirodkar and G. D. Seidel, *Strain and Damage Sensing in Polymer-Bonded Energetics through Piezoresistive MWCNT Networks.*

[100] W. F. Brown and J. E. Srawley, "Plane Strain Crack Toughness Testing of High Strength Metallic Materials," *ASTM STP*, pp. 1–1–129, 1966.

[101] K. Hollmann and H. T. Hahn, "Plane-strain fracture toughness of epoxies at different loading rates," *Polymer Engineering Science*, vol. 29, no. 8, pp. 523–530, 1989.

[102] Q. G. Quino, "Characterization of fracture toughness of epoxy resin after hygrothermal aging," 2013.

[103] S. P. Lynch, R. J. Wanhill, R. T. Byrnes, and G. H. Bray, *Fracture toughness and fracture modes of aerospace aluminum-lithium alloys.* Elsevier Inc., 2013.

[104] D. B. Lee, T. Ikeda, N. Miyazaki, and N. S. Choi, "Effect of bond thickness on the fracture toughness of adhesive joints," *Journal of Engineering Materials and Technology, Transactions of the ASME*, vol. 126, no. 1, pp. 14–18, 2004.

[105] J. Jamali, Y. Fan, and J. T. Wood, "The mixed-mode fracture behavior of epoxy by the compact tension shear test," *International Journal of Adhesion and Adhesives*, vol. 63, pp. 79–86, 2015.

[106] F. Ren, J. J. A. Wang, and W. D. Bertelsen, "Fractographic study of epoxy under mode I and mixed mode I/III loading," *Materials Science and Engineering A*, vol. 532, pp. 449–455, 2012.

[107] J. Karami, M. R. Ayatollahi, and B. Saboori, "Experimental fracture investigation of CNT/epoxy nanocomposite under mixed mode II/III loading conditions," *Fatigue and Fracture of Engineering Materials and Structures*, vol. 43, no. 5, pp. 879–892, 2020.

[108] B. Saboori and M. R. Ayatollahi, "Experimental fracture study of mwcnt/epoxy nanocomposites under the combined out-of-plane shear and tensile loading," *Polymer Testing*, vol. 59, pp. 193–202, 2017.

[109] R. Guillén-Rujano, J. J. Ku-Herrera, and A. Hernández-Pérez, "Mode III Fracture Toughness Measurement Using the Transverse Shear Cracked Plate Specimen," *Experimental Mechanics*, vol. 61, no. 9, pp. 1419–1430, 2021.

[110] P. Poapongsakorn, A. Wiangkham, P. Aengchuan, N. Noraphaiphipaksa, and C. Kanchanomai, "Time-dependent fracture of epoxy resin under mixed-mode I/III loading," *Theoretical and Applied Fracture Mechanics*, vol. 106, no. June 2019, p. 102445, 2020.

[111] E. M. Arruda, M. C. Boyce, and R. Jayachandran, "Effects of strain rate, temperature

and thermomechanical coupling on the finite strain deformation of glassy polymers," *Mechanics of Materials*, vol. 19, no. 2-3, pp. 193–212, 1995.

[112] P. B. Bowden and J. A. Jukes, "The plastic flow of isotropic polymers," *Journal of Materials Science*, vol. 7, no. 1, pp. 52–63, 1972.

[113] D. R. Drodge, D. M. Williamson, S. J. Palmer, W. G. Proud, and R. K. Govier, "The mechanical response of a pbx and binder: Combining results across the strain-rate and frequency domains," *Journal of Physics D: Applied Physics*, vol. 43, no. 33, 2010.

[114] J. E. Balzer, C. R. Siviour, S. M. Walley, W. G. Proud, and J. E. Field, "Behaviour of ammonium perchlorate-based propellants and a polymer-bonded explosive under impact loading," *Proceedings of the Royal Society A: Mathematical, Physical and Engineering Sciences*, vol. 460, no. 2043, pp. 781–806, 2004.

[115] S. Kim, A. Barua, Y. Horie, and M. Zhou, "Ignition probability of polymer-bonded explosives accounting for multiple sources of material stochasticity," *Journal of Applied Physics*, vol. 115, no. 17, 2014.

[116] J. Hunley, "The history of solid-propellant rocketry - what we do and do not know," *35th Joint Propulsion Conference and Exhibit*, 1999.

[117] E. C. Sengezer and G. D. Seidel, "Structural health monitoring of nanocomposite bonded energetic materials through piezoresistive response," *AIAA Journal*, vol. 56, no. 3, pp. 1225–1238, 2018.

[118] C. R. Siviour, P. R. Laity, W. G. Proud, J. E. Field, D. Porter, P. D. Church, P. Gould, and W. Huntingdon-Thresher, "High strain rate properties of a polymer-bonded sugar: Their dependence on applied and internal constraints," *Proceedings of the Royal Society*

A: Mathematical, Physical and Engineering Sciences, vol. 464, no. 2093, pp. 1229–1255, 2008.

[119] N. Shirodkar, S. Rocker, and G. D. Seidel, "Structural health monitoring of solid rocket propellants using piezoresistive properties of dispersed carbon nano-tube sensing networks," no. 51944, p. V001T01A022, 2018. 10.1115/SMASIS2018-8250.

[120] S. J. P. Palmer, J. E. Field, and J. M. Huntley, "Deformation, strengths and strains to failure of polymer bonded explosives," *Proceedings: Mathematical and Physical Sciences*, vol. 440, no. 1909, pp. 399–419, 1993. 1. Explains how rubbery elastomer PBX fails 2. Shows strength of specimens with micronzed particles is higher than coarse grains.

[121] P. J. Schilling, B. P. R. Karedla, A. K. Tatiparthi, M. A. Verges, and P. D. Herrington, "X-ray computed microtomography of internal damage in fiber reinforced polymer matrix composites," *Composites Science and Technology*, vol. 65, no. 14, pp. 2071–2078, 2005.

[122] K. T. Tan, N. Watanabe, and Y. Iwahori, "X-ray radiography and micro-computed tomography examination of damage characteristics in stitched composites subjected to impact loading," *Composites Part B: Engineering*, vol. 42, no. 4, pp. 874–884, 2011.

[123] E. C. Sengezer, G. D. Seidel, and R. J. Bodnar, "Anisotropic piezoresistivity characteristics of aligned carbon nanotube-polymer nanocomposites," *Smart Materials and Structures*, vol. 26, no. 9, 2017.

[124] N. Prakash and G. D. Seidel, "Effects of microscale damage evolution on piezoresistive sensing in nanocomposite bonded explosives under dynamic loading via electromechanical peridynamics effects of microscale damage evolution on

piezoresistive sensing in nanocomposite bonded explosive," *Modelling and Simulation in Materials Science and Engineering*, vol. 26, no. 1, p. 32, 2017.

[125] S. N. Rocker, N. Shirodkar, T. A. McCoy, and G. D. Seidel, "Electro-mechanical response of polymer bonded surrogate energetic materials with carbon nanotube sensing networks for structural health monitoring applications bt - mechanics of composite, hybrid and multifunctional materials, volume 5," (Cham), pp. 185–193, Springer International Publishing, 2019.

[126] A. Chaurasia, E. Sengezer, K. Talamadupula, S. Povolny, and G. Seidel, "Experimental characterization and computational modeling of deformation and damage sensing through the piezoresistive response of nanocomposite bonded surrogate energetic materials," *Journal of Multifunctional Composites*, vol. 2, no. 4, pp. 227–253, 2014.

[127] D. A. Price R Clairmont Jr I Jaffe, "Explosive behavior of ammonium perchlorate donna price," 0.

[128] L. Gao, T. W. Chou, E. T. Thostenson, Z. Zhang, and M. Coulaud, "In situ sensing of impact damage in epoxy/glass fiber composites using percolating carbon nanotube networks," *Carbon*, vol. 49, no. 10, pp. 3382–3385, 2011.

[129] J. R. Bautista-Quijanoa, F. Avilésa, J. O. Aguilara, and A. Tapia, "Strain sensing capabilities of a piezoresistive mwcnt-polysulfone film," *Sensors and Actuators, A: Physical*, vol. 159, no. 2, pp. 135–140, 2010.

[130] S. Nag-Chowdhury, H. Bellegou, I. Pillin, M. Castro, P. Longrais, and J. F. Feller, "Non-intrusive health monitoring of infused composites with embedded carbon quantum piezo-resistive sensors," *Composites Science and Technology*, vol. 123, pp. 286–294, 2016.

[131] X. Chen, X. Zheng, J.-K. Kim, X. Li, and D.-W. Lee, “Investigation of graphene piezoresistors for use as strain gauge sensors,” *Journal of Vacuum Science Technology B, Nanotechnology and Microelectronics: Materials, Processing, Measurement, and Phenomena*, vol. 29, no. 6, p. 06FE01, 2011.

[132] M. A. Daniel, “Polyurethane binder systems for polymer bonded explosives,” *Weapons Systems Division Defence Science and Technology Organisation DSTO-GD-0492*, p. 34, 2006. PBX ratio ref.

[133] P. A. Kakavas, “Mechanical properties of propellant composite materials reinforced with ammonium perchlorate particles,” *International Journal of Solids and Structures*, vol. 51, no. 10, pp. 2019–2026, 2014. This paper is a reference to show AP is being used as a solid rocket propellant in many works. Also gives some mix ratios and mechanical characterization techniques.

[134] S. Jain, M. Maurya, N. S, P. P. Singh, K. K. Radhakrishnan, and B. Bhattacharya, *Size and Shape of Ammonium Perchlorate and their Influence on Properties of Composite Propellant*, vol. 59. 5 2009. Good paper for AP.

[135] R. F. Gould, C. Boyars, and K. Klager, “Propellants manufacture, hazards, and testing, copyright, advances in chemistry series, foreword,” in *Propellants Manufacture, Hazards, and Testing* (G. R. F., ed.), vol. 88 of *Advances in Chemistry*, pp. i–vi, AMERICAN CHEMICAL SOCIETY, 6 1969. doi:10.1021/ba-1969-0088.fw001.

[136] F. Kelley, “Solid propellant mechanical properties testing, failure criteria, and aging,” in *Propellants Manufacture, Hazards, and Testing*, vol. 88 of *Advances in Chemistry*, pp. 188–243 SE – 8, AMERICAN CHEMICAL SOCIETY, 6 1969. doi:10.1021/ba-1969-0088.ch008.

[137] G. A. Fluke, “Composite solid propellant processing techniques,” in *Propellants Manufacture, Hazards, and Testing*, vol. 88 of *Advances in Chemistry*, pp. 165–187 SE – 7, AMERICAN CHEMICAL SOCIETY, 6 1969. doi:10.1021/ba-1969-0088.ch007.

[138] A. D. 02a, “Standard test method for tensile properties of plastics,” *ASTM D 638 -02a*, vol. 08, pp. 46–58, 2003.

[139] A. D695, “Standard test method for compressive properties of rigid plastics,” vol. i, pp. 1–8, 2018.

[140] J. Cho, M. S. Joshi, and C. T. Sun, “Effect of inclusion size on mechanical properties of polymeric composites with micro and nano particles,” *Composites Science and Technology*, vol. 66, no. 13, pp. 1941–1952, 2006.

[141] D. Lee, H. P. Hong, C. J. Lee, C. W. Park, and N. K. Min, “Microfabrication and characterization of spray-coated single-wall carbon nanotube film strain gauges,” *Nanotechnology*, vol. 22, no. 45, pp. 1–7, 2011.

[142] S.-h. Jang and H. Yin, “Characterization and modeling of the effective electrical conductivity of a carbon nanotube / polymer composite containing chain-structured ferromagnetic particles,” 2017.

[143] B. Han, Y. Wang, S. Dong, and L. Zhang, “Smart concretes and structures : A review,” vol. 26, no. 11, pp. 1303–1345, 2015.

[144] S. Wang and D. D. L. Chung, “Self-sensing of flexural strain and damage in carbon fiber polymer-matrix composite by electrical resistance measurement,” *Carbon*, vol. 44, no. 13, pp. 2739–2751, 2006.

[145] J. E. Balzer, C. R. Siviour, S. M. Walley, W. G. Proud, and J. E. Field, “Behaviour of ammonium perchlorate-based propellants and a polymer-bonded explosive under

impact loading," *Proceedings of the Royal Society A: Mathematical, Physical and Engineering Sciences*, vol. 460, no. 2043, pp. 781–806, 2004.

[146] S. J. P. Palmer, J. E. Field, and J. M. Huntley, "Deformation, Strengths and Strains to Failure of Polymer Bonded Explosives," *Proceedings: Mathematical and Physical Sciences*, vol. 440, no. 1909, pp. 399–419, 1993.

[147] Y. K. Adde, Alemayehu, G. Lulseged, Y. Adde, L. Alemayehu, and G. Solomon, "Design of a solid rocket propulsion system," *International Journal of Aeronautical Science Aerospace Research*, pp. 224–229, 07 2020.

[148] O. Yilmaz, B. Kuran, and G. O. Özgen, "Reliability assessment of solid-propellant rocket motors under storage and transportation loads," *Journal of Spacecraft and Rockets*, vol. 54, no. 6, pp. 1356–1366, 2017.

[149] C. Leach, D. Debenham, J. Kelly, and K. Gillespie, "Factors affecting the vulnerability of composite lova gun propellants," in *International Symposium on Energetic Materials Technology Proceedings, The American Defense Preparedness Association*, pp. 132–138, 1995.

[150] P. Braithwaite, G. Dixon, M. Rose, and R. Wardle, "The promise of energetic tpe gun propellants-from notebook to full scale verification," in *NDIA 37th Annual Gun and Ammunition Symposium. San Diego: NDIA*, vol. 4, pp. 15–18, 2002.

[151] S. lin Pang, X. Chen, J. sheng Xu, G. tu Zhaori, and H. Y. Du, "Analysis on damage characteristics and detonation performance of solid rocket engine charge subjected to jet," *Defence Technology*, no. xxxx, 2021.

[152] Propulsion and Energetics Panel Working Group, *Structural Assessment of Solid Propellant Grains*. No. December, 1997.

[153] F. C. CHund, "Nondestructive Testing of Solid Propellant Missile Motors," *Symposium on Recent Developments in Nondestructive Testing of Missiles and Rockets*, pp. 62–62–23, 2009.

[154] K. T. Tan, N. Watanabe, and Y. Iwahori, "X-ray radiography and micro-computed tomography examination of damage characteristics in stitched composites subjected to impact loading," *Composites Part B: Engineering*, vol. 42, no. 4, pp. 874–884, 2011.

[155] J. O. Mares, J. K. Miller, N. D. Sharp, D. S. Moore, D. E. Adams, L. J. Groven, J. F. Rhoads, and S. F. Son, "Thermal and mechanical response of PBX 9501 under contact excitation," *Journal of Applied Physics*, vol. 113, no. 8, 2013.

[156] S. W. Doebling, C. R. Farrar, M. B. Prime, *et al.*, "A summary review of vibration-based damage identification methods," *Shock and vibration digest*, vol. 30, no. 2, pp. 91–105, 1998.

[157] E. C. Sengezer and G. D. Seidel, "Structural health monitoring of nanocomposite bonded energetic materials through piezoresistive response," *AIAA Journal*, vol. 56, no. 3, pp. 1225–1238, 2018.

[158] E. C. Sengezer, G. D. Seidel, and R. J. Bodnar, "Anisotropic piezoresistivity characteristics of aligned carbon nanotube-polymer nanocomposites," *Smart Materials and Structures*, vol. 26, p. 095027, aug 2017.

[159] S. N. Rocker, N. Shirodkar, T. A. McCoy, and G. D. Seidel, "Electro-mechanical response of polymer bonded surrogate energetic materials with carbon nanotube sensing networks for structural health monitoring applications," in *Mechanics of Composite, Hybrid and Multifunctional Materials, Volume 5* (P. R. Thakre, R. P. Singh, and G. Slipher, eds.), (Cham), pp. 185–193, Springer International Publishing, 2019.

[160] *Structural Health Monitoring of Solid Rocket Propellants Using Piezoresistive Properties of Dispersed Carbon Nano-Tube Sensing Networks*, vol. Volume 1: Development and Characterization of Multifunctional Materials; Modeling, Simulation, and Control of Adaptive Systems; Integrated System Design and Implementation of *Smart Materials, Adaptive Structures and Intelligent Systems*, 09 2018. V001T01A022.

[161] W. Chung-Lin, H.-C. Lin, C.-H. Huang, M.-C. Yip, and W. Fang, "Mechanical Properties of PDMS/CNTs Nanocomposites," *MRS Proceedings*, vol. 1056, pp. 9–14, 2008.

[162] J. Du, L. Wang, Y. Shi, F. Zhang, S. Hu, P. Liu, A. Li, and J. Chen, "Optimized cnt-pdms flexible composite for attachable health-care device," *Sensors (Switzerland)*, vol. 20, no. 16, pp. 1–13, 2020.

[163] R. Ariati, F. Sales, A. Souza, R. A. Lima, and J. Ribeiro, "Polydimethylsiloxane composites characterization and its applications: A review," *Polymers*, vol. 13, no. 23, pp. 1–21, 2021.

[164] I. D. Johnston, D. K. McCluskey, C. K. Tan, and M. C. Tracey, "Mechanical characterization of bulk Sylgard 184 for microfluidics and microengineering," *Journal of Micromechanics and Microengineering*, vol. 24, no. 3, 2014.

[165] S. J. Povolny, G. D. Seidel, and C. Tallon, "Numerical investigation of thermomechanical response of multiscale porous Ultra-High Temperature Ceramics," *Ceramics International*, vol. 48, no. 8, pp. 11502–11517, 2022.

[166] S. J. Povolny, G. D. Seidel, and C. Tallon, "Numerical Brazilian disk testing of multiscale porous Ultra-High Temperature Ceramics," *International Journal of Solids and Structures*, vol. 234-235, no. June 2021, p. 111262, 2022.

[167] S. J. Lim, H. S. Lim, Y. Joo, and D. Y. Jeon, "Impact of MWCNT concentration on the piezo-impedance response of porous MWCNT/PDMS composites," *Sensors and Actuators, A: Physical*, vol. 315, p. 112332, 2020.

[168] K. Park, P. Tran, N. Deaton, and J. P. Desai, "Multi-walled Carbon Nanotube (MWCNT)/PDMS-based Flexible Sensor for Medical Applications," *2019 International Symposium on Medical Robotics, ISMR 2019*, 2019.

[169] J. Shao, L. Yu, A. L. Skov, and A. E. Daugaard, "Highly stretchable conductive MWCNT-PDMS composite with self-enhanced conductivity," *Journal of Materials Chemistry C*, vol. 8, no. 38, pp. 13389–13395, 2020.

[170] K. Huang, H. Ning, N. Hu, F. Liu, X. Wu, S. Wang, Y. Liu, R. Zou, W. Yuan, Alamusi, and L. Wu, "Ultrasensitive MWCNT/PDMS composite strain sensor fabricated by laser ablation process," *Composites Science and Technology*, vol. 192, no. December 2019, p. 108105, 2020.

[171] W. Bauhofer and J. Z. Kovacs, "A review and analysis of electrical percolation in carbon nanotube polymer composites," *Composites Science and Technology*, vol. 69, no. 10, pp. 1486–1498, 2009.

[172] R. Ramalingame, D. Rajendran, A. Lakshmanan, and O. Kanoun, "Effect of organic solvent on MWCNT-PDMS nanocomposite based capacitive pressure sensors," *2018 15th International Multi-Conference on Systems, Signals and Devices, SSD 2018*, pp. 1208–1211, 2018.

[173] J. Lu, M. Lu, A. Bermak, and Y. K. Lee, "Study of piezoresistance effect of carbon nanotube-PDMS composite materials for nanosensors," *2007 7th IEEE International Conference on Nanotechnology - IEEE-NANO 2007, Proceedings*, pp. 1240–1243, 2007.

[174] C. C. Perry, “The resistance strain gage revisited,” *Experimental Mechanics*, vol. 25, no. 1, p. 84, 1985.

[175] A. Chaurasia and G. Seidel, “Computational micromechanics analysis of electron hopping and interfacial damage induced piezoresistive response in carbon nanotube-polymer nanocomposites subjected to cyclic loading conditions,” *European Journal of Mechanics - A/Solids*, vol. 64, pp. 112 – 130, 2017.

[176] N. Prakash and G. D. Seidel, “Effects of microscale damage evolution on piezoresistive sensing in nanocomposite bonded explosives under dynamic loading via electromechanical peridynamics,” *Modelling and Simulation in Materials Science and Engineering*, vol. 26, no. 1, p. 015003, 2018.

[177] K. K. Talamadupula, S. J. Povolny, N. Prakash, and G. D. Seidel, “Mesoscale strain and damage sensing in nanocomposite bonded energetic materials under low velocity impact with frictional heating via peridynamics,” *Modelling and Simulation in Materials Science and Engineering*, vol. 28, p. 085011, nov 2020.

[178] K. K. Talamadupula, S. J. Povolny, N. Prakash, and G. D. Seidel, “Piezoresistive detection of simulated hotspots and the effects of low velocity impact at the mesoscale in nanocomposite bonded energetic materials via multiphysics peridynamics modeling,” *Computational Materials Science*, vol. 188, pp. 110211 – 30 pgs, 2021.

[179] N. Prakash and G. D. Seidel, “Computational electromechanical peridynamics modeling of strain and damage sensing in nanocomposite bonded explosive materials (ncbx),” *Engineering Fracture Mechanics*, vol. 177, pp. 180–202, 2017.

[180] A. K. Chaurasia, E. C. Sengezer, K. K. Talamadupula, S. Povolny, and G. D. Seidel, “Experimental characterization and computational modeling of deformation

and damage sensing through the piezoresistive response of nanocomposite bonded surrogate energetic materials," *Journal of Multifunctional Composites*, vol. 2, no. 4, pp. 227–253, 2014.

[181] M. Villar, M. Bibbó, and E. Vallés, "Influence of pendant chains on mechanical properties of model poly(dimethylsiloxane) networks. 1. analysis of the molecular structure of the network," *Macromolecules*, vol. 29, no. 11, pp. 4072–4080, 1996. cited By 32.

[182] W. S. Lee, K. S. Yeo, A. Andriyana, Y. G. Shee, and F. R. Mahamd Adikan, "Effect of cyclic compression and curing agent concentration on the stabilization of mechanical properties of PDMS elastomer," *Materials and Design*, vol. 96, pp. 470–475, 2016.

[183] G. Chatzigeorgiou, G. D. Seidel, and D. C. Lagoudas, "Effective mechanical properties of "fuzzy fiber" composites," *Composites Part B: Engineering*, vol. 43, no. 6, pp. 2577–2593, 2012.

[184] M. R. Gude, S. G. Prolongo, and A. Ureña, "Toughening effect of carbon nanotubes and carbon nanofibres in epoxy adhesives for joining carbon fibre laminates," *International journal of adhesion and adhesives*, vol. 62, pp. 139–145, 2015.

Appendices

Appendix A

Compilation of Normalized Nanocomposite Epoxy Fracture Toughness Values

Table A.1: Sources and value of the normalized critical stress intensity factors, K_{IC}, of reinforced epoxies obtained from the literature and plotted in Figure 1.1

Author(s)	**Material System**	**Nanoparticle Weight Concentration (%)**	**Normalized K_{IC}**
Sun et al (2007)	Epoxy-Pristine SWCNTs	1	1.035
	Epoxy-Functionalized SWCNTs (ammonia)	1	1.17
Chatterjee et al (2012)	CNT-Epoxy	0.5	1.8
	25 um GNP-Epoxy	0.5	1.6
	1:9 CNT:GNP-Epoxy	0.5	1.46
	9:1 CNT:GNP-Epoxy	0.5	1.79
	1:5 CNT:GNP-Epoxy	0.5	1.24

	5:1 CNT:GNP-Epoxy	0.5	1.46
	1:3 CNT-GNP-Epoxy	0.5	1.7
	3:1 CNT:GNP-Epoxy	0.5	1.7
Chatterjee et al (2012)	5 um GNP-Epoxy	0.1, 1, 2	1.02, 1.22, 1.59
	25 um GNP-Epoxy	0.1, 1, 2	1.52, 1.7, 1.8
Ahmadi-Mohgadum et al (2014)	25 um GNP-Epoxy	0.5, 1, 2	1.24, 1.37, 1.68
	2:3 (25um GNP):CNT-Epoxy	0.5	1.32
	7:3 GNP-CNT-Epoxy	1	1.62
	1.7:0.3 GNP-CNT-Epoxy	2	1.75
Hernandez-Perez et al (2007)	CNT-Epoxy	1	1.33
Zaman et al (2011)	GNP-Epoxy	0.25, 1, 4	1.42, 1.08, 1.91
Ayatollahi et al (2010)	MWCNT-Epoxy	0.1, 0.5, 1	1.15, 1.263, 1.192
Zhou et al (2007)	CNT-Epoxy	0.1, 0.2, 0.3, 0.4	1.17, 1.25, 1.32, 1.07
Shokrieh et al (2014)	GNP-Epoxy	0.5	1.152
Hsieh et al (2011)	MWCNT-Epoxy	0.1, 0.2, 0.5	1.23, 1.25, 1.42
Rafiee et al (2009)	SWCNT-Epoxy	0.1	1.12

	MWCNT-Epoxy	0.1	1.18
	GPL-Epoxy	0.1	1.467
Gojny et al (2005)	Epoxy-SWCNT	0.05, 0.1, 0.3	1.1, 1.23, 1.12
	Epoxy-DWCNT	0.1, 0.3, 0.5	1.169, 1.30, 1.30
	Epoxy-MWCNT	0.1, 0.3	1.215, 1.23
Kumar et al	GNP-Epoxy	0.1, 0.5	2.42, 3
Cha et al (2017)	Melamine-CNT-Epoxy	1, 2, 3	1.98, 1.95, 2.02
	CNT-Epoxy	0.5, 1, 2, 3	1.4, 1.3, 1.45, 1.51
Zeinedini et al (2018)	CNT-Epoxy	0.1, 0.3, 0.5, 0.7	1.085, 1.13, 1.24, 1.21
Cha et al (2019)	GNP-Epoxy	2	1.49
	Melamine - GNP-Epoxy	2	2.25
Bisht et al (2017)	GNP-Epoxy	0.1, 0.2, 0.3, 0.5, 1	1.4, 1.8, 2, 1.92, 1.32
	CNT-EPoxy	0.1, 0.2, 0.3, 0.5, 1	1.64, 2, 2.28, 2.48, 1.44
Domun et al (2017)	Nitric Acid Functionalized GNP-Epoxy	0.1, 0.25, 0.5, 0.75, 1	1.32, 1.51, 1.4, 1.265, 1.135

Appendix B

Variance to Mean Ratio (VMR)

A new measure is introduced to quantify the reliability of electrical measurements of the energetic nanocomposite samples which are collected using the Agilent A4980 LCR meter. Electro-mechanical sensing tests require the measurement of impedance data of the sample under test (DUT) in conjunction with mechanical strain. Due to the DUT being a bulk material rather than an assembly of electrical components, relatively higher electrical noise is expected in the readings. The amount of noise in the electrical reading depends on a number factors such as: experimental setup, CNT weight concentration, insulation from fixture as well as ambient statics. The nanocomposite samples have a percolation threshold for CNT weight concentration beyond which the electrical reading are much clearer, measurable and repeatable. Through the use of variance to mean ratios (VMRs), the noise in the electrical readings is quantified and a criterion is set for minimum VMRs for a given electrical signal to be deemed as reliable.

B.1 Variance to mean ratio

The variance to mean ratio (VMR) is a simple tool through which the dispersion of a probability distribution can be quantified. The VMR, also referred to as the ”index of dispersion”, is equal to zero when the measured value is constant. It is exactly equal to 1 in a perfect Poisson distribution. If the VMR is >1 then the distribution is deemed to be over dispersed, whereas if the VMR is between zero and 1, then the distribution is deemed to be under-dispersed. In the purview of the electrical-mechanical sensing work presented in this dissertation, the VMR shall be applied to quantify the dispersion of the electrical reading taken for a particular sample at a particular strain level. If the VMR is lesser than 1, the electrical readings will be considered to be stable and reliable, implying that the electrical data gathered for that sample, can be used to characterize material behavior. If the VMR is higher than 1, the electrical readings have a larger scatter and hence the readings may not be reliable and repeatable, implying that the trends seen in electrical responses cannot be associated strongly with the material behavior.

B.2 Procedure to calculate VMRs

For a material sample's electrical readings to be deemed consistent and reliable at a particular strain, the VMR must be under 1. In this work, two types of VMRs are evaluated: unstrained VMR and instantaneous VMR. Unstrained VMR refers to VMR calculated from the electrical readings taken when the sample is not under any mechanical strain. An instantaneous VMR refers to a VMR that is calculated from the electrical readings taken when the sample is subjected to and held at a particular level of strain. Typically, the sample will be subjected to an held to progressively higher levels of strain at which an instantaneous VMR will be calculated. This is done to ensure the reliability of electrical readings as the sample is subjected to various levels of mechanical strain as well as damage.

The following has to be ensured/assumed for a valid VMR calculation.

1. The data collected must be independent data points; meaning, the outcome of one data point must not affect the outcome of the next data point. This is true for the electrical readings gathered for the energetic samples, as long as the readings are taken

at a constant strain level.

2. The distribution of the data must resemble a Poisson distribution. This must be verified for every set of data.
3. The variance and mean must be calculated using the normalized electrical values, and NOT the absolute values.
4. There must be at least 100 data points available to obtain a valid VMR.

The following formula is used to calculate VMRs (unstrained and instantaneous)

$$VMR = \frac{Variance}{Mean} \tag{B.1}$$

To calculate the unstrained VMR, the sample is first laid on a insulating surface—typically a sheet of silicone rubber or a wooden plank. Next, the electrode leads attached to the sample are connected to the LCR meter using banana clips. It must be ensured that before the leads are connected, OPEN and SHORT corrections are performed on the LCR meter and an appropriate cable length correction factor is added (it depends on how long the leads are). The LCR meter must be setup to run at 100 kHz measurement frequency, 2V signal voltage, R-X readings display, and ”short” measurement period. Once the connections and setup are verified, the LCR must be run via the LabView code. R-X data must be acquired for 30 seconds and then stopped. This must be done for each and every sample and material type. The variance and the mean of the data gather must be calculated. The VMR is then calculated by simply dividing the variance by the mean.

To calculate the instantaneous VMRs, the sample must be subjected to a ramp-hold-ramp displacement controlled test. This essentially conducts a mechanical test where the strain is monotonically increased and then held for a stipulated period after which is it increased again. The electrical readings must be gathered in conjunction with the mechanical data. The purpose of the hold phase is to allow gathering of the electrical signals at a constant strain level to fulfil the assumption of independent data points. There are two approaches for gathering data to calculate instantaneous VMRs: electrical data is gathered separately at every hold period or the electrical data is continuously gathered and then the data corresponding to hold period is separated using the associated time stamps. The VMRs can then be calculated using the same procedure as for the unstrained VMRs.

B.3 Unstrained Resistance, Reactance and Impedance Data used for VMR Calculations of PBE Samples

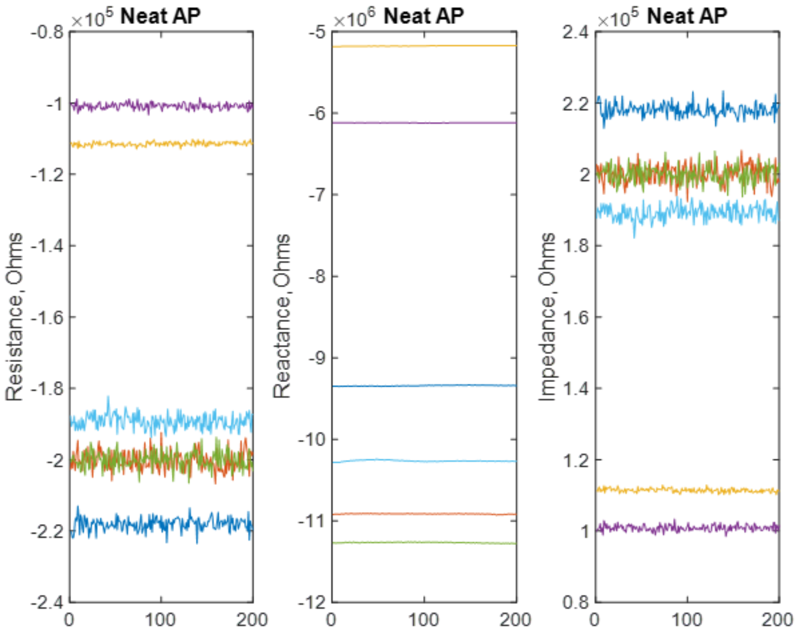

Figure B.1: Unstrained resistance, reactance and impedance for Neat PBE

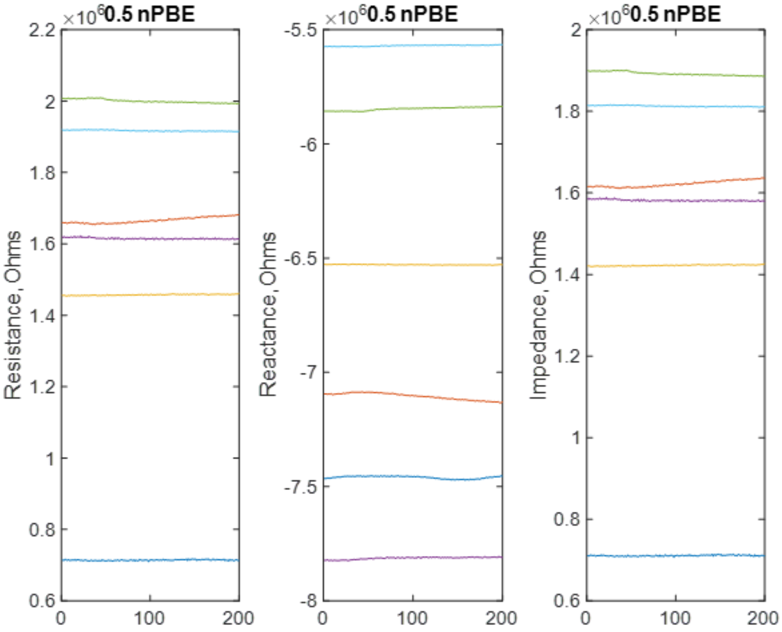

Figure B.2: Unstrained resistance, reactance and impedance for 0.5% nPBE

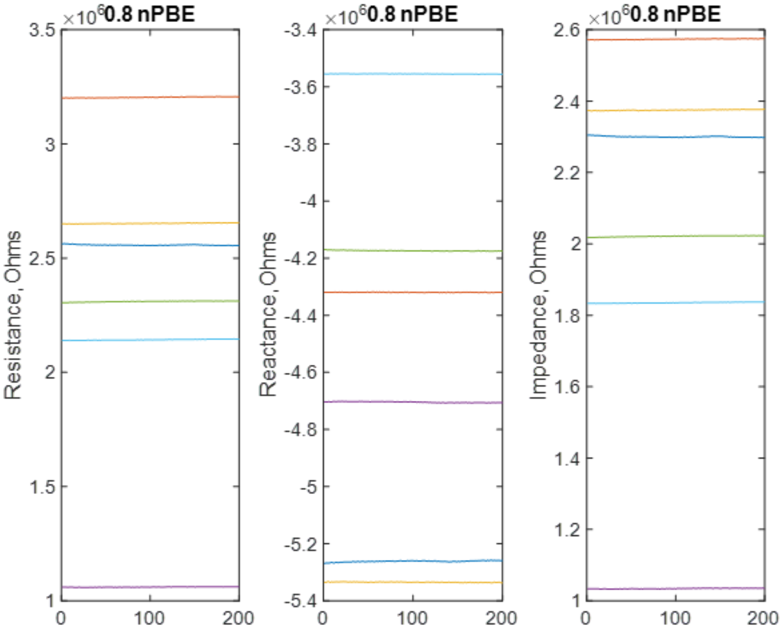

Figure B.3: Unstrained resistance, reactance and impedance for 0.8% nPBE

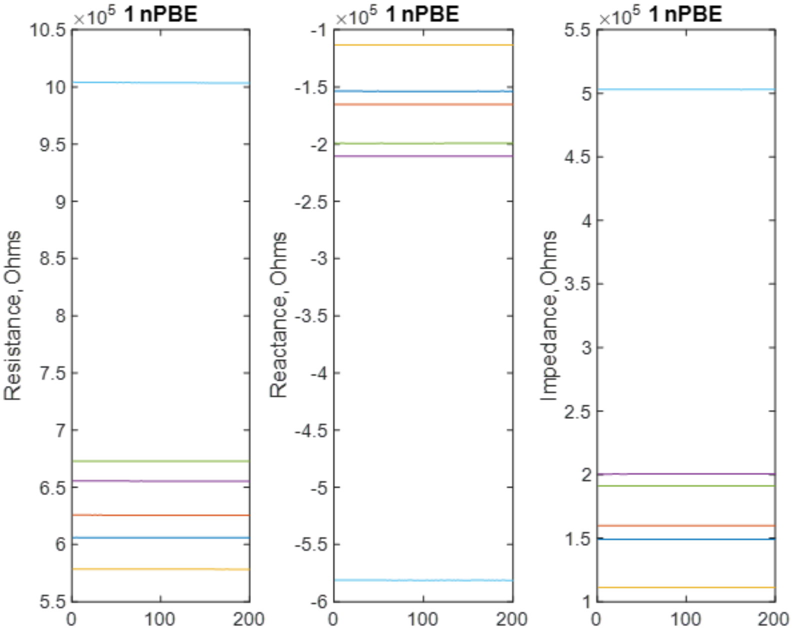

Figure B.4: Unstrained resistance, reactance and impedance for 1% nPBE

Appendix C

Additional Results: Electro-mechanical Sensing

The raw data for all the nanocomposite polymer binder samples that were tested in Chapter 7 have been presented in this section [1].

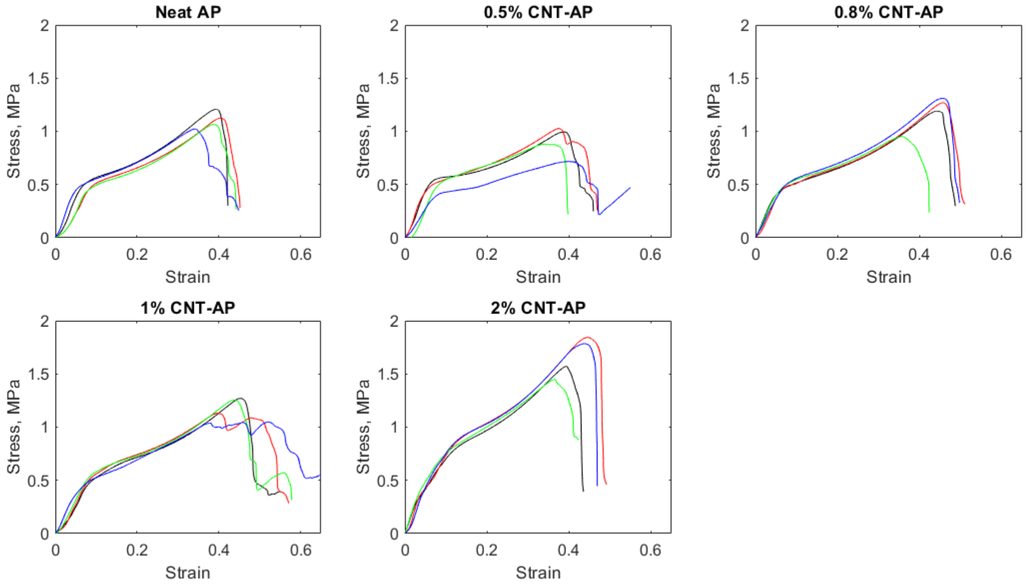

Figure C.1: Stress-strain curves for all the samples tested for the PBE material type.

---

[1] Based on the VMR criterion, only 2% MWCNT concentration was explored for aluminum PBE samples. Hence additional data is not available for other concentrations

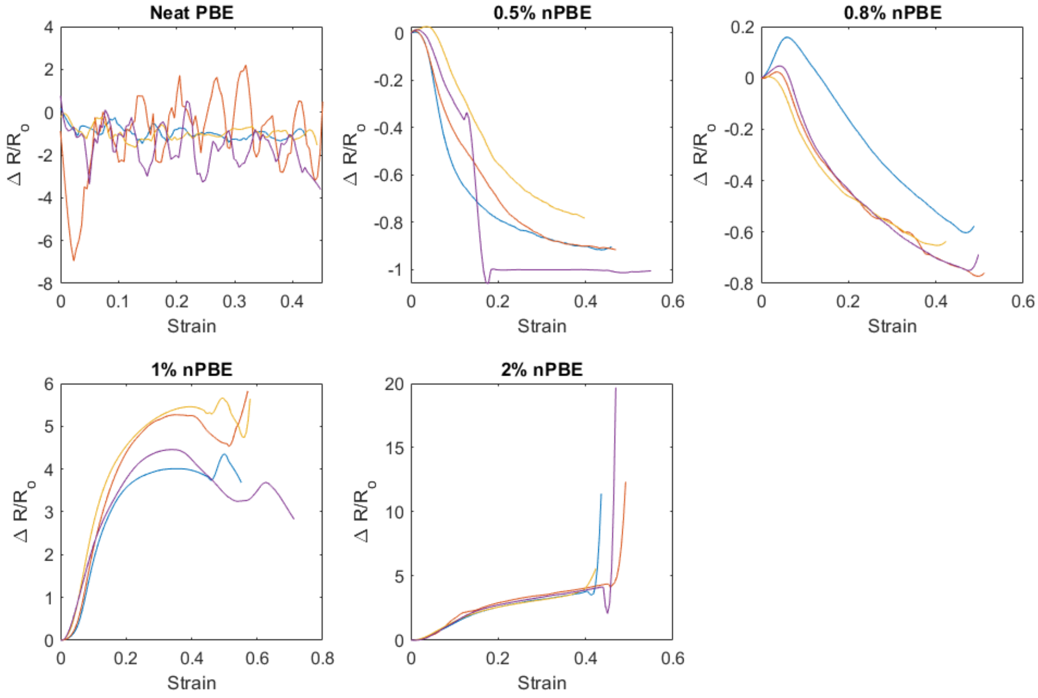

Figure C.2: Change in normalized resistance as a function of strain for all the samples tested for the PBE material type.

Appendix D

Theoretical models correlating change in electrical properties to applied strain

In order to understand the expected behavior of the material during electromechanical sensing, theoretical models based on equations describing the resistance, reactance and impedance as functions of strain and Poisson's ratio were developed. Piezoresistive evolution and piezocapacitive evolution of the materials resistivity and dielectric constant, respectively, were incorporated in to the models to understand the influence these mechanisms may have on the sensing behavior. For this purpose, informed estimates of the piezoresistive coefficient and piezocapacitive coefficient were used (the former obtained by fitting the fabricated material's electrical properties, and the latter obtained from literature for similar materials). The growth/decline of electrical properties due to piezo-evolution is implemented such that it makes physical sense for the test samples considered in this study; i.e the electrical resistivity decreases upon compression of the material, and the dielectric constant increases upon material compression (due to the arrangement of electrodes on the test samples). In addition to the piezo-evolution, the influence of damage was also investigated by incorporating a simple damage evolution for the electrical properties. A continuum damage evolution was used with dummy damage variables, which served to simply demonstrate how the electrical response would be affected if damage occurs. The damage laws also affect the electrical properties such that it made physical sense for the test samples considered in this study; i.e. the electrical resistivity increases with occurrence of damage, while the dielectric constant decreases until it reaches the value of permittivity of free space at full damage.

The initial resistance of a material, when it is not subjected to any mechanical strain, can be defined as follows

$$R = \frac{\rho_o L_o}{A_o}$$

where ρ is the material's initial electrical resistivity, L is the initial length of the conductor (in this study, that translates to the distance between electrodes), and the initial cross-section area. Similarly, the resistance at an i^{th} point in time during testing can be defined using the length, and area at the i^{th} time step. In materials that do not exhibit piezoresistivity, the ρ value can be assumed as a constant or can be evolved using a pieze-evolution law. Thus, a ΔR expression can be derived. The length and area can be expressed using mechanical strain and Poisson's ratio. The end result of this substitution is an equation that describes the change in resistance as a function of strain and Poisson's ratio [45, 46]. To psuedo-simulate the occurence of damage and its subsequent influence on the electrical properties, a simple continuum damage model is used, where the material property is arbitrarily and continually knocked down as the strain increases. This model can be refined significantly, but for the purposes of understanding the electrical behavior under damage, it is sufficient.

Similarly, the initial capacitance of a material, when it is not subjected to any mechanical strain, can be defined as follows

$$C = \frac{\epsilon_r \epsilon_o A_o}{d_o}$$

where ϵ_r is the relative dielectric constant, ϵ_o is the dielectric permittivity of free space, A_o

and d_o are the initial cross section area of the parallel plate capacitor (corresponds to the cross-section area of the test sample) and distance between the plates, respectively (which in this study corresponds to the distance between the two electrodes). The capacitance can further be expressed as in terms of reactance, X which is the imaginary component of AC impedance. Reactance can be defined as

$$X = \frac{-1}{2\pi f C}$$

where f is the measurement frequency. Substituting the expression for Capacitance, C

$$X = \frac{-d_o}{2\pi f \epsilon_r \epsilon_o A_o}$$

Thus reactance is negatively and inversely proportional to capacitance, i.e. a large reactance value would indicate a small capacitance contribution in the total impedance of the sample. Similar to the resistance, the geometric components of the reactance expression can be expressed as strain and Poisson's ratio, and thus an equation expressing the change in reactance as a function of strain and Poisson's ratio can be derived.

Lastly, the change in electrical impedance as function of strain and Poisson's ratio can be calculated using the individual expressions for change in resistance and reactance derived earlier. The electrical impedance is calculated as parallel circuit impedance (based on how the LCR machine choses to derive the real and imaginary components of the impedance). Thus impedance can be defined as

$$Z = \frac{1}{\sqrt{\left(\frac{1}{R}\right)^2 + \left(\frac{1}{X}\right)^2}}$$

By simply substituting the values of the resistance and reactance, the full equation describing the change in impedance as a function of strain and Poisson's ratio can be derived.

Figures D.1, D.2, and D.3 shows the change in resistance, reactance and impedance plotted as a function of compressive strain. The following are the initial parameters used to create the graphs based on the derived models.

1. Strain vector: eps = 0:0.01:0.6;
2. Damage Turns on at 0.4 strain value;
3. Evolution of damage variable, alpha = linspace(0,0.999,N-damonset*100), where N is the length of the strain vector and "damonset" is the value at which damage is activated.
4. Poisson's Ratio v = 0.3;
5. Piezoresistive Coeff H = 0.99;
6. Piezocapacitive Coefficient, θ = 2;
7. Geometrical Constants Length, Lo = 45 mm; Area, Ao = pi*$(19/4)^2$;
8. Trial Electrical Values for Resistance, resistivity and dielectric constant Ro = 100*10^3 kΩ
   ρ = Ao*Ro/Lo (Resistivity at zero strain)
   ϵ = 1.2; (relative dielectric permittivity constant)
   ϵ_{free} = 8.85*10^-15
   Measurement Frequency ω=2*pi*10^5

Based on experimental observations, 60% strain is used as the failure strain, i.e. the sample is fully damaged. The plotted graphs thus show the variation of electrical properties between zero and 60% strain. The solid black line indicates that the piezo-evolution and damage evolution are both turned off. The solid blue line indicates that the piezo-evolution is turned on, but the damage is off. The dashed magenta line indicates that piezo-evolution is off but the damage is turned on. Lastly, the dashed red line indicates that both piezo-evolution and damage evolution are turned on. In the special case of the reactance plot (Figure D.2), the dark green dotted line represents damage evolution and piezo-evolution turned on for the sample which is being compressed beyond full failure, thus representing change in electrical properties due to compression of free space. It can be observed in Figure D.1 that piezo-resistive evolution of resisitivity increases the non-linearity of the electrical response, thus making the material more conductive. However, turning damage on increases the resistance, and thus competes with the piezo-evolution. For the materials under consideration, damage evolution is believed to be more dominant, and hence the total resistance increase after damage initiates. The resistance increases to large values as the material damages more, eventually leading to a theoretical value of infinity at full damage. A similar trend is observed in the reactance, where the piezocapacitive evolution increases the non-linearity in the reactance change, while damage decreases it. Eventually, the reactance values are dominated by the permittivity of free space as damage increases to its maximum value. Compressing a sample beyond full failure, essentially meaning compression free space, only exhibits electrical property variation as a result of geometric changes (change in distance between the electrodes). These responses are combined in the impedance response. Since the parallel impedance formula has the resistance and reactance in the denominator, for the test values considered, the impedance response is dominated by the resistance. However, this is a good approximation since samples that have exceed percolation concentration of CNT networks are best at sensing, and these samples also have an impedance that is resistance dominated. In Figure D.3 it can be seen that during the strain sensing region, the impedance value decreases as no damage is taking place and the piezo-evolution decreases the resistance. However, as soon as damage is turned on, it dominates the response leading to an increase in the impedance values, reaching very high values towards the end where the sample undergoes full damage. These expected electrical responses are meant to help understand the experimental behavior observed during the electro-mechanical sensing tests presented in this document.

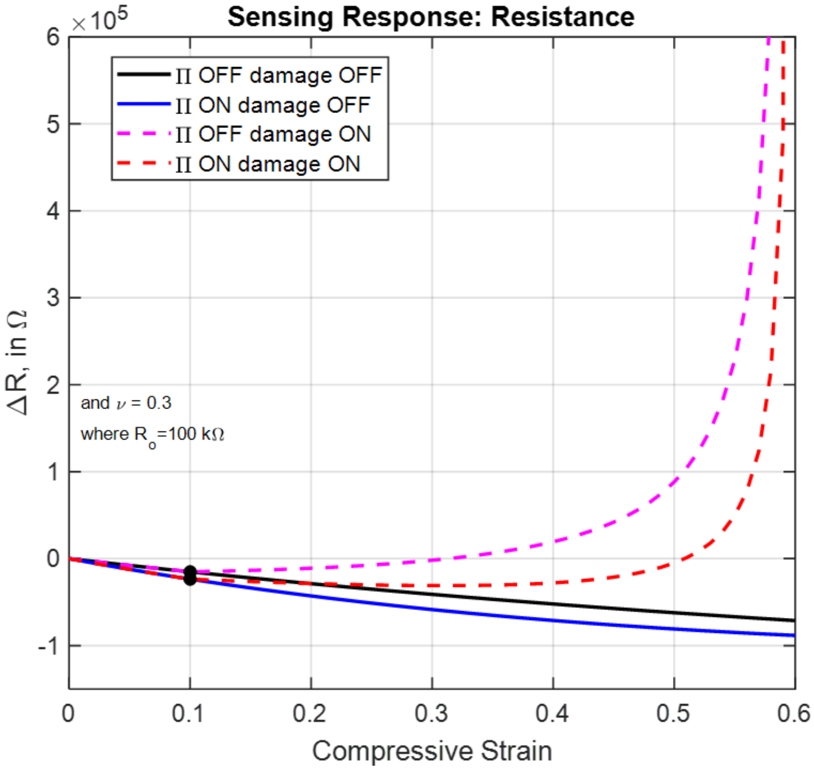

Figure D.1: Theoretical model showing the variation in Resistance as a function of strain. Damage is artificially turned on at 0.1 strain (marked by the black dot). The symbol Π indicates piezoresistive evolution of resistivity is turned on.

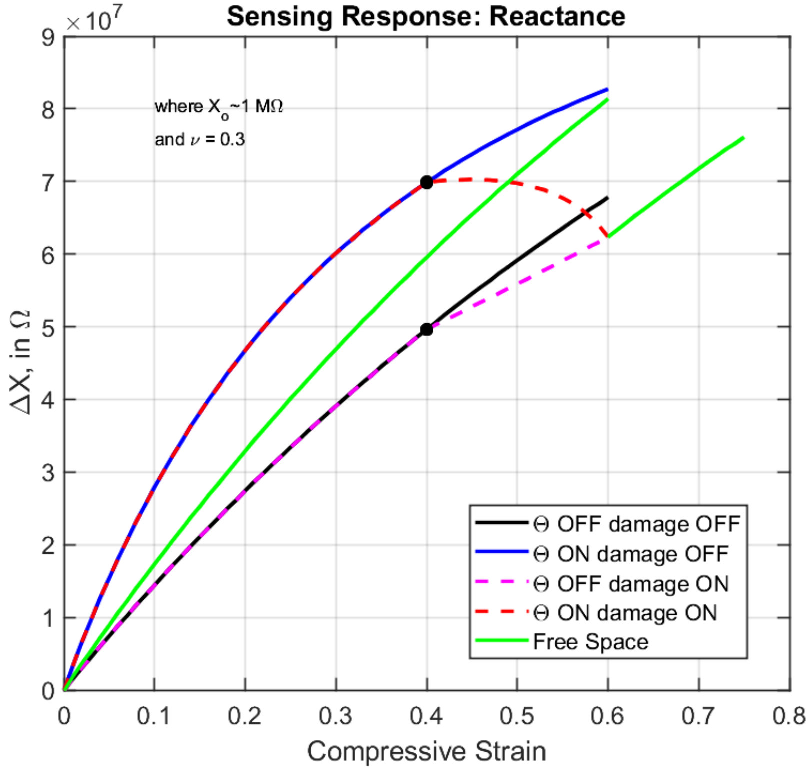

Figure D.2: Theoretical model showing the variation in Reactance as a function of strain. Damage is artificially turned on at 0.1 strain (marked by the black dot). The symbol Θ indicates piezocapacitance evolution of resistivity is turned on.

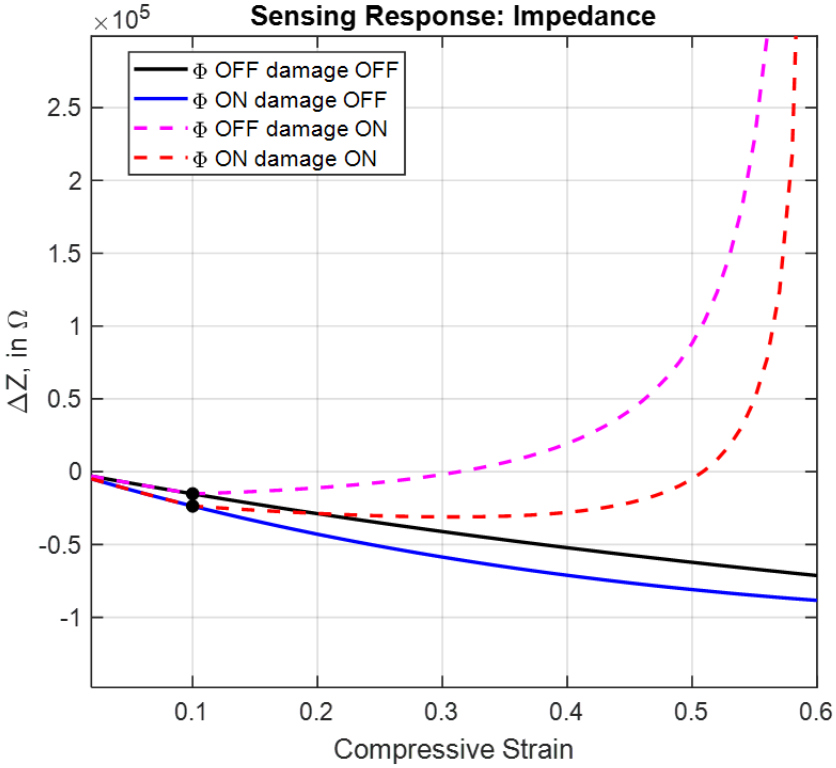

Figure D.3: Theoretical model showing the variation in parallel Impedance as a function of strain. Damage is artificially turned on at 0.1 strain (marked by the black dot). The symbol Φ indicates piezoresistive and piezocapacitance evolution of resistivity is turned on.

Appendix E

Nanocomposite Epoxy Fabrication: Additional Details

The following appendix section describes some fabrication tips and techniques that have been very useful for consistent, high quality sample production with epoxy (EPON 682 and W curing agent).

E.1 Nanoparticle Dispersion

The first step involved in achieving good nanoparticle dispersion is dispersing the nanoparticles in a low viscosity solvent such as acetone, ethanol, toluene, water, or chloroform. Depending on the type of polymer, the choice of the solvent must change. Solvents are sometimes incompatible with the polymer, eg. PDMS+acetone, causing swelling in the polymer and some level of permeation. This severely promotes the aggregation behavior in MWCNTs and GNPs which is contradictory to the goal of dispersion. Furthermore, it also decreases the extraction efficiency when the solvent and polymer are separated in the rotary evaporator. There is no commonly agreed ratio between the amount of solvent to use for every unit weight of MWCNT or GNP. Based on trial and error, the work presented in this document employed a ratio of 10 ml acetone for every 0.1 grams of carbon based nanoparticles. For a typical batch size (depending on the nanoparticle weight concentration), about 100 ml acetone was used, which occupied roughly 2/5th the volume of the beaker during sonication. Larger volumes typically require longer sonication times and large amplitudes. These parameters may cause breakage of nanoparticles and hence must be critically analyzed and then employed.

E.2 Degassing Process

It is highly desirable to obtain samples without any bubbles of voids present in the material. Practically speaking, the formation of voids is a complex process and complete elimination of voids is not an assured process. However, several fabrication steps can ensure macroscopic voids are not formed within the sample during fabrication. The first step after obtaining a mixture of the epoxy involves using elevated temperatures to reduce the viscosity. The reduced viscosity aids the quick escape of entrapped air during vacuum degassing, thus saving critical pot life time. This can be achieved by placing the glass beaker containing the epoxy on a hot plate and maintaining the temperature at 60^o. For most epoxies, there will be a temperature vs viscosity vs time chart available, either on the manufacturer's website or in other research works. This chart should provide information on determining the right temperature and time for which degassing can be performed. For the epoxy used in this work, elevated temperature of 60^o provides a significant drop in viscosity, while still allowing 35-45 minutes before significant crosslinking developments between the polymer chains.

After the first stage of degassing, the mixture should be poured in the molds. A very thin coat of mold release agent should always be used. This prevents easy release during extraction. However, from the perspective of degassing, the thin coat of mold release also smooths out microscopic surface roughness which can be nucleating points for void formations. The mold, which now contains the epoxy in it, must be degassed for a second time. This was found to significantly cut down the formation of macroscopic voids in the final product. During this second degassing stage, which shorter than the first, the rapid swelling of air bubble may lead to spillage and hence, it must be cautiously watched throughout. Finally, after the second degassing, the molds must be removed and kept on a flat, cool surface. Then a hot air gun should be hovered over the samples. Upon careful observation, one may see the popping of several bubbles entrapped on the surface layer of the epoxy. This final step ensures that the samples have minimal void formation after curing. As an additional note, silicone molds tend to have a reusable life of 2-3 fabrication cycles. After exceeding this limit, warping of the molds, increased surface roughness and excessive voids were observed. All these may affect the final sample quality.

Appendix F

Traced Pre-crack Fronts for All Samples: Influence of Pre-crack Characteristics

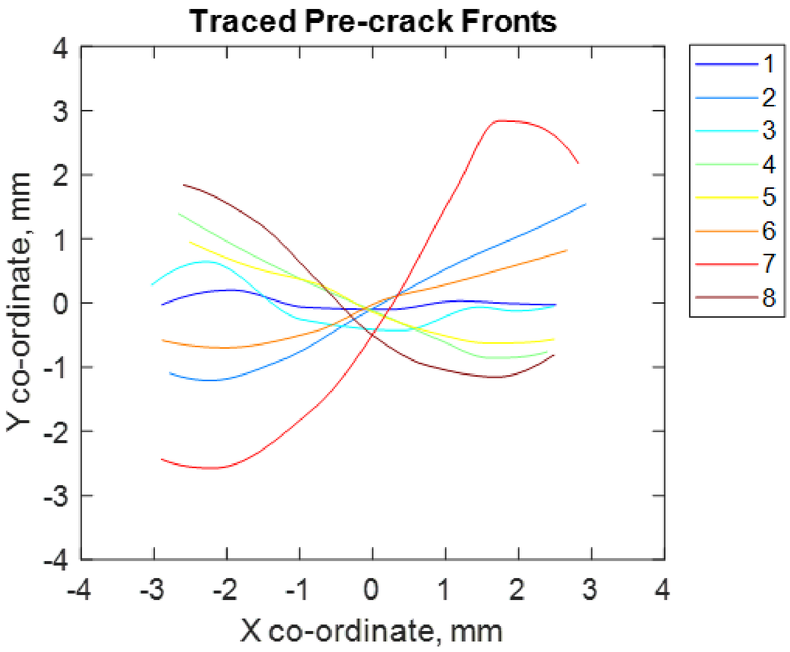

(a) Batch 1

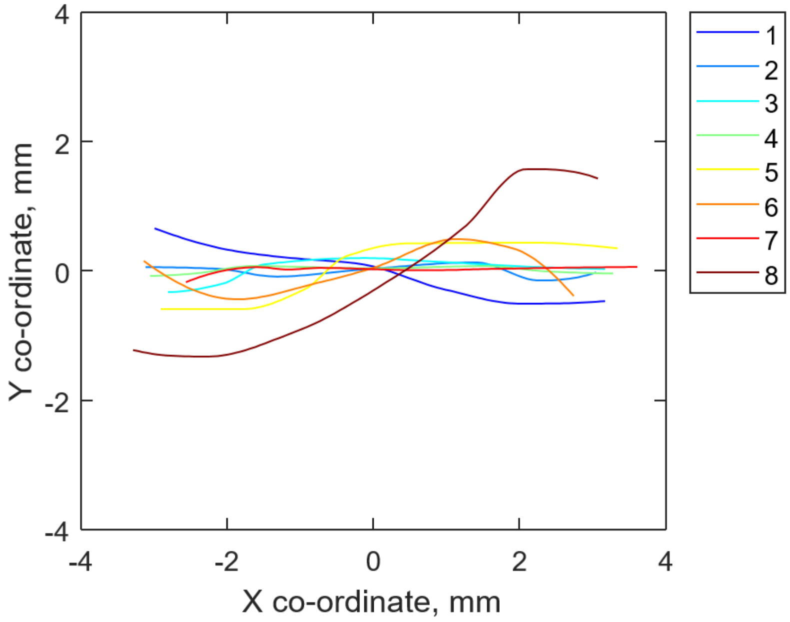

(b) Batch 2

Figure F.1: Traced pre-crack fronts for all the tested samples plotted on an X-Y co-ordinate system. The curves have been shifted such that they are roughly centered around the origin, in order to allow visual comparison. The legend on the right indicates the sample number from that respecctive batch.

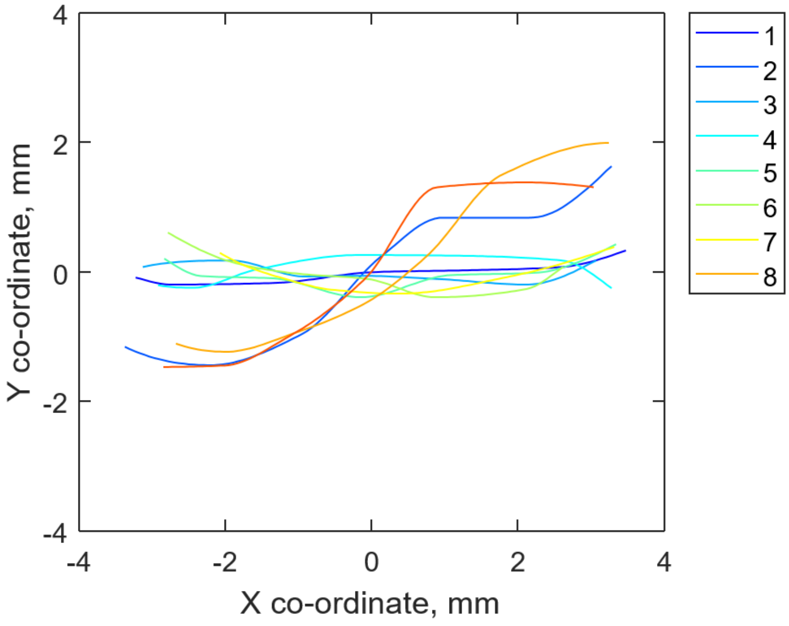

(c) Batch 3

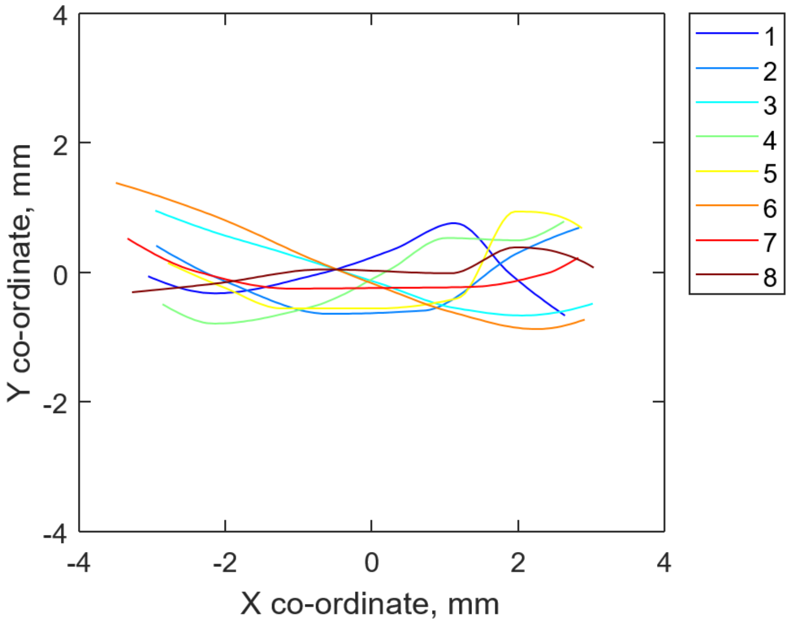

(d) Batch 4

Figure F.1: Traced pre-crack fronts for all the tested samples plotted on an X-Y co-ordinate system. The curves have been shifted such that they are roughly centered around the origin, in order to allow visual comparison. The legend on the right indicates the sample number from that respecctive batch.

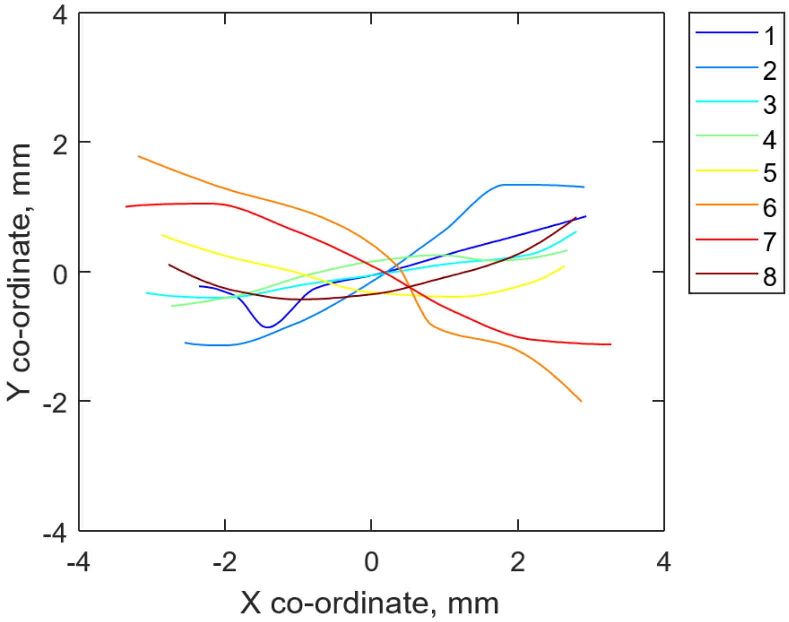

(e) Batch 5

Figure F.1: Traced pre-crack fronts for all the tested samples plotted on an X-Y co-ordinate system. The curves have been shifted such that they are roughly centered around the origin, in order to allow visual comparison. The legend on the right indicates the sample number from that respecctive batch.